Universita' degli studi di Milano-Bicocca
Istituto Nazionale di Alta Matematica
Universita' degli studi di Pavia

Joint Ph.D. Program in Mathematics
XXXIII Cycle

Virtual elements for Hellinger-Reissner elasticity problems

Supervisor:
Prof. Carlo Lovadina
Tutor:
Prof. Lourenço Beirão da Veiga

Ph.D. thesis of:
Michele Visinoni

Dedicated to my family

Contents

Introduction

Recently, the interest of numerical methods for the approximation of Partial Differential Equations (PDEs in short) based on polygonal and polyhedral meshes has grown considerably. The reason for this success is due to the flexibility that these grids offer. Indeed, employing polytopal meshes, we can handle, for instance, hanging nodes, non-convex elements, mesh refinement, an easier construction of adaptive meshes and a more efficient approximation of geometric data features.
Here we provide a short and non exhaustive list of polytopal methods: mimetic finite differences (MFD) [29, 33, 44], hybrid discontinuous Galerkin method and discontinuous Galerkin method (HDG-FEM and DG-FEM) [5, 51], polygonal finite element method (PFEM) [49, 63], hybrid high-order methods (HHO) [58, 59], weak Galerkin finite element method (WG-FEM) [84], extended finite element method (XFEM) [62].
Among these technologies, there is also the Virtual Element Method (in short VEM). Its first appearance in the scientific community was in 2013, see [22], where the authors presented it either as a generalization of the Finite Element Method (FEM) and as an elegant evolution of Mimetic Finite Differences. The fundamental idea behind this technology consists of abandoning the concept of local polynomial approximation, typically FEM, and using approximating functions that are solution of suitable local PDE. In general, these discrete functions are not known pointwise, but a limited information of them (degrees of freedom) is at disposal. Hence, the key point is to use the available information to compute certain local projection operators onto polynomial spaces and stabilizing bilinear forms. These two ingredients allow obtaining a stable and accurate method.
Although the Virtual Element Method is a very recent technology, its associated literature is widespread. Here we mention some of the topics and the problems covered by this technique: problem with curved edges [11, 14, 34, 53], Stokes problem [3, 24, 25, 32, 48], Cahn-Hillard equation [4], bilaplacian problem [23], magnetostatic problem [26, 27], geomechanics problem [2], Helmholtz problem [67, 68, 75] eigenvalue problem [64, 69], application to discrete fracture network simulations [35, 36, 37], contact problem [38], structural mechanics problems [12, 13, 17, 30, 85, 86, 87].
In the present thesis, we propose some Virtual Element schemes for linear elasticity problems, focusing our attention on the stress-displacement formulation based on the Hellinger-Reissner functional. As it is well-known, see for instance [10, 39], imposing both the symmetry of the stress tensor and the continuity of the tractions at the inter-elements is typically a great source of troubles in the framework of classical Galerkin schemes. Indeed,

in the Finite Element practice, one is led either to consider quite cumbersome schemes [6] or to relax the symmetry [8, 81, 82] with also the possibility of abandoning this feature [9]. Another recent interesting approach is analyzed in [73, 74]. The fundamental reason behind this difficulty lies in the local polynomial approximation. This construction forces the introduction of nodal degrees of freedom for the stress unknown, which is an additional complication if one aims at using the hybridization procedure to solve the discrete linear system, see [7]. Therefore, we exploit the flexibility of the VE approach to avoid these drawbacks. We propose some Virtual Element schemes that are reasonably cheap concerning the delivered accuracy. Particular emphasis is given to low-order methods for 3D problems, although in some cases, for simplicity, we present the analysis for the bi-dimensional case. Finally, the whole numerical scheme is developed inside the `vem++` library, a `c++` code realized at the University Milano-Bicocca during the CAVE project (`https://sites.google.com/view/vembic/home`).

A brief outline of the thesis

We briefly describe the structure of the work as follows:

- In Chapter 1, we present the Virtual Element Method and the elasticity equations. Moreover, we introduce some basic notations and the main assumptions that we have used in the thesis.

- In Chapter 2, we present a Virtual Element Method for 3D Hellinger-Reissner elasticity problems. We propose a low-order scheme with a-priori symmetric stresses and continuous tractions across element interfaces.

- In Chapter 3, we present and apply the hybridization technique to low-order VEMs for elasticity problems. We show some computational aspects both for 2D and 3D problems, and we suggest a possible post-processing to obtain a better reconstruction of the continuous solution.

- In Chapter 4, we introduce a very preliminary investigation of a VEM for an augmented Lagrangian formulation. More precisely, we present a deep numerical campaign in order to show what we have already done for this kind of topic and suggest the feasible future directions that need to be undertaken.

Chapter 1

Virtual Element Method and elasticity problem

The aim of this chapter is to introduce the two topics of this thesis: the Virtual Element Method and the elasticity problem. More precisely, after having briefly remind some basic notations and useful results of the classic PDEs theory, we will give a (non-exhaustive) overview of the fundamental aspects of the VEM technology. Finally, we will present the elasticity problem and its mixed formulation that will guide us to the remaining part of this dissertation.

1.1 Preliminaries: notations and assumptions

We begin introducing some preliminary results regarding classic PDEs theory. First of all, we will present some useful notations and a simple model problem, then we will discuss admissible polytopal decompositions through their properties. Here, we do not claim to be complete so, in the sequel, when a well-known concept is not explicitly introduced, we refer for instance to [39, 41, 50, 65] for its definition.

1.1.1 Space notation

Let $\Omega \subset \mathbb{R}^d$ a bounded Lipschitz-continuous domain and we denote by $\partial\Omega$ the boundary of Ω. We firstly define the Lebesgue space of square integrable functions on Ω as:

$$L^2(\Omega) := \left\{ u : \Omega \to \mathbb{R} \quad : \quad u \text{ is Lebesgue measurable and } \int_\Omega |u|^2 \, \mathrm{d}\Omega < \infty \right\}. \tag{1.1}$$

We endow this space with the following inner product and norm:

$$(u, v)_{0,\Omega} = \int_\Omega u\, v \, \mathrm{d}\Omega, \qquad ||u||^2_{0,\Omega} := \int_\Omega |u|^2 \, \mathrm{d}\Omega, \qquad \forall\, u, v \in L^2(\Omega). \tag{1.2}$$

Then, we introduce the Sobolev spaces. For any integer $m \geq 0$, we define

$$H^m(\Omega) := \left\{ u \in L^2(\Omega), \quad D^{\boldsymbol{\alpha}} u \in L^2(\Omega), \quad |\boldsymbol{\alpha}| \leq m \right\} \tag{1.3}$$

where $\boldsymbol{\alpha} := (\alpha_1, \alpha_2, \ldots, \alpha_d) \in \mathbb{N}^d$ is a multi-index and

$$D^{\boldsymbol{\alpha}} u := \frac{\partial^{|\boldsymbol{\alpha}|} u}{\partial x_1^{\alpha_1} \partial x_2^{\alpha_2} \ldots \partial x_d^{\alpha_d}}, \qquad |\boldsymbol{\alpha}| = \alpha_1 + \alpha_2 + \cdots + \alpha_d. \tag{1.4}$$

These (weak) derivatives are taken in the sense of distributions. On this space, we introduce the following inner product and induced norm

$$(u, v)_{m,\Omega} = \sum_{|\boldsymbol{\alpha}| \leq m} \int_\Omega D^{\boldsymbol{\alpha}} u \, D^{\boldsymbol{\alpha}} v \, \mathrm{d}\Omega, \qquad ||u||^2_{m,\Omega} = (u, u)_{m,\Omega}. \tag{1.5}$$

In addition, we also define the classical Sobolev semi-norms as follows

$$|u|^2_{m,\Omega} := \sum_{|\boldsymbol{\alpha}| = m} \int_\Omega D^{\boldsymbol{\alpha}} u \, D^{\boldsymbol{\alpha}} u \, \mathrm{d}\Omega. \tag{1.6}$$

Clearly, for $m = 0$ we have that $H^0(\Omega) = L^2(\Omega)$, whereas for $m = 1$ we have one of the most common Sobolev space used in the PDEs theory

$$H^1(\Omega) := \left\{ v \in L^2(\Omega) \ : \ \nabla v \in \left[L^2(\Omega) \right]^d \right\}, \tag{1.7}$$

with

$$(u, v)_{1,\Omega} = \int_\Omega (u\, v + \nabla u \cdot \nabla v) \, \mathrm{d}\Omega, \qquad ||u||_{1,\Omega} := \int_\Omega \left(|v|^2 + |\nabla v|^2 \right) \, \mathrm{d}\Omega. \tag{1.8}$$

Since the gradient ∇u of a scalar function is a vector-valued function, in (1.7) we ask that each component of the gradient is a square integrable function, in accordance with the notation used in (1.3). More in general, given a functional space X, we denote by

$$[X]^d, \quad [X]^{d\times d} \quad \text{and} \quad [X]^{d\times d}_s \tag{1.9}$$

the d vectors, the $d \times d$ tensors and the $d \times d$ symmetric tensors whose components belong to the space X, respectively.

Another important space, which is specially adapted to the study of mixed and hybrid methods for elasticity problems, is the following:

$$H(\mathbf{div}; \Omega) := \left\{ \boldsymbol{\sigma} \in \left[L^2(\Omega) \right]^{d\times d} \text{ s.t. } \mathbf{div}\, \boldsymbol{\sigma} \in \left[L^2(\Omega) \right]^d \right\} \tag{1.10}$$

endowing it with the graph norm

$$||\boldsymbol{\sigma}||^2_{H(\mathbf{div};\Omega)} := \int_\Omega |\boldsymbol{\sigma}|^2 \, \mathrm{d}\Omega + \int_\Omega |\, \mathbf{div}\, \boldsymbol{\sigma}|^2 \, \mathrm{d}\Omega = ||\boldsymbol{\sigma}||^2_{0,\Omega} + ||\, \mathbf{div}\, \boldsymbol{\sigma}||^2_{0,\Omega}. \tag{1.11}$$

As we can notice, $H(\mathbf{div}; \Omega)$ is the space of tensor in $[L^2(\Omega)]^{d\times d}$ whose divergence is the vector-valued operator in $[L^2(\Omega)]^d$. Henceforth, if the set Ω is clear from the contest we can erase it and we can write H^m, $H(\mathbf{div})$, $||\cdot||_m$ and $(\cdot,\cdot)_m$ instead of $H^m(\Omega)$, $H(\mathbf{div}; \Omega)$, $||\cdot||_{m,\Omega}$ and $(\cdot,\cdot)_{m,\Omega}$.

Finally we introduce the space of polynomials up to degree k. Given a subset $A \subset \mathbb{R}^d$ and integer $k \geq 0$, we denote by $\mathcal{P}_k(A)$ the space of polynomials up to degree k, defined on A. Conventionally, if $k = -1$, we set $\mathcal{P}_{-1}(A) = \{0\}$. Moreover, for each $k \geq 0$, we fix:

$$\nu_k = \dim(\mathcal{P}_k(A)). \tag{1.12}$$

We now assume that, for $k \in \mathbb{N}$, we are given $\{m_\alpha\}_{\alpha=1}^{\nu_k}$ a basis of $\mathcal{P}_k(A)$, then we obviously have that

$$span\left(\{m_\alpha\}_{\alpha=1}^{\nu_k}\right) = \mathcal{P}_k(A). \tag{1.13}$$

In this work, we select the set of scaled monomials $\mathcal{M}_k(A)$ as a basis of the polynomial spaces. The advantage of our choice is that this set of functions is invariant with respect to homothetic transformation [28]. This property will be useful from a computational point of view. Now, we briefly show an example of the set of scaled monomials for $d = 2$, taking into account that the three-dimensional case is only a simple extension.

Given $A \subset \mathbb{R}^2$ we denote by $\mathbf{x}_A = (x_{1,A}, x_{2,A})$ and h_A the barycenter and the diameter of A, respectively. Let $\mathbf{x} = (x_1, x_2)$ and given a multi-index $\boldsymbol{\alpha} = (\alpha_1, \alpha_2) \in \mathbb{N}^2$, we have that

$$\mathbf{x}^{\boldsymbol{\alpha}} = x_1^{\alpha_1} x_2^{\alpha_2}.$$

Then, we define the set of scaled monomials of degree less than equal to k as follows:

$$\mathcal{M}_k(A) := \{m_{\boldsymbol{\alpha}} \ : \ 0 \leq |\boldsymbol{\alpha}| \leq k\} \tag{1.14}$$

where

$$m_{\boldsymbol{\alpha}} := \left(\frac{\mathbf{x} - \mathbf{x}_A}{h_A}\right)^{\boldsymbol{\alpha}}. \tag{1.15}$$

We observe that there is a natural correspondence between the one-dimension index α (cf. (1.13)) and the multi-index $\boldsymbol{\alpha}$ (cf. (1.15)). We show this relation through the following basic example.

Example. Fixed $k = 2$, we have that the dimension of the space $\mathcal{P}_2(A)$, when $A \subset \mathbb{R}^2$ is equal to 6. A possible correspondence is given by the following basis relations:

$$\begin{aligned} &m_1 \leftrightarrow m_{(0,0)}, \qquad m_2 \leftrightarrow m_{(1,0)}, \quad m_3 \leftrightarrow m_{(0,1)} \\ &m_4 \leftrightarrow m_{(2,0)} \qquad m_5 \leftrightarrow m_{(1,1)} \quad m_6 \leftrightarrow m_{(0,2)}. \end{aligned} \tag{1.16}$$

From now on, for convenience, we will use the notation m_α instead of $m_{\boldsymbol{\alpha}}$ to denote the scaled monomials.

1.1.2 Model problem

Given $\Omega \subset \mathbb{R}^2$ polygonal domain, and let $f : \Omega \to \mathbb{R}$ and $g : \partial\Omega \to \mathbb{R}$ two regular functions. The aim is to find a function $u : \Omega \to \mathbb{R}$ such that the following equations are verified

$$\begin{cases} -\Delta u = f & \text{in } \Omega \\ \quad u = g & \text{on } \partial\Omega. \end{cases} \tag{1.17}$$

For simplicity, from now on, we will consider the Poisson problem (1.17) with homogeneous boundary conditions, e.g., by considering $g = 0$ on the boundary. Then, the associated variational formulation reads as

$$\begin{cases} \text{find } u \in V \text{ such that} \\ a(u, v) = \langle f, v \rangle \quad \forall v \in V. \end{cases} \tag{1.18}$$

where

$$V = H_0^1(\Omega) := \left\{ v \in H^1(\Omega) \ : \ v = 0 \text{ on } \partial\Omega \right\} \tag{1.19}$$

and

$$a(w, v) = \int_\Omega \nabla w \cdot \nabla v \ \mathrm{d}\Omega, \quad \forall w, v \in V,$$
$$\langle f, v \rangle = \int_\Omega f \ v \ \mathrm{d}\Omega \quad \forall v \in V.$$

As it is well known, thanks to the Lax-Milgram theorem, this problem is well-posed [42], indeed we have that

- $a(\cdot, \cdot) : V \times V \to \mathbb{R}$ is a continuous bilinear form, i.e., there exists a constant $\alpha^* > 0$ such that
$$|a(w, v)| \leq \alpha^* ||w||_V ||v||_V \quad \forall w, v \in V. \tag{1.20}$$
- $a(\cdot, \cdot) : V \times V \to \mathbb{R}$ is a coercive form, i.e., there exists a constant $\alpha_* > 0$ such that
$$|a(v, v)| \geq \alpha_* ||v||_V^2 \quad \forall v \in V. \tag{1.21}$$
The constant derives from the Poincaré inequality.
- $\langle f, \cdot \rangle : V \to \mathbb{R}$ is a linear continuous operator, i.e., there exists a constant $C > 0$
$$|\langle f, v \rangle| \leq C ||v||_V. \tag{1.22}$$

Hence, the problem (1.18) has a unique solution $u \in V$, which continuously depends on data

$$||u||_V \leq \frac{||f||_{V'}}{\alpha_*} \tag{1.23}$$

where V' is the dual space of V.

1.1.3 Polytopal decomposition

The Virtual Element technique, as we have already emphasized in the introduction, can be considered as a generalization of the Finite Element Method to polytopal meshes. Here, we introduce the basic notation and the reasonable assumptions on the mesh's elements in order to develop the theoretical analysis of the VEM.
Firstly, we take $\Omega \subset \mathbb{R}^d$ $(d = 2, 3)$ a bounded polygonal (polyhedral) domain, with a

Lipschitz continuous boundary. Let $\{\mathcal{T}_h\}_h$ be a sequence of decompositions of Ω into general nonoverlapping polygonal (polyhedral) elements E with

$$h_E := \text{diameter}(E), \quad h := \sup_{E \in \mathcal{T}_h} h_E$$

and let $\mathcal{V}_h$, $\mathcal{E}_h$ and $\mathcal{F}_h$ denote the set of vertices, edges and faces of $\mathcal{T}_h$, respectively. Moreover, the previous three sets can be split into two simple disjoint subsets. For instance, if we consider $\mathcal{V}_h$, we denote by $\mathcal{V}_h^I$ and $\mathcal{V}_h^B$ the subset of the internal and boundary vertices of the mesh $\mathcal{T}_h$. Similarly we can use the same notation for the edges $\mathcal{E}_h := \mathcal{E}_h^I \cup \mathcal{E}_h^B$ and for the faces $\mathcal{F}_h := \mathcal{F}_h^I \cup \mathcal{F}_h^B$.

Let's start to introduce the assumptions for both cases $d = 2, 3$.

Polygonal domain. We firstly fix some useful notations. Given a polygon $E \in \mathcal{T}_h$ with n_e^E edges, we denote its area, diameter and barycenter by $|E|$, h_E and $\mathbf{x}_E$, respectively. Moreover, given e an edge of the polygon E, we denote by $|e|$ (or h_e) the length of this edge. Afterwards, the basic assumptions that can be formulated on each element of the mesh $\mathcal{T}_h$ are the following (cf. [22]):

- (**A1**) : E is star-shaped with respect to a ball with radius greater or equal than $\gamma\, h_E$,
- (**A2**) : the distance between any two vertexes of E is greater or equal than $C\, h_E$,

where γ and C are positive constants independent from h and E.

Polyhedral domain. Given a polyhedron E with n_f^E faces, we denote its volume, diameter and barycenter by $|E|$, h_E and $\mathbf{x}_E$, respectively. In a similar way we refer to the area, diameter and barycenter of a face f. So, for each h, $\{T_h\}_h$ is a regular polyhedral decomposition if the following assumptions are satisfied (cf. [1]):

- (**B1**) : every element E is star-shaped with respect to all the points of a sphere of radius greater or equal to $\gamma\, h_E$,
- (**B2**) : every face $f \in \partial E$ is star-shaped with respect to all the points of a disk having radius greater or equal to $\gamma\, h_f$,
- (**B3**) : for every element E, for every face $f \in \partial E$, and for every edge $e \in \partial f$, we have

$$h_e \geq \gamma\, h_f \geq \gamma^2\, h_E,$$

where γ is a suitable positive constant.

Remark 1. *We remark that these assumptions are fundamental in the theoretical analysis of the method, but not for a practical construction. Actually, in the numerical tests, we will consider some meshes that do not satisfy the above conditions, but nevertheless, our method will not lose accuracy.*

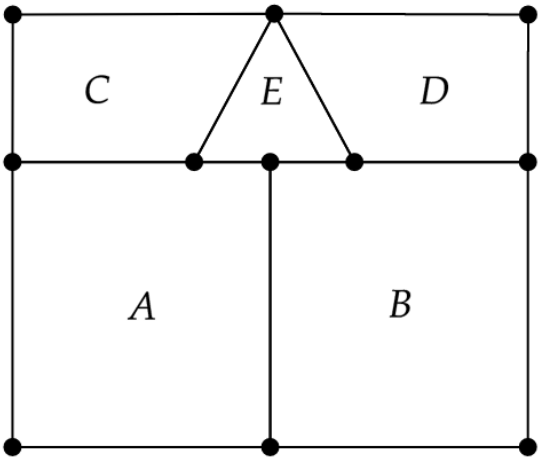

Figure 1.1: Elements A and B have 5 edges, C, D and E have 4 edges.

We point out some important advantages from the above mesh assumptions. First of all, it is possible to observe that the meshes, considered forbidden in the standard finite element theory, are now admissible, in particular, our assumptions cover the thorny issues of the *hanging nodes*. Indeed, since we deal with general polygons (polyhedrons), the hanging nodes can be seen as natural (extra) vertices of the element as it is showed in Figure 1.1. In other words, a polytopal element can not be determined by its geometric shape, but only for the number of its vertices, edges or faces. This means that, basically, they are not really hanging.

Additional advantage of working under these mesh hypothesis is that we can easier treat, for instance, the following problems: crack propagation, fractured materials, contact problems, fluid-structure interaction, adaptive mesh refinement and mesh gluing.

Remark 2. *Our mesh assumptions, although they are not too restrictive, could be further relaxed. In [31, 43], for instance, the authors provide a stability and an error analysis for the Poisson problem, by considering the presence of small edges. The main difference, in considering these weaker hypothesis, is that the proofs become more technical. Nevertheless, the assumptions stated above cover the use of very general decompositions and they turn out to be reasonable for our analysis.*

1.2 Virtual Element Method

Now we briefly present the Virtual Element Method and its main features through the use of the Poisson problem, see (1.17). For this presentation we refer to [22, 28], which represent two milestones in term of VE technology, from either a theoretical and computational point of view.

1.2.1 The discrete problem

We begin recalling the Poisson problem's variational formulation with homogeneous boundary conditions (1.18):

$$\begin{cases} \text{find } u_h \in V_h^k \text{ such that} \\ a_h(u_h, v_h) = \langle f_h, v_h \rangle \quad \forall v_h \in V_h^k \end{cases} \tag{1.24}$$

where

- $V_h^k \subset V := H_0^1(\Omega)$ is a finite dimensional space, k is the degree of accuracy;
- $a_h(\cdot,\cdot) : V_h^k \times V_h^k \to \mathbb{R}$ is the discrete bilinear form which approximates the continuous bilinear form $a(\cdot,\cdot)$;
- f_h is the discrete (loading) term.

Let $\{\mathcal{T}_h\}_h$ be a sequence of decompositions of Ω into general polygonal elements E such that, for each h, every element E fulfills the assumptions (**A1**) and (**A2**), defined in the Section 1.1.3.

1.2.2 The virtual spaces

Given a polygon E with n_e^E edges we define, for $k \geq 1$, the following finite dimensional local space:

$$\mathbb{B}_h^k(\partial E) := \left\{ v_h \in C^0(\partial E) \ : \ v_{h_{|e}} \in \mathcal{P}_k(e) \quad \forall e \in \partial E \right\}, \tag{1.25}$$

which is the space of continuous functions defined on the boundary ∂E and they are, restricted to each edge $e \in \partial E$, polynomials of degree less equal to k. Therefore, a function in this space is uniquely determined by its values at the n_e^E vertices of the polygon and, if $k > 1$, by its values at $k-1$ additional internal point on each edge. So the dimension of this space is

$$\dim(\mathbb{B}_h^k(\partial E)) := n_e^E + n_e^E(k-1) = n_e^E k. \tag{1.26}$$

Once we have defined this space, we are ready to define the following local virtual space:

$$V_h^k(E) := \left\{ v_h \in H^1(E) \ : \ v_{h_{|\partial E}} \in \mathbb{B}_h^k(\partial E) \quad \text{and} \quad \Delta v_h \in \mathcal{P}_{k-2}(E) \right\}. \tag{1.27}$$

A first remark is that $\mathcal{P}_k(E) \subset V_h^k(E)$. Indeed, a polynomial function $p \in \mathcal{P}_k(E)$ on the boundary belongs to the space $\mathbb{B}_h^k(\partial E)$, because it is a continuous function and restricted to each edge is also a polynomial of degree up to k, while inside the element its laplacian is a polynomial of degree less equal to $k-2$. This is a crucial condition for the approximation properties of the method. Moreover, it is not hard to see that a general function of $V_h^k(E)$ is virtual inside the element. Therefore, to describe a function in this space, we use the following degrees of freedom, see Figure 1.2:

- $\mathrm{D}_{\mathcal{V}_E}$: the values of v_h at the vertices of the element E;

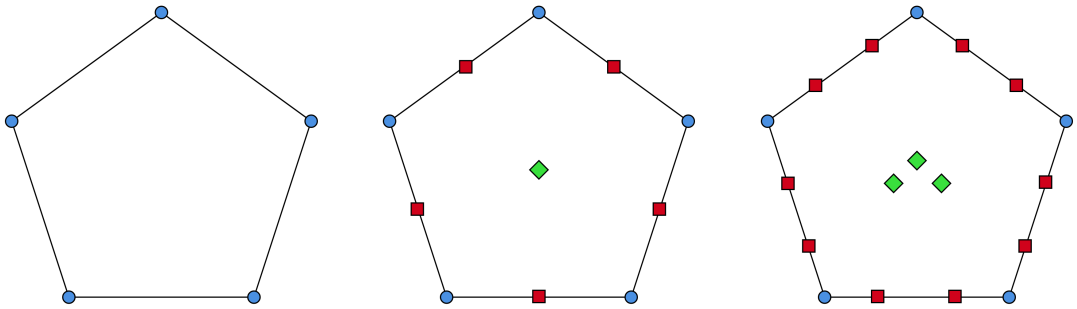

Figure 1.2: **Degrees of freedom for k=1,2,3.** We denote $\mathrm{D}_{\mathcal{V}_E}$ by blue dots, $\mathrm{D}_{\mathcal{E}_E}$ by red squares, $\mathrm{D}_{\mathcal{M}_E}$ by green squares.

- $\mathrm{D}_{\mathcal{E}_E}$: the values of v_h at $k-1$ additional points for each edge $e \in \partial E$, i.e., we can take the $k-1$ internal points of the $(k+1)$-point Gauss-Lobatto quadrature rule on edge e, see [28];
- $\mathrm{D}_{\mathcal{M}_E}$: the moments up to the order $k-2$ of v_h in E

$$\frac{1}{|E|}\int_E m_\alpha v_h \,\mathrm{d}E \qquad \forall m_\alpha \in \mathcal{P}_{k-2}(E), \tag{1.28}$$

  where we recall that, for $\alpha = 1, \dots, \nu_{k-2}$, m_α is a scaled monomial already defined in the previous sections.

For sake of simplicity, we also refer to the first two sets of degrees of freedom, $\mathrm{D}_{\mathcal{V}_E}$ and $\mathrm{D}_{\mathcal{E}_E}$, as *boundary degrees of freedom*, while we use the term *internal degrees of freedom* for the third set $\mathrm{D}_{\mathcal{M}_E}$.

Remark 3. *For degree of accuracy $k = 1$, the only set of degrees of freedom that survives is $D_{\mathcal{V}_E}$. The functions in the space $V_h^k(E)$ are harmonic functions and linear on each edge.*

The dimension of the space $V_h^k(E)$ is:

$$\begin{aligned} \dim(V_h^k(E)) &= \#\mathrm{D}_{\mathcal{V}_E} + \#\mathrm{D}_{\mathcal{E}_E} + \#\mathrm{D}_{\mathcal{M}_E} \\ &= \dim(\mathbb{B}_h^k(\partial E)) + \nu_{k-2} \\ &= n_e^E k + \frac{(k-1)k}{2}. \end{aligned} \tag{1.29}$$

We have the following unisolvence results for the degrees of freedom of the space $V_h^k(E)$.

Proposition 1.2.1. *Let E a simple polygon in $\mathcal{T}_h$ and we fix $k \geq 1$, then $v_h \in V_h^k(E)$ is completely determined by the degrees of freedom $D_{\mathcal{V}_E}$, $D_{\mathcal{E}_E}$ and $D_{\mathcal{M}_E}$.*

Here we give an idea of the proof, see [22] for more details. We assume that the dimension of the space $V_h^k(E)$ is equal to $\#\mathrm{D}_{\mathcal{V}_E} + \#\mathrm{D}_{\mathcal{E}_E} + \#\mathrm{D}_{\mathcal{M}_E}$ to proof the Proposition 1.2.1 we only need to check that if v_h has vanishing degrees of freedom, then v_h is identically zero.

Now, we are ready to introduce the global approximation space V_h^k, by glueing the local approximation spaces, see (1.27):

$$V_h^k := \left\{ v_h \in V \ : \ v_{h|E} \in V_h^k(E) \quad \forall E \in \mathcal{T}_h \right\}. \tag{1.30}$$

Therefore it holds that:

$$\dim(V_h^k) := \mathcal{V}_h^I + \mathcal{E}_h^I + \frac{(k-1)k}{2} N_E, \tag{1.31}$$

where N_E is the number of the element in $\mathcal{T}_h$, whereas we recall that $\mathcal{V}_h^I$ and $\mathcal{E}_h^I$ are the sets of internal vertices and edges of $\mathcal{T}_h$, respectively. In agreement with the local sets of degrees of freedom, the global degrees of freedom are the following:

- $\mathrm{D}_{\mathcal{V}}$: the values of v_h at the internal vertices $\mathcal{V}_h^I$ of $\mathcal{T}_h$;
- $\mathrm{D}_{\mathcal{E}}$: the values of v_h at $k-1$ additional points on each internal edge $e \in \mathcal{E}_h^I$;
- $\mathrm{D}_{\mathcal{M}}$: the moments up to the order $k-2$ of v_h in each element $E \in \mathcal{T}_h$

$$\frac{1}{|E|} \int_E m_\alpha v_h \, \mathrm{d}E \qquad \forall m_\alpha \in \mathcal{P}_{k-2}(E). \tag{1.32}$$

We observe that $V_h^k \subset V := H_0^1(\Omega)$, then on the vertices and edges belonging to the boundary $\partial\Omega$ we have $v_h = 0$. This is why we consider only the internal vertices and edges in the definition of the global boundary degrees of freedom. Their unisolvence easily comes from Proposition 1.2.1.

1.2.3 The discrete form

We introduce the virtual discrete form and the construction of the right-hand side underling the main properties of this technology.

The local bilinear form $a_E(\cdot,\cdot)$. Usually the local bilinear form

$$a_E(u_h, v_h) := \int_E \nabla u_h \cdot \nabla v_h \, \mathrm{d}E \tag{1.33}$$

is not computable for an arbitrary pair $(u_h, v_h) \in V_h^k(E) \times V_h^k(E)$. The reason is that, inside the element E, we do not know (explicitly) the discrete functions u_h and v_h, and consequently the gradient of these functions. Thankfully, polynomials come to our aid to solve this trouble. We can observe that, when one of the two entries is a polynomial,

the bilinear form in (1.33) is computable. Actually, for every $v_h \in V_h^k(E)$ and for every $p \in \mathcal{P}_k(E)$, using the divergence theorem, we have that

$$\begin{aligned} a_E(p, v_h) &= \int_E \nabla p \cdot \nabla v_h \, \mathrm{d}E \\ &= -\int_E \Delta p \, v_h \, \mathrm{d}E + \int_{\partial E} \nabla p \cdot \mathbf{n} \, v \, \mathrm{d}s \end{aligned} \tag{1.34}$$

where $\mathbf{n}$ is the outward normal to the boundary ∂E.

The first term is computable from the local internal degrees of freedom since $\Delta p \in \mathcal{P}_{k-2}(E)$, while the second term is also computable using, this time, the local boundary degrees of freedom.

Therefore, the core of this technology is to introduce a suitable approximation of $a_E(\cdot, \cdot)$

$$a_E^h(\cdot, \cdot) : V_h^k(E) \times V_h^k(E) \to \mathbb{R} \tag{1.35}$$

such that the following two fundamental properties are verified:

- **k-consistency**: for all $p \in \mathcal{P}_k(E)$ and for all $v_h \in V_h^k(E)$

$$a_E^h(p, v_h) = a_E(p, v_h); \tag{1.36}$$

- **stability**: there exist two positive constants α_* and α^*, independent of h and E such that

$$c_* a_E(v_h, v_h) \leq a_E^h(v_h, v_h) \leq c^* a_E(v_h, v_h) \quad \forall v_h \in V_h^k(E). \tag{1.37}$$

Let's start with the **k-consistency** and we introduce a suitable projection operator

$$\Pi_E^k : V_h^k(E) \to \mathcal{P}_k(E) \tag{1.38}$$

defined as follows

$$\begin{cases} a_E(\Pi_E^k v_h, q) = a_E(v_h, q) & \forall q \in \mathcal{P}_k(E) \\ P_E^0(\Pi_E^k v_h - v_h) = 0 \end{cases} \tag{1.39}$$

where the second equation takes care of the constant part. Here below, we show two possible choice for $P_E^0 : V_h^k(E) \to \mathcal{P}_0(E)$:

$$P_E^0(v_h) := \begin{cases} \dfrac{1}{n_e^E} \displaystyle\sum_{i=1}^{n_e^E} v_h(V_i) & \text{for} \quad k = 1 \\ \dfrac{1}{|E|} \displaystyle\int_E v_h \, \mathrm{d}E & \text{for} \quad k \geq 2 \end{cases} \tag{1.40}$$

where $V_1, \ldots, V_{N_e^E}$ are the vertices of the polygon E. The projection operator Π_E^k is computable using integration by parts and the degrees of freedom, see [22]. Instead, to ensure the **stability**, the strategy of VEM is to introduce a suitable symmetric, positive definite bilinear form

$$S_E(\cdot, \cdot) : V_h^k(E) \times V_h^k(E) \to \mathbb{R} \tag{1.41}$$

such that, for every $v_h \in V_h^k(E)$ with $\Pi_E^k v_h = 0$, it holds

$$c_* a_E(v_h, v_h) \leq S_E(v_h, v_h) \leq c^* a_E(v_h, v_h) \tag{1.42}$$

where c_* and c^* are two positive constants, independent of E and h.

Then, for every $u_h, v_h \in V_h^k(E)$, the approximation of $a_E(\cdot, \cdot)$ is thus:

$$a_E^h(u_h, v_h) := a_E(\Pi_E^k u_h, \Pi_E^k v_h) + S_E(u_h - \Pi_E^k u_h, v_h - \Pi_E^k v_h). \tag{1.43}$$

From the above definition, it is not hard to see that the bilinear form $a_E^h(\cdot, \cdot)$ satisfies the **k-consistency** and the **stability** properties.

Remark 4. *The choice of the stabilization term depends on the problem and on the degrees of freedom [22, 31, 56].*

Finally, once we have defined the local approximation of $a_E(\cdot, \cdot)$, see (1.43), the global approximation form is achieved as follows

$$a_h(u_h, v_h) := \sum_{E \in \mathcal{T}_h} a_E^h(u_h, v_h), \tag{1.44}$$

for every $u_h, v_h \in V_h^k$

The discrete loading term. We first consider the case $k \geq 2$, and we define for each element E the L^2-projection onto the space $\mathcal{P}_{k-2}(E)$, that is,

$$f_h = P_E^{k-2}(f) \quad \text{on each } E \in \mathcal{T}_h. \tag{1.45}$$

Consequently, the associated right-hand side is

$$\begin{aligned} \langle f_h, v_h \rangle &= \sum_{E \in \mathcal{T}_h} \int_E f_h v_h \, \mathrm{d}E \\ &= \sum_{E \in \mathcal{T}_h} \int_E P_E^{k-2}(f) \, v_h \, \mathrm{d}E \\ &= \sum_{E \in \mathcal{T}_h} \int_E f \; P_E^{k-2}(v_h) \, \mathrm{d}E. \end{aligned} \tag{1.46}$$

and the fundamental observation is that $P_E^{k-2}(v_h)$ can be computed from the internal degrees of freedom for V_h^k. Rather, for $k = 1$ there is an "ad-hoc" precedure. We approximate f by a piecewise constant and using (1.40) we define

$$\langle f_h, v_h \rangle = \sum_{E \in \mathcal{T}_h} |E| P_E^0(f) \frac{1}{n_e^E} \sum_{i=1}^{n_e^E} v_h(V_i) \tag{1.47}$$

where we recall that $V_1, \ldots, V_{n_e^E}$ are the vertices of the element E.

1.2.4 Convergence analysis

In this section we briefly recall, without proving, the main important results for the convergence of the method. We assume that the mesh assumptions (**A1**) and (**A2**) are always fulfilled. In accordance with the classical Scott-Dupont theory [42] we have the following two fundamental approximation estimates. The first estimate, regards polynomial functions:

Proposition 1.2.2. *Given h, let $E \in \mathcal{T}_h$ and $k \geq 1$, then for every $w \in H^{s+1}(E)$, with $0 \leq s \leq k$ there exists a polynomial function $w_\pi \in \mathcal{P}_k(E)$ such that*

$$||w - w_\pi||_{0,E} + h_E|w - w_\pi|_{1,E} \leq Ch_E^{s+1}|w|_{s+1,K} \tag{1.48}$$

where C is a constant independent of h.

On the other hand, the second result regards the interpolation operator, see [22] for its definition.

Proposition 1.2.3. *Given h and let $E \in \mathcal{T}_h$, then for every $w \in H^{s+1}(E)$, with $1 \leq s \leq k$ there exists a unique interpolation $w_I \in V_h^k(E)$ such that*

$$||w - w_I||_{0,E} + h_E|w - w_I|_{1,E} \leq Ch_E^{s+1}|w|_{s+1,K} \tag{1.49}$$

where C is a constant independent of h.

Employing now the previous estimates, we present the following main convergence result [22]:

Theorem 1.2.4. *Let u be the solution of the Problem (1.18) and let u_h be the solution of the discrete Problem (1.24). Assuming that the solution $u \in H^{k+1}(\Omega)$ and the data $f \in H^{k-1}(\Omega)$, then we have that*

$$|u - u_h|_{1,\Omega} \leq Ch^k|u|_{k+1,\Omega} \tag{1.50}$$

where C is a constant independent of h.

1.2.5 Implementation details

In this section, we briefly show some details about the implementation of the method, see [28] for a deeper study for a bi-dimensional Poisson problem. As in the standard finite element methods, the global stiffness matrix is obtained by assembling the local ones. Therefore, we show the computation of the local stiffness matrix (cf. (1.43)).

First of all, we need to fix some notations. Fixed a mesh $\mathcal{T}_h$, we consider a polygonal element E. Once numbered the local degrees of freedom from 1 to $\eta_E^k = \dim(V_h^k(E))$ we define the operator

$$\text{dof}_i : V_h^k(E) \to \mathbb{R} \tag{1.51}$$

such that for every $v_h \in V_h^k(E)$ we have

$$\text{dof}_i(v_h) := i\text{-th degree of freedom of } v_h \qquad \text{for } i = 1, \dots, \eta_E^k. \tag{1.52}$$

The basis functions $\varphi_i \in V_h^k(E)$ are defined as usual as the canonical basis functions:

$$\text{dof}_i(\varphi_j) = \delta_{ij} \qquad i, j = 1, \dots, \eta_E^k. \tag{1.53}$$

Moreover, the following identity holds:

$$v_h = \sum_{i=1}^{\eta_E^k} \text{dof}_i(v_h)\varphi_i \qquad \forall v_h \in V_h^k(E). \tag{1.54}$$

After we have introduced the previous useful notation, the local stiffness matrix is given by

$$\mathbf{A}_h^E := (\mathbf{\Pi}_*^\nabla)^T \tilde{\mathbf{G}} (\mathbf{\Pi}_*^\nabla) + (\mathbf{I} - \mathbf{\Pi}^\nabla)^T \mathbf{S} (\mathbf{I} - \mathbf{\Pi}^\nabla), \tag{1.55}$$

where all the quantities are defined here below.

Matrix $\mathbf{\Pi}_*^\nabla$. This matrix is the representation of the projection operator $\Pi_E^k : V_h^k(E) \to \mathcal{P}_k(E)$ defined in (1.38):

$$\mathbf{\Pi}_*^\nabla := \mathbf{G}^{-1}\mathbf{B}. \tag{1.56}$$

We begin with the definition of $\nu_k \times \nu_k$ matrix $\mathbf{G}$:

$$\mathbf{G}_{\alpha,\beta} := \begin{cases} P_E^0(m_\beta) & \alpha = 1, \text{ and } \forall \beta = 1, \dots, \nu_k; \\ (\nabla m_\beta, \nabla m_\alpha)_{0,E} & \forall \alpha, \beta = 2, \dots, \nu_k; \\ 0 & \text{otherwise.} \end{cases} \tag{1.57}$$

Using (1.40) applied to the scaled monomials and a suitable quadrature rule, which depends on the degree k, it is straightforward to implement the above matrix. Instead, the $\nu_k \times \eta_E^k$ matrix $\mathbf{B}$ is defined as follows

$$\mathbf{B}_{\alpha,i} := \begin{cases} (\nabla \varphi_i, \nabla m_\alpha)_{0,E} & \forall \alpha = 2, \dots, \nu_k, \forall i = 1, \dots, \eta_E^k; \\ P_E^0(\varphi_i) & \text{otherwise.} \end{cases} \tag{1.58}$$

We recall that the functions φ_i are unknown inside the element E. Then, to compute the matrix $\mathbf{B}$, we absolutely need to use the divergence theorem

$$(\nabla \varphi_i, \nabla m_\alpha)_{0,E} := -\int_E \Delta m_\alpha \varphi_i \, \mathrm{d}E + \int_{\partial E} \nabla m_\alpha \cdot \mathbf{n} \, \varphi_i \, \mathrm{d}s. \tag{1.59}$$

On the one hand, for the first term, we have that $\Delta m_\alpha \in \mathcal{P}_{k-2}(E)$ so we use the internal degrees of freedom $\mathrm{D}_\mathcal{M}$ to compute it. While, on the other we observe that the integrand function of the second term is a polynomial up to degree $2k-1$, then we use the boundary degrees of freedom $(\mathrm{D}_\mathcal{V} + \mathrm{D}_\mathcal{E})$ to exactly compute the integral.

Remark 5. *The term "exactly", referred to integrals' computation, means that we do not use any approximation for the integrand functions. Indeed, using the available information, as degrees of freedom or polynomial functions, we can compute the integrals only with a suitable quadrature rule.*

Matrix $\mathbf{\Pi}^{\nabla}$. This matrix represents the expansion of the projection operator Π_E^k in term of the basis functions of $V_h^k(E)$:

$$\mathbf{\Pi}^{\nabla} = \mathbf{D}\mathbf{\Pi}_*^{\nabla} \tag{1.60}$$

where $\mathbf{D}$ is a $\eta_E^k \times \nu_k$ matrix and it is defined as

$$\mathbf{D}_{i,\alpha} := \text{dof}_i(m_\alpha) \quad \forall i = 1, \dots, \eta_E^k, \forall \alpha = 1, \dots, \nu_k. \tag{1.61}$$

Remark 6. *Since $\mathcal{P}_k(E) \subset V_h^k(E)$, for every $\beta = 1, \dots, \nu_k$ we have the following relation:*

$$m_\beta := \sum_{i=1}^{\eta_E^k} dof_i(m_\beta)\varphi_i. \tag{1.62}$$

So the matrix $\mathbf{G}$ can be expressed in terms of $\mathbf{B}$ and $\mathbf{D}$ as follows:

$$\mathbf{G} = \mathbf{B}\mathbf{D}. \tag{1.63}$$

Although we do not use (1.63) in the explicit construction of the matrix $\mathbf{G}$, we can exploit this relation to check the correctness of the VEM code, as a sort of crucial test.

Finally the last two matrices are the following:

$$\tilde{\mathbf{G}}_{\alpha,\beta} := \begin{cases} \mathbf{G}_{\alpha,\beta} & \forall \alpha, \beta = 2, \dots, \nu_k; \\ 0 \quad \text{otherwise} \end{cases} \tag{1.64}$$

while the matrix $\mathbf{S}$, which represents the stabilization term is defined as follows

$$\mathbf{S}_{i,j} = S_E(\varphi_j, \varphi_i) \quad \forall i, j = 1, \dots, \eta_E^k. \tag{1.65}$$

Remark 4 states that there are different choices for the stabilization term. For instance, in [28] the stabilization introduced is the simplest one: the identity matrix. Instead in [56], the authors explore some high-order VEMs for 3D Poisson problem, with different stabilization terms and polynomial bases.

1.3 Elasticity problem

In this section, we present the problem and its variational formulation discussed in this work. When we deal with elasticity problems, we study both the deformations of elastic bodies under the influence of applied forces and the stresses and strains which result from deformations. Here, we focus our attention on the linear case considering a homogeneous and isotropic material. Therefore, we work in the framework of small displacement and small deformation.

In this setting, we have three different variational formulations for this problem, which depends on the number of the variables considered. So we have

- **the displacement formulation,** where the only variable is the displacement $\mathbf{u}$;
- **the mixed formulation based on Hellinger-Reissner principle,** where the stress $\boldsymbol{\sigma}$ and the displacement $\mathbf{u}$ are the variables of our problem;
- **the mixed formulation based on Hu-Washizu principle,** where we take into account all variables: the stress $\boldsymbol{\sigma}$, the strain $\boldsymbol{\varepsilon}$ and the displacement $\mathbf{u}$.

In this dissertation, we choose the second one.

1.3.1 The Hellinger-Reissner formulation

We present the elasticity problem based on the Hellinger-Reissner principle for the three-dimensional case [39, 41]. The bi-dimensional problem will be analogous.

Let $\Omega \subseteq \mathbb{R}^3$ be a Lipschitz polyhedral domain, which represents our elastic body and let $\partial\Omega$ its regular boundary. Moreover, we denote by $\mathbf{f} \in [L^2(\Omega)]^3$ the loading term and let $\mathbb{C}$ the Cauchy stress tensor, which depends on the material of the body. Then, the linear elasticity problem reads

$$\begin{cases} \text{find } (\boldsymbol{\sigma}, \mathbf{u}) \text{ such that} & & \\ \mathbf{div}\,\boldsymbol{\sigma} + \mathbf{f} = \mathbf{0} & \text{in } \Omega & \text{the equilibrium equation,} \\ \boldsymbol{\sigma} = \mathbb{C}\boldsymbol{\varepsilon}(\mathbf{u}) & \text{in } \Omega & \text{the costitutive law,} \end{cases} \tag{1.66}$$

where $\mathbf{u}$ and $\boldsymbol{\sigma}$ represent the displacement and the stress fields, respectively. Denoting by $\boldsymbol{\varepsilon}(\cdot)$ the symmetric gradient operator, we define the strain tensor by:

$$\boldsymbol{\varepsilon}(\mathbf{u}) := \frac{\nabla\mathbf{u} + \nabla\mathbf{u}^T}{2}. \tag{1.67}$$

We recall that the first equation of (1.66) represents the equilibrium of all internal and external forces of the system, while the second one is the Hook's equation, which depends on the material of the body. More precisely, since we are in the linear case, we observe that the relationship between stress and strain can be written in the following easier way:

$$\boldsymbol{\sigma} := \mathbb{C}\boldsymbol{\varepsilon}(\mathbf{u}) = 2\mu\boldsymbol{\varepsilon}(\mathbf{u}) + \lambda \mathrm{tr}(\boldsymbol{\varepsilon}(\mathbf{u}))I, \tag{1.68}$$

where $\lambda > 0, \mu > 0$ are the Lamè coefficients, $\mathrm{tr}(\cdot)$ is the trace operator and I is the identity tensor.

Remark 7. *Alternatively, the equation (1.68) can be define as follows*

$$\boldsymbol{\sigma} = \frac{E}{1+\nu}\left(\boldsymbol{\varepsilon}(\mathbf{u}) + \frac{\nu}{1-2\nu}\right) tr(\boldsymbol{\varepsilon}(\mathbf{u}))I, \tag{1.69}$$

where we use a different set of material constants, namely the Young's modulus of elasticity E and the Poisson ratio ν.

Remark 8. *The natural relationship between the two couples of material parameters* (λ, μ) *and* (E, ν) *is:*

$$\nu(\lambda, \mu) = \frac{\lambda}{2(\lambda + \mu)}, \qquad E(\lambda, \mu) = \frac{\mu(3\lambda + 2\mu)}{\lambda + \mu}, \tag{1.70}$$

and

$$\lambda(E, \nu) = \frac{E\nu}{(1 + \nu)(1 - 2\nu)}, \qquad \mu(E, \nu) = \frac{E}{2(1 + \nu)}. \tag{1.71}$$

From physical considerations, we have that $\lambda > 0, \mu > 0$, *and* $E > 0, 0 < \nu < 1/2$. *Moreover, for compressible materials we have* $\lambda \sim \mu$, *whereas, for nearly incompressible materials,* $\lambda >> \mu$, *i.e.,* ν *is very close to* $1/2$.

For the treatment of the boundary conditions we consider the general case. Therefore, we split $\partial\Omega$ into two regular disjoint parts $\partial\Omega_D$ and $\partial\Omega_N$ and we take the following conditions:

$$\begin{array}{lll} \mathcal{BC}_D(\mathbf{u}) : & \mathbf{u} = \mathbf{g} \quad \text{on } \partial\Omega_D & \text{Dirichlet boundary conditions,} \\ \mathcal{BC}_N(\boldsymbol{\sigma}) : & \boldsymbol{\sigma} \cdot \mathbf{n} = \boldsymbol{\psi} \quad \text{on } \partial\Omega_N & \text{Neumann boundary conditions,} \end{array} \tag{1.72}$$

with $\mathbf{n}$ is the unit outward normal vector to $\partial\Omega_N$ and the displacements $\mathbf{g} : \partial\Omega_D \to \mathbb{R}^3$ and the tractions $\boldsymbol{\psi} : \partial\Omega_N \to \mathbb{R}^3$ are two regular functions.

Defining $(\cdot, \cdot)$ as the scalar product in L^2, $\mathbb{D} := \mathbb{C}^{-1}$ and $a(\boldsymbol{\sigma}, \boldsymbol{\tau}) := (\mathbb{D}\boldsymbol{\sigma}, \boldsymbol{\tau})$, the Hellinger-Reissner mixed formulation of the Problem (1.66):

$$\begin{cases} \text{Find } (\boldsymbol{\sigma}, \mathbf{u}) \in \Sigma_{\boldsymbol{\psi}} \times U \text{ such that} \\ a(\boldsymbol{\sigma}, \boldsymbol{\tau}) + (\mathbf{div}\, \boldsymbol{\tau}, \mathbf{u}) = \displaystyle\int_{\partial\Omega_D} \mathbf{g} \cdot \boldsymbol{\tau}\, \mathbf{n}\, \mathrm{d}\Omega \quad \forall \boldsymbol{\tau} \in \Sigma_{\mathbf{0}} \\ (\mathbf{div}\, \boldsymbol{\sigma}, \mathbf{v}) = -(\mathbf{f}, \mathbf{v}) \qquad\qquad\qquad\qquad \forall \mathbf{v} \in U \end{cases} \tag{1.73}$$

where the displacement space U is

$$U = \left[L^2(\Omega)\right]^3$$

and, for a given function $\mathbf{h} : \partial\Omega_N \to \mathbb{R}^3$, the stress space $\Sigma_{\mathbf{h}}$ is

$$\Sigma_{\mathbf{h}} = \left\{ \boldsymbol{\tau} \in H(\mathbf{div}; \Omega) \ : \ \boldsymbol{\tau} \text{ is symmetric}; \quad \boldsymbol{\tau} \cdot \mathbf{n}_{|\partial\Omega_N} = \mathbf{h} \right\}.$$

The elasticity fourth-order symmetric tensor $\mathbb{D}$ is assumed to be uniformly bounded, positive-definite and sufficiently regular.

Remark 9. *We remark that in this Hellinger-Reissner mixed formulation, the tractions prescribed on* $\partial\Omega_N$ *are directly included in the functional space* $\Sigma_{\boldsymbol{\psi}}$ *(the so-called forced boundary conditions), while the displacements prescribed on* $\partial\Omega_D$ *are imposed in a weak sense through the introduction of the right-hand side in the first equation of* (1.73) *(the so-called natural boundary conditions).*

From now on, for sake of simplicity, we consider the case of homogeneous Dirichlet boundary conditions, hence we take $\partial\Omega_N = \emptyset$ and $\mathbf{g} = \mathbf{0}$. Thus, the problem (1.73) becomes

$$\begin{cases} \text{Find } (\boldsymbol{\sigma}, \mathbf{u}) \in \Sigma \times U \text{ such that} \\ a(\boldsymbol{\sigma}, \boldsymbol{\tau}) + (\mathbf{div}\, \boldsymbol{\tau}, \mathbf{u}) = 0 & \forall \boldsymbol{\tau} \in \Sigma \\ (\mathbf{div}\, \boldsymbol{\sigma}, \mathbf{v}) = -(\mathbf{f}, \mathbf{v}) & \forall \mathbf{v} \in U \end{cases} \tag{1.74}$$

where

$$\Sigma := \{\boldsymbol{\tau} \in H(\mathbf{div}, \Omega) \ : \ \boldsymbol{\tau} \text{ is symmetric}\}.$$

It is well known, see for instance [39, 41], that

- $a(\cdot, \cdot) : \Sigma \times \Sigma \to \mathbb{R}$ is a symmetric and continuous bilinear form, i.e., there exists a constant $\alpha^* > 0$ such that

$$|a(\boldsymbol{\sigma}, \boldsymbol{\tau})| := \left| \int_\Omega \mathbb{D}\boldsymbol{\tau} : \boldsymbol{\sigma} \, \mathrm{d}\Omega \right| \leq \alpha^* ||\boldsymbol{\sigma}||_\Sigma ||\boldsymbol{\tau}||_\Sigma \quad \forall \boldsymbol{\sigma}, \boldsymbol{\tau} \in \Sigma, \tag{1.75}$$

  where $\boldsymbol{\tau} : \boldsymbol{\sigma} = \sum_{ij} \boldsymbol{\tau}_{ij} \boldsymbol{\sigma}_{ij}$ is the Frobenius inner product, which is analogous to the vector inner product. Moreover we observe that the constant α^* depends on the elasticity tensor $\mathbb{D}$.

- The mixed term $(\mathbf{div}\, \cdot, \cdot) : \Sigma \times U \to \mathbb{R}$ is a continuous bilinear form, i.e., there exist a constant c such that

$$|(\mathbf{div}\, \boldsymbol{\sigma}, \mathbf{u})| := \left| \int_\Omega \mathbf{div}\, \boldsymbol{\sigma} \cdot \mathbf{u} \, \mathrm{d}\Omega \right| \leq c ||\boldsymbol{\sigma}||_\Sigma ||\mathbf{u}||_U \quad \forall \boldsymbol{\sigma} \in \Sigma, \, \forall \mathbf{u} \in U. \tag{1.76}$$

- The **ellipticity on the kernel condition** is verified, i.e., there exists a positive constant α such that

$$a(\boldsymbol{\tau}, \boldsymbol{\tau}) \geq \alpha ||\boldsymbol{\tau}||_\Sigma \qquad \forall \boldsymbol{\tau} \in K \tag{1.77}$$

  where

$$K := \{\boldsymbol{\tau} \in \Sigma \ : \ (\mathbf{div}\, \boldsymbol{\tau}, \mathbf{v}) = 0 \quad \forall \mathbf{v} \in U\}. \tag{1.78}$$

  Therefore, it is sufficient to require that the bilinear form $a(\cdot, \cdot)$ is coercive on the kernel K and not on the whole space Σ.

- The **inf-sup condition** is satisfied, i.e., there exists a constant $\beta > 0$ such that

$$\sup_{\boldsymbol{\tau} \in \Sigma, \boldsymbol{\tau} \neq \mathbf{0}} \frac{(\mathbf{div}\, \boldsymbol{\tau}, \mathbf{v})}{||\boldsymbol{\tau}||_\Sigma} \geq \beta ||\mathbf{v}||_U \qquad \forall \mathbf{v} \in U. \tag{1.79}$$

Hence the problem has a unique solution $(\boldsymbol{\sigma}, \mathbf{u})$ such that

$$||\boldsymbol{\sigma}||_\Sigma + ||\mathbf{u}||_U \leq C ||\mathbf{f}||_0. \tag{1.80}$$

Chapter 2

A three-dimensional low-order Virtual Element Method

In this chapter, we present a Virtual Element Method for three-dimensional elasticity problems based on the Hellinger-Reissner variational principle. More precisely, in the framework of small displacements and small deformations, we propose a conforming low-order scheme with a-priori symmetric stresses.

As it is well known, in the Finite Element approach, designing a conforming method that preserves the symmetry of the stresses is not at all a trivial task. The reason for this difficulty stands in the local polynomial approximation, which forces us to consider quite cumbersome schemes, especially for three-dimensional problems. Hence, to avoid these troubles, we exploit the flexibility of the Virtual Element technology to approximate the stress field, while for displacements, we use a suitable polynomial approximation.

Recently for these problems, some Virtual Element schemes have been proposed and analyzed for the bi-dimensional case. In particular, in [15] the authors presented a low-order scheme, while in [16] they developed a family of VE schemes with different degrees of accuracy.

The aim of this chapter is to extend the analysis and the computational aspects of [15] to a three-dimensional case, designing and implementing a robust method both with respect to the different types of meshes and the compressibility parameter (the nearly incompressible materials are allowed). These aspects show that, even for tetrahedral or hexahedral meshes, the proposed VEM method is a valid alternative to the corresponding mixed Finite Element with $H(\mathbf{div})$-conformity for stress and L^2-conformity for displacements [6].

The outline of the chapter follows. Section 2.1 details the procedure of our discrete method, by describing all the relevant projectors, bilinear and linear forms, together the VEM approximation spaces. The stability and convergence analysis is developed in Section 2.2, while the numerical experiments, which confirm the theoretical predictions, are detailed in Section 2.3.

For the results of this chapter we refer to the paper [54].

2.1 The Virtual Element Method

In this section, we define our Virtual Element discretization of Problem (1.74). Let $\{\mathcal{T}_h\}_h$ be a sequence of decompositions of Ω into general polyhedral elements E satisfying the usual assumptions (**B1**), (**B2**), (**B3**). Given a polygonal face $f \in \partial E$, we use $\mathbf{x}$ and $\tilde{\mathbf{x}}$ to indicate the global and local coordinates of a generic point of f, respectively. This notation will be useful in the definition of the local degrees of freedom for the stress field. Moreover, given two quantities a and b, we use the notation $a \lesssim b$ to mean: there exists a constant C, independent of the mesh-size, such that $a \leq Cb$.

Our Virtual Element method is based on the following procedure [15].

1. Firstly, we approximate the tensor $\mathbb{D}$ with $\bar{\mathbb{D}}$, a suitable piecewise constant concerning the underlying mesh $\mathcal{T}_h$: for instance, we could take the local mean value of $\mathbb{D}$, component-wise. Hence, we consider the problem:

$$\begin{cases} \text{Find } (\bar{\boldsymbol{\sigma}}, \bar{\mathbf{u}}) \text{ such that} & \\ -\mathbf{div}\,\bar{\boldsymbol{\sigma}} = \mathbf{f} & \text{in } \Omega \\ \bar{\mathbb{D}}\bar{\boldsymbol{\sigma}} = \boldsymbol{\varepsilon}(\bar{\mathbf{u}}) & \text{in } \Omega \\ \bar{\mathbf{u}} = \mathbf{0} & \text{in } \partial\Omega. \end{cases} \tag{2.1}$$

2. Then, we approximate Problem (2.1) by an appropriate Virtual Element scheme which returns a discrete solution $(\boldsymbol{\sigma}_h, \mathbf{u}_h)$ satisfying

$$||\bar{\boldsymbol{\sigma}} - \boldsymbol{\sigma}_h||_\Sigma + ||\bar{\mathbf{u}} - \mathbf{u}_h||_0 \lesssim h. \tag{2.2}$$

We now show that, for smooth tensors $\mathbb{D}$, the discrete solution $(\boldsymbol{\sigma}_h, \mathbf{u}_h)$ is also a first order approximation of $(\boldsymbol{\sigma}, \mathbf{u})$, solution to the original Problem (1.66) with homogeneous Dirichlet boundary conditions. More precisely, we have the following result:

Proposition 2.1.1. *Let $(\boldsymbol{\sigma}, \mathbf{u})$ solve Problem (1.66) and let $(\bar{\boldsymbol{\sigma}}, \bar{\mathbf{u}})$ solve Problem (2.1). Let $\mathbb{D}$ a regular tensor such that each component $\mathbb{D}_{ijkl}$ of $\mathbb{D}$ satisfies the following condition*

$$\mathbb{D}_{ijkl_{|E}} \in H^1(E) \text{ for every } E \in \mathcal{T}_h, \tag{2.3}$$

then we have

$$||\boldsymbol{\sigma} - \bar{\boldsymbol{\sigma}}||_\Sigma + ||\mathbf{u} - \bar{\mathbf{u}}||_1 \lesssim \left(\sum_{E \in \mathcal{T}_h} h_E^2 |\mathbb{D}|_{1,E}^2 \right)^{1/2} ||\mathbf{f}||_0. \tag{2.4}$$

In addition, if $(\boldsymbol{\sigma}_h, \mathbf{u}_h)$ fulfils (2.2), then

$$||\boldsymbol{\sigma} - \boldsymbol{\sigma}_h||_\Sigma + ||\mathbf{u} - \mathbf{u}_h||_0 \lesssim h. \tag{2.5}$$

Proof. Let's start to prove the inequality (2.4). Using the uniform boundedness and positive-definiteness of $\mathbb{D}$, together with the Korn's inequality, we have

$$||\boldsymbol{\sigma}-\bar{\boldsymbol{\sigma}}||_0^2+||\mathbf{u}-\bar{\mathbf{u}}||_1^2 \lesssim \int_\Omega \mathbb{D}(\boldsymbol{\sigma}-\bar{\boldsymbol{\sigma}}):(\boldsymbol{\sigma}-\bar{\boldsymbol{\sigma}})\,\mathrm{d}\Omega+\int_\Omega \mathbb{C}(\boldsymbol{\varepsilon}(\mathbf{u}-\bar{\mathbf{u}})):(\boldsymbol{\varepsilon}(\mathbf{u}-\bar{\mathbf{u}}))\,\mathrm{d}\Omega. \quad (2.6)$$

By the Hyper-Circle Theorem of Prager and Synge (see [76]), it holds

$$\int_\Omega \mathbb{D}(\boldsymbol{\sigma}-\bar{\boldsymbol{\sigma}}):(\boldsymbol{\sigma}-\bar{\boldsymbol{\sigma}})\,\mathrm{d}\Omega+\int_\Omega \mathbb{C}(\boldsymbol{\varepsilon}(\mathbf{u}-\bar{\mathbf{u}})):(\boldsymbol{\varepsilon}(\mathbf{u}-\bar{\mathbf{u}}))\,\mathrm{d}\Omega=\int_\Omega \mathbb{D}(\bar{\boldsymbol{\sigma}}-\mathbb{C}\boldsymbol{\varepsilon}(\bar{\mathbf{u}})):(\bar{\boldsymbol{\sigma}}-\mathbb{C}\boldsymbol{\varepsilon}(\bar{\mathbf{u}}))\,\mathrm{d}\Omega. \quad (2.7)$$

Now we notice that $\mathbb{D}(\bar{\boldsymbol{\sigma}}-\mathbb{C}\boldsymbol{\varepsilon}(\bar{\mathbf{u}}))=\mathbb{D}(\bar{\boldsymbol{\sigma}}-\mathbb{C}\bar{\mathbb{D}}\bar{\boldsymbol{\sigma}})=(\mathbb{D}-\bar{\mathbb{D}})\bar{\boldsymbol{\sigma}}$, see (2.1). Hence, thanks to the uniform boundedness of $\mathbb{C}$ and standard approximation results, we infer

$$\begin{aligned}\int_\Omega \mathbb{D}(\bar{\boldsymbol{\sigma}}-\mathbb{C}\boldsymbol{\varepsilon}(\bar{\mathbf{u}})):(\bar{\boldsymbol{\sigma}}-\mathbb{C}\boldsymbol{\varepsilon}(\bar{\mathbf{u}}))\,\mathrm{d}\Omega &= \int_\Omega (\mathbb{D}-\bar{\mathbb{D}})\bar{\boldsymbol{\sigma}}:\mathbb{C}((\mathbb{D}-\bar{\mathbb{D}})\bar{\boldsymbol{\sigma}})\,\mathrm{d}\Omega\\ &\lesssim ||(\mathbb{D}-\bar{\mathbb{D}})\bar{\boldsymbol{\sigma}}||_0^2\\ &\lesssim \left(\sum_{E\in\mathcal{T}_h} h_E^2|\mathbb{D}|_{1,E}^2\right)||\bar{\boldsymbol{\sigma}}||_0^2.\end{aligned} \quad (2.8)$$

Furthermore, we notice that $\mathbf{div}(\boldsymbol{\sigma}-\bar{\boldsymbol{\sigma}})=\mathbf{0}$. Therefore, combining (2.6), (2.7) and (2.8), and employing the stability bound $||\bar{\boldsymbol{\sigma}}||_0 \lesssim ||\mathbf{f}||_0$ we obtain

$$||\boldsymbol{\sigma}-\bar{\boldsymbol{\sigma}}||_\Sigma^2+||\mathbf{u}-\bar{\mathbf{u}}||_1^2 \lesssim \left(\sum_{E\in\mathcal{T}_h} h_E^2|\mathbb{D}|_{1,E}^2\right)||\mathbf{f}||_0^2, \quad (2.9)$$

and thus we have estimate (2.4). From (2.9) we immediately get

$$||\boldsymbol{\sigma}-\bar{\boldsymbol{\sigma}}||_\Sigma+||\mathbf{u}-\bar{\mathbf{u}}||_0 \lesssim h\,||\mathbf{f}||_0, \quad (2.10)$$

and estimate (2.5) now follows using (2.2) and the triangle inequality. □

Remark 10. *Proposition 2.1.1 shows that one may assume that $\mathbb{D}$ is piecewise constant from the beginning. Indeed, if an error bound like (2.2) holds true, then the convergence estimate (2.5) is also valid for $\mathbb{D}$ sufficiently regular, see (2.3). This is the approach we follow in the sequel of the chapter and thesis.*

2.1.1 The local spaces

To describe the local spaces employed in the VEM proposed scheme, we firstly introduce two spaces: $RM(E)$ and $T_h(f)$.

Space $RM(E)$. It is the space of local infinitesimal rigid body motions:

$$RM(E):=\left\{\mathbf{r}(\mathbf{x})=\boldsymbol{\alpha}+\boldsymbol{\omega}\wedge\left(\mathbf{x}-\mathbf{x}_E\right)\ \text{ s.t. } \boldsymbol{\alpha},\ \boldsymbol{\omega}\in\mathbb{R}^3\right\}, \quad (2.11)$$

whose dimension is 6.

Space $T_h(f)$. For each face $f \in \partial E$, we introduce

$$T_h(f) := \Big\{ \boldsymbol{\psi}(\tilde{\mathbf{x}}) = \mathbf{t}_f + a\Big[\mathbf{n}_f \wedge (\mathbf{x}(\tilde{\mathbf{x}}) - \mathbf{x}_f)\Big] + p_1(\tilde{\mathbf{x}})\mathbf{n}_f, \text{ s.t. } a \in \mathbb{R},\ p_1(\tilde{\mathbf{x}}) \in \mathcal{P}_1(f) \Big\}, \tag{2.12}$$

where $\mathbf{n}_f$ the outward normal to the face f, and $\mathbf{t}_f$ is an arbitrary vector tangent to the face f. Above, $\mathbf{x}(\tilde{\mathbf{x}})$ is the three dimensional position vector of a point on f, determined by the two local coordinates $\tilde{\mathbf{x}}$. The dimension of such a space is 6, indeed:

- The three dimensional tangent vector $\mathbf{t}$ is determined by a linear combination of two given linearly independent tangential vectors $\mathbf{t}_1$ and $\mathbf{t}_2$, i.e.

$$\mathbf{t} = b_1\mathbf{t}_1 + b_2\mathbf{t}_2.$$

- The rotational term $a\Big[\mathbf{n}_f \wedge (\mathbf{x}(\tilde{\mathbf{x}}) - \mathbf{x}_f)\Big]$ is determined by a single scalar value $a \in \mathbb{R}$.
- The polynomial $p_1(\tilde{\mathbf{x}}) \in \mathcal{P}_1(f)$ is a two variable polynomial with respect to the local face coordinate system so it is determined by three parameters, and here we use:

$$p_1(\tilde{\mathbf{x}}) = c_1 + c_2(\tilde{x} - \tilde{x}_f) + c_3(\tilde{y} - \tilde{y}_f).$$

Therefore, this space consists of vector functions whose tangential component is a 2D face rigid body motion (the first two terms of (2.12)), while the normal component is a linear two-variable polynomial (the last term of (2.12)), see Figure 2.1.

Stress space. We are now ready to introduce our local approximation space for the stress field:

$$\begin{aligned}\Sigma_h(E) := \Big\{ \boldsymbol{\tau}_h \in & H(\mathbf{div}; E) \ : \ \exists\, \mathbf{w}^* \in \Big[H^1(E)\Big]^3 \text{ such that } \boldsymbol{\tau}_h = \mathbb{C}\boldsymbol{\varepsilon}(\mathbf{w}^*); \\ & (\boldsymbol{\tau}_h\, \mathbf{n})_{|f} \in T_h(f) \quad \forall f \in \partial E; \quad \mathbf{div}\, \boldsymbol{\tau}_h \in RM(E) \Big\}.\end{aligned} \tag{2.13}$$

Accordingly, for the local space $\Sigma_h(E)$ the following degrees of freedom can be taken, see also (2.12).

- For each face f of the element E, the three degrees of freedom which determine the tangential component of the tractions:

$$\boldsymbol{\tau}_h \longrightarrow \int_f (\boldsymbol{\tau}_h\, \mathbf{n})_{|f} \cdot \Big[\boldsymbol{\theta}_f + \alpha\Big[\mathbf{n}_f \wedge (\mathbf{x}(\tilde{\mathbf{x}}) - \mathbf{x}_f)\Big]\Big]\, \mathrm{d}f. \tag{2.14}$$

  Above, $\alpha \in \mathbb{R}$ and $\boldsymbol{\theta}_f$ is an arbitrary vector tangential to the face f.

- For each face f of the element E, the three degrees of freedom which determine the normal component of the tractions:

$$\boldsymbol{\tau}_h \longrightarrow \int_f (\boldsymbol{\tau}_h\, \mathbf{n})_{|f} \cdot \Big[q_1(\tilde{\mathbf{x}})\mathbf{n}_f\Big]\, \mathrm{d}f \qquad \forall\, q_1(\tilde{\mathbf{x}}) \in \mathcal{P}_1(f). \tag{2.15}$$

Therefore, we infer that the dimension of the space (2.13) is

$$\dim(\Sigma_h(E)) = 6\, n_f^E,$$

n_f^E being the number of element faces.

Proposition 2.1.2. *Let $\boldsymbol{\tau}_h \in \Sigma_h(E)$, then $\mathbf{div}\,\boldsymbol{\tau}_h$ is completely determined by $(\boldsymbol{\tau}_h\,\mathbf{n})_{|f}$, with $f \in \partial E$ face of E. More precisely, setting (cf (2.11))*

$$\mathbf{div}\,\boldsymbol{\tau}_h = \boldsymbol{\alpha}_E + \boldsymbol{\omega}_E \wedge \Big(\mathbf{x} - \mathbf{x}_E\Big), \tag{2.16}$$

it holds

$$\boldsymbol{\alpha}_E = \frac{1}{|E|}\left(\sum_{f\in\partial E}\int_f (\boldsymbol{\tau}_h\,\mathbf{n})\ df\right), \tag{2.17}$$

and $\boldsymbol{\omega}_E$ is the unique solution of the 3×3 linear system

$$\int_E \Big(\mathbf{x} - \mathbf{x}_E\Big) \wedge \Big[\boldsymbol{\omega}_E \wedge \Big(\mathbf{x} - \mathbf{x}_E\Big)\Big]\ dE = \sum_{f\in\partial E}\int_f \Big(\mathbf{x} - \mathbf{x}_E\Big) \wedge (\boldsymbol{\tau}_h\mathbf{n})\ df. \tag{2.18}$$

Proof. Since $\boldsymbol{\tau}_h \in \Sigma_h(E)$, we have $\mathbf{div}\,\boldsymbol{\tau}_h \in RM(E)$ and $(\boldsymbol{\tau}_h\,\mathbf{n})_{|f} = \boldsymbol{\psi}(\tilde{\mathbf{x}})_{|f} \in T_h(f)$, for $f \in \partial E$. Then, denoting with $\boldsymbol{\varphi} : \partial E \to \mathbb{R}^3$ the function such that $\boldsymbol{\varphi}_{|f} := \boldsymbol{\psi}(\tilde{\mathbf{x}})_{|f}$, the integration by parts:

$$\int_E \mathbf{div}\,\boldsymbol{\tau}_h \cdot \mathbf{r}\ \mathrm{d}E = \int_{\partial E} \boldsymbol{\varphi}\cdot\mathbf{r}\ \mathrm{d}f \qquad \forall \mathbf{r} \in RM(E), \tag{2.19}$$

allows to compute $\mathbf{div}\,\boldsymbol{\tau}_h$ using the degrees of freedom of the space $T_h(f)$.

Testing (2.19) with constant functions $\mathbf{r}(\mathbf{x}) = \boldsymbol{\alpha}$ and recalling (2.16), we have

$$\int_E \boldsymbol{\alpha}_E\cdot\boldsymbol{\alpha}\ \mathrm{d}E = \int_{\partial E}\boldsymbol{\varphi}_{|f}\cdot\boldsymbol{\alpha}\ \mathrm{d}f = \Big(\sum_{f\in\partial E}\int_f(\boldsymbol{\tau}_h\,\mathbf{n})\ \mathrm{d}f\Big)\cdot\boldsymbol{\alpha} \qquad \forall\boldsymbol{\alpha}\in\mathbb{R}^3.$$

Hence, we obtain

$$\boldsymbol{\alpha}_E = \frac{1}{|E|}\Big(\sum_{f\in\partial E}\int_f(\boldsymbol{\tau}_h\,\mathbf{n})\ \mathrm{d}f\Big).$$

Now, we test (2.19) selecting $\mathbf{r}(\mathbf{x}) = \boldsymbol{\omega}\wedge\Big(\mathbf{x}-\mathbf{x}_E\Big)$. We have

$$\int_E \Big[\boldsymbol{\omega}_E\wedge\Big(\mathbf{x}-\mathbf{x}_E\Big)\Big]\cdot\Big[\boldsymbol{\omega}\wedge\Big(\mathbf{x}-\mathbf{x}_E\Big)\Big]\ \mathrm{d}E = \sum_{f\in\partial E}\int_f\boldsymbol{\varphi}_{|f}\cdot\Big[\boldsymbol{\omega}\wedge\Big(\mathbf{x}-\mathbf{x}_E\Big)\Big]\ \mathrm{d}f \quad \forall\boldsymbol{\omega}\in\mathbb{R}^3, \tag{2.20}$$

i.e.

$$\boldsymbol{\omega}\cdot\left(\int_E\Big(\mathbf{x}-\mathbf{x}_E\Big)\wedge\Big[\boldsymbol{\omega}_E\wedge\Big(\mathbf{x}-\mathbf{x}_E\Big)\Big]\ \mathrm{d}E\right) = \boldsymbol{\omega}\cdot\left(\sum_{f\in\partial E}\int_f\Big(\mathbf{x}-\mathbf{x}_E\Big)\wedge\boldsymbol{\varphi}_{|f}\ \mathrm{d}f\right) \quad \forall\boldsymbol{\omega}\in\mathbb{R}^3.$$

We then infer that $\boldsymbol{\omega}_E$ satisfies

$$\int_E \left(\mathbf{x}-\mathbf{x}_E\right) \wedge \left[\boldsymbol{\omega}_E \wedge \left(\mathbf{x}-\mathbf{x}_E\right)\right] \, \mathrm{d}E = \sum_{f\in\partial E} \int_f \left(\mathbf{x}-\mathbf{x}_E\right) \wedge \left(\boldsymbol{\tau}_h \, \mathbf{n}\right) \, \mathrm{d}f,$$

i.e. $\boldsymbol{\omega}_E$ solves system (2.18). We also notice that from (2.20) we deduce that the linear operator

$$\boldsymbol{\omega}_E \longmapsto \int_E \left(\mathbf{x}-\mathbf{x}_E\right) \wedge \left[\boldsymbol{\omega}_E \wedge \left(\mathbf{x}-\mathbf{x}_E\right)\right] \mathrm{d}E$$

is symmetric and positive definite. □

Displacement space. The local approximation space for the displacement field is defined by, see (2.11):

$$U_h(E) = \left\{ \mathbf{v}_h \in \left[L^2(E)\right]^3 \; : \; \mathbf{v}_h \in RM(E) \right\}. \tag{2.21}$$

Accordingly, for the local space $U_h(E)$ the following degrees of freedom can be taken:

$$\mathbf{v}_h \longrightarrow \int_E \mathbf{v}_h \cdot \mathbf{r} \, \mathrm{d}E \qquad \forall \, \mathbf{r} \in RM(E). \tag{2.22}$$

It follows that $\dim(U_h(E)) = 6$, see Figure 2.1.

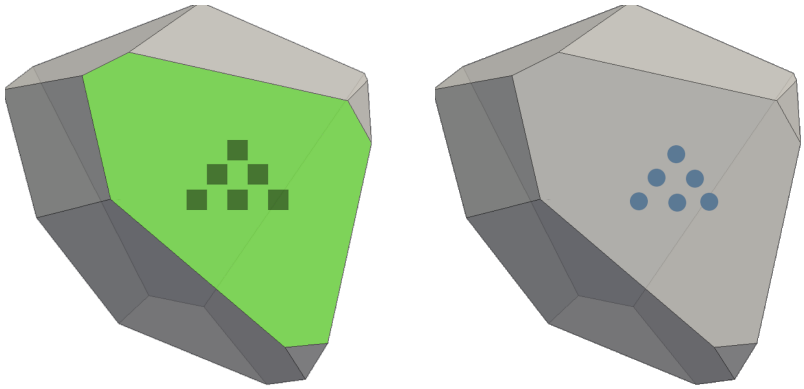

Stress Dofs Displacement Dofs

Figure 2.1: Overview of the local degrees of freedom. On the left, the stress degrees of freedom on a fixed face (green face); on the right the displacement degrees of freedom.

2.1.2 The local forms

In this section we introduce the VEM counterparts of the local forms associated with the continuous problem.

The local mixed term. Given $E \in \mathcal{T}_h$, we begin by noticing that the term

$$(\mathbf{div}\,\boldsymbol{\tau}_h, \mathbf{v}_h)_E = \int_E \mathbf{div}\,\boldsymbol{\tau}_h \cdot \mathbf{v}_h \,\mathrm{d}E$$

is computable for every $\boldsymbol{\tau}_h \in \Sigma_h(E)$ and $\mathbf{v}_h \in U_h(E)$ via degrees of freedom. For this reason, we do not need to introduce any approximation of the terms $(\mathbf{div}\,\boldsymbol{\tau}, \mathbf{u})$ and $(\mathbf{div}\,\boldsymbol{\sigma}, \mathbf{v})$ in problem (1.74).

The local bilinear form $a_E(\cdot,\cdot)$. The local bilinear form

$$a_E(\boldsymbol{\sigma}_h, \boldsymbol{\tau}_h) = \int_E \mathbb{D}\boldsymbol{\sigma}_h : \boldsymbol{\tau}_h \,\mathrm{d}E$$

is not computable for a general couple $(\boldsymbol{\sigma}_h, \boldsymbol{\tau}_h) \in \Sigma_h(E) \times \Sigma_h(E)$. As it is standard in the VEM procedure (cf. [22]), we build a computable approximation of the bilinear form by defining a suitable projection operator onto local polynomial functions. In our case, we introduce $\Pi_E : \Sigma_h(E) \to [\mathcal{P}_0(E)]^{3\times 3}_s$, by requiring

$$\int_E \Pi_E\,\boldsymbol{\tau}_h : \boldsymbol{\pi}_0 = \int_E \boldsymbol{\tau}_h : \boldsymbol{\pi}_0 \,\mathrm{d}E \qquad \forall \boldsymbol{\pi}_0 \in [\mathcal{P}_0(E)]^{3\times 3}_s\,. \tag{2.23}$$

This is a projection operator onto the constant symmetric tensor functions and it is computable. Indeed, we notice that each $\boldsymbol{\pi}_0 \in [\mathcal{P}_0(E)]^{3\times 3}_s$ can be written as the symmetric gradient of a linear vectorial function, i.e. $\boldsymbol{\pi}_0 = \boldsymbol{\varepsilon}(\mathbf{p}_1)$, with $\mathbf{p}_1 \in [\mathcal{P}_1(E)]^3$. Hence, using the divergence theorem, the right-hand side of (2.23) becomes

$$\int_E \boldsymbol{\tau}_h : \boldsymbol{\pi}_0 \,\mathrm{d}E = \int_E \boldsymbol{\tau}_h : \boldsymbol{\varepsilon}(\mathbf{p}_1) \,\mathrm{d}E = -\int_E \mathbf{div}\,\boldsymbol{\tau}_h \cdot \mathbf{p}_1 \,\mathrm{d}E + \int_{\partial E} (\boldsymbol{\tau}_h \mathbf{n}) \cdot \mathbf{p}_1 \,\mathrm{d}f$$

which is clearly computable (see also Proposition 2.1.2). Then, the approximation of $a_E(\cdot,\cdot)$ reads:

$$\begin{aligned} a^h_E(\boldsymbol{\sigma}_h, \boldsymbol{\tau}_h) &:= a_E(\Pi_E\,\boldsymbol{\sigma}_h, \Pi_E \boldsymbol{\tau}_h) + s_E\left((I-\Pi_E)\boldsymbol{\sigma}_h, (I-\Pi_E)\boldsymbol{\tau}_h\right) \\ &= \int_E \mathbb{D}(\Pi_E \boldsymbol{\sigma}_h) : (\Pi_E \boldsymbol{\tau}_h) \,\mathrm{d}E + s_E\left((I-\Pi_E)\boldsymbol{\sigma}_h, (I-\Pi_E)\boldsymbol{\tau}_h\right), \end{aligned} \tag{2.24}$$

where $s_E(\cdot,\cdot)$ is a suitable stabilization term. In this chapter we propose the following choice:

$$s_E(\boldsymbol{\sigma}_h, \boldsymbol{\tau}_h) := \kappa_E\, h_E \int_{\partial E} (\boldsymbol{\sigma}_h \mathbf{n}) \cdot \boldsymbol{\tau}_h \mathbf{n} \,\mathrm{d}f, \tag{2.25}$$

Above, κ_E is a positive constant to be chosen according to $\mathbb{D}$. For instance, in the numerical examples of Section 2.3, κ_E is set equal to $\frac{1}{2}\mathrm{tr}(\mathbb{D}_{|E})$. However, any norm of $\mathbb{D}_{|E}$ can be used. A possible variant of (2.25) is

$$s_E(\boldsymbol{\sigma}_h, \boldsymbol{\tau}_h) := \kappa_E \sum_{f \in \partial E} h_f \int_f (\boldsymbol{\sigma}_h \mathbf{n}) \cdot \boldsymbol{\tau}_h \mathbf{n} \,\mathrm{d}f.$$

The local loading term. We split the load term on each element and we have

$$(\mathbf{f}, \mathbf{v}_h) = \int_\Omega \mathbf{f} \cdot \mathbf{v}_h \, \mathrm{d}\Omega = \sum_{E \in \mathcal{T}_h} \int_E \mathbf{f} \cdot \mathbf{v}_h \, \mathrm{d}E.$$

Since $\mathbf{v}_h \in RM(E)$, the right-hand side is computable via quadrature rules for polyhedral domains.

Remark 11. *Since this integral involves a sufficiently regular function* $\mathbf{f}$*, to get a "good" approximation we exploit a quadrature rule of high degree. For the numerical examples in Section 2.3, we use a quadrature rule of degree 4.*

2.1.3 The discrete scheme

Starting from the local spaces and local terms introduced in the previous sections, we can set the global problem. More specifically, we introduce a global approximation space for the stress field, by glueing the local approximation spaces, see (2.13):

$$\Sigma_h = \left\{ \boldsymbol{\tau}_h \in H(\mathbf{div}; \Omega) \ : \ \boldsymbol{\tau}_{h|E} \in \Sigma_h(E) \quad \forall E \in \mathcal{T}_h \right\}. \tag{2.26}$$

The global stress degrees of freedom are obtained by glueing together, on each internal face of the mesh $\mathcal{T}_h$, the local degrees of freedom. Given an internal face, this accounts for selecting one of the two normals once and for all, and then consider the corresponding functionals (2.14) and (2.15). For the global approximation of the displacement field, we take, see (2.21):

$$U_h = \left\{ \mathbf{v}_h \in \left[L^2(\Omega) \right]^3 \ : \ \mathbf{v}_{h|E} \in U_h(E) \quad \forall E \in \mathcal{T}_h \right\}. \tag{2.27}$$

Since no inter-element continuity is required, the global displacement degrees of freedom are simply obtained by collecting the local degrees of freedom (2.22).

Now, given a local approximation of $a_E(\cdot, \cdot)$, see (2.24), we set

$$a_h(\boldsymbol{\sigma}_h, \boldsymbol{\tau}_h) := \sum_{E \in \mathcal{T}_h} a_E^h(\boldsymbol{\sigma}_h, \boldsymbol{\tau}_h). \tag{2.28}$$

The method we consider is then defined by (cf. Problem (1.74) and Remark 9):

$$\begin{cases} \text{Find } (\boldsymbol{\sigma}_h, \mathbf{u}_h) \in \Sigma_h \times U_h \text{ such that} & \\ a_h(\boldsymbol{\sigma}_h, \boldsymbol{\tau}_h) + (\mathbf{div}\, \boldsymbol{\tau}_h, \mathbf{u}_h) = 0 & \forall \boldsymbol{\tau}_h \in \Sigma_h \\ (\mathbf{div}\, \boldsymbol{\sigma}_h, \mathbf{v}_h) = -(\mathbf{f}, \mathbf{v}_h) & \forall \mathbf{v}_h \in U_h. \end{cases} \tag{2.29}$$

2.2 Stability and convergence analysis

Since some results of the analysis follows the guidelines of the theory developed in [15], in this section we do not provide full details of all the proofs. First, for all $E \in \mathcal{T}_h$, we introduce the space:

$$\widetilde{\Sigma}(E) := \left\{ \boldsymbol{\tau} \in H(\mathbf{div}; E) \ : \ \exists \mathbf{w} \in \left[H^1(E)\right]^3 \text{ such that } \boldsymbol{\tau} = \mathbb{C}\boldsymbol{\varepsilon}(\mathbf{w}) \right\}. \tag{2.30}$$

The global space $\widetilde{\Sigma}$ is defined as

$$\widetilde{\Sigma} := \left\{ \boldsymbol{\tau} \in H(\mathbf{div}; \Omega) \ : \ \exists \mathbf{w} \in \left[H^1(\Omega)\right]^3 \text{ such that } \boldsymbol{\tau} = \mathbb{C}\boldsymbol{\varepsilon}(\mathbf{w}) \right\}.$$

In the sequel, given a measurable subset $A \subseteq \Omega$ and $r > 2$, we will use the following space

$$W^r(A) := \left\{ \boldsymbol{\tau} \ : \boldsymbol{\tau} \in [L^r(A)]^{3\times 3}_s \ , \ \mathbf{div}\, \boldsymbol{\tau} \in \left[L^2(A)\right]^3 \right\},$$

equipped with the obvious norm.

2.2.1 An interpolation operator for stresses

We introduce the local interpolation operator $\mathcal{I}_E : W^r(E) \to \Sigma_h(E)$, defined by:

$$\int_{\partial E} (\mathcal{I}_E \boldsymbol{\tau})\mathbf{n} \cdot \boldsymbol{\varphi}_* \, \mathrm{d}f = \int_{\partial E} (\boldsymbol{\tau}\, \mathbf{n}) \cdot \boldsymbol{\varphi}_* \, \mathrm{d}f \qquad \forall \boldsymbol{\varphi}_* \in R_*(\partial E), \tag{2.31}$$

where:

$$R_*(\partial E) = \left\{ \boldsymbol{\varphi}_* \in \left[L^2(\partial E)\right]^3 \ : \ \boldsymbol{\varphi}_{*|f}(\tilde{\mathbf{x}}) = \boldsymbol{\gamma}_f + [\boldsymbol{\delta}_f \wedge (\mathbf{x}(\tilde{\mathbf{x}}) - \mathbf{x}_E)] \,, \right. \\ \left. \boldsymbol{\gamma}_f, \, \boldsymbol{\delta}_f \in \mathbb{R}^3, \ \forall f \in \partial E \right\}. \tag{2.32}$$

We remark that if $\boldsymbol{\tau}$ is not sufficiently regular, the integral in the right-hand side of (2.31) is intended as a duality between $\left[W^{-\frac{1}{r},r}(\partial E)\right]^3$ and $\left[W^{\frac{1}{r},r'}(\partial E)\right]^3$. Instead, if $\boldsymbol{\tau}$ is a regular function, the above condition is equivalent to require:

$$\begin{cases} \displaystyle\int_f (\mathcal{I}_E \boldsymbol{\tau})\mathbf{n} \cdot \boldsymbol{\alpha} \, \mathrm{d}f = \int_f (\boldsymbol{\tau}\, \mathbf{n}) \cdot \boldsymbol{\alpha} \, \mathrm{d}f & \forall \boldsymbol{\alpha} \in \mathbb{R}^3; \\ \displaystyle\int_f (\mathcal{I}_E \boldsymbol{\tau})\mathbf{n} \cdot [\boldsymbol{\omega} \wedge (\mathbf{x}(\tilde{\mathbf{x}}) - \mathbf{x}_E)] \, \mathrm{d}f = \int_f (\boldsymbol{\tau}\, \mathbf{n}) \cdot [\boldsymbol{\omega} \wedge (\mathbf{x}(\tilde{\mathbf{x}}) - \mathbf{x}_E)] \, \mathrm{d}f & \forall \boldsymbol{\omega} \in \mathbb{R}^3; \end{cases} \tag{2.33}$$

for each face $f \in \partial E$.

We now show that $\mathcal{I}_E \boldsymbol{\tau} \in \Sigma_h(E)$ is well-defined by conditions (2.31). Indeed this is an immediate consequence of the following Lemma.

Lemma 2.2.1. *If $\boldsymbol{\tau}_h \in \Sigma_h(E)$ is such that*

$$\int_{\partial E} (\boldsymbol{\tau}_h\, \mathbf{n}) \cdot \boldsymbol{\varphi}_* \ df = 0 \qquad \forall \boldsymbol{\varphi}_* \in R_*(\partial E),$$

then $\boldsymbol{\tau}_h = \mathbf{0}$.

Proof. Recalling (2.13), Proposition 2.1.2 and (2.32), it is sufficient to prove that, given a face $f \in \partial E$, conditions

$$\int_f (\boldsymbol{\tau}_h \, \mathbf{n}) \cdot \Big[\boldsymbol{\gamma}_f + \boldsymbol{\delta}_f \wedge (\mathbf{x}(\tilde{\mathbf{x}}) - \mathbf{x}_E) \Big] \, \mathrm{d}f = 0 \qquad \forall \boldsymbol{\gamma}_f, \, \boldsymbol{\delta}_f \in \mathbb{R}^3 \tag{2.34}$$

imply $(\boldsymbol{\tau}_h \, \mathbf{n})_{|f} = \mathbf{0}$. To this end, we first set (cf. (2.12))

$$(\boldsymbol{\tau}_h \, \mathbf{n})_{|f}(\tilde{\mathbf{x}}) = \, \mathbf{t}_f + a \Big[\mathbf{n}_f \wedge (\mathbf{x}(\tilde{\mathbf{x}}) - \mathbf{x}_f) \Big] + p_1(\tilde{\mathbf{x}}) \mathbf{n}_f, \tag{2.35}$$

with $\mathbf{t}_f$ an arbitrary constant vector tangent to the face f, $a \in \mathbb{R}$, $\mathbf{n}_f$ the outward normal vector and

$$p_1(\tilde{\mathbf{x}}) = c_1 + c_2(\tilde{x} - \tilde{x}_f) + c_3(\tilde{y} - \tilde{y}_f) \qquad c_i \in \mathbb{R} \quad i = 1, 2, 3.$$

Choosing $\boldsymbol{\delta}_f = \mathbf{0}$ and $\boldsymbol{\gamma}_f$ arbitrary in (2.34), and considering (2.35), we infer $\mathbf{t}_f = \mathbf{0}$ and $c_1 = 0$. Hence, it holds:

$$(\boldsymbol{\tau}_h \, \mathbf{n})_{|f}(\tilde{\mathbf{x}}) = \, a \Big[\mathbf{n}_f \wedge (\mathbf{x}(\tilde{\mathbf{x}}) - \mathbf{x}_f) \Big] + \Big(c_2(\tilde{x} - \tilde{x}_f) + c_3(\tilde{y} - \tilde{y}_f) \Big) \, \mathbf{n}_f. \tag{2.36}$$

We now select $\boldsymbol{\gamma}_f = \mathbf{0}$ and $\boldsymbol{\delta}_f = \mathbf{n}_f$ in (2.34). From (2.36) we get

$$a \int_f \Big[\mathbf{n}_f \wedge (\mathbf{x}(\tilde{\mathbf{x}}) - \mathbf{x}_f) \Big] \cdot \Big[\mathbf{n}_f \wedge (\mathbf{x}(\tilde{\mathbf{x}}) - \mathbf{x}_E) \Big] \mathrm{d}f = 0.$$

We have:

$$\begin{aligned}
&\int_f \Big[\mathbf{n}_f \wedge (\mathbf{x}(\tilde{\mathbf{x}}) - \mathbf{x}_f) \Big] \cdot \Big[\mathbf{n}_f \wedge (\mathbf{x}(\tilde{\mathbf{x}}) - \mathbf{x}_E) \Big] \mathrm{d}f = \\
&\int_f \Big[\mathbf{n}_f \wedge (\mathbf{x}(\tilde{\mathbf{x}}) - \mathbf{x}_f) \Big] \cdot \Big[\mathbf{n}_f \wedge ((\mathbf{x}(\tilde{\mathbf{x}}) - \mathbf{x}_f) + (\mathbf{x}_f - \mathbf{x}_E)) \Big] \mathrm{d}f = \\
&\int_f \Big| \mathbf{n}_f \wedge (\mathbf{x}(\tilde{\mathbf{x}}) - \mathbf{x}_f) \Big|^2 \mathrm{d}f + \int_f \Big[\mathbf{n}_f \wedge (\mathbf{x}(\tilde{\mathbf{x}}) - \mathbf{x}_f) \Big] \cdot \Big[\mathbf{n}_f \wedge (\mathbf{x}_f - \mathbf{x}_E) \Big] \mathrm{d}f = \\
&\int_f \Big| \mathbf{n}_f \wedge (\mathbf{x}(\tilde{\mathbf{x}}) - \mathbf{x}_f) \Big|^2 \mathrm{d}f > 0.
\end{aligned} \tag{2.37}$$

Above, we have used that $\mathbf{n}_f \wedge (\mathbf{x}_f - \mathbf{x}_E)$ is a constant vector and that $\mathbf{n}_f \wedge (\mathbf{x}(\tilde{\mathbf{x}}) - \mathbf{x}_f)$ has zero mean value over the face f, to infer that:

$$\int_f \Big[\mathbf{n}_f \wedge (\mathbf{x}(\tilde{\mathbf{x}}) - \mathbf{x}_f) \Big] \cdot \Big[\mathbf{n}_f \wedge (\mathbf{x}_f - \mathbf{x}_E) \Big] \mathrm{d}f = 0$$

From (2.37) we deduce $a = 0$, and therefore we get:

$$(\boldsymbol{\tau}_h \, \mathbf{n})_{|f}(\tilde{\mathbf{x}}) = \, \Big(c_2(\tilde{x} - \tilde{x}_f) + c_3(\tilde{y} - \tilde{y}_f) \Big) \, \mathbf{n}_f. \tag{2.38}$$

We finally select $\boldsymbol{\gamma}_f = \mathbf{0}$ and $\boldsymbol{\delta}_f = \mathbf{t}_f$ in (2.34), with $\mathbf{t}_f$ an arbitrary vector tangential to the face f. Thus, we obtain:

$$\int_f \Big(c_2(\tilde{x} - \tilde{x}_f) + c_3(\tilde{y} - \tilde{y}_f) \Big) \, \mathbf{n}_f \cdot [\mathbf{t}_f \wedge (\mathbf{x}(\tilde{\mathbf{x}}) - \mathbf{x}_E)] \, \mathrm{d}f = 0.$$

Using again $\mathbf{x}(\tilde{\mathbf{x}}) - \mathbf{x}_E = (\mathbf{x}(\tilde{\mathbf{x}}) - \mathbf{x}_f) + (\mathbf{x}_f - \mathbf{x}_E)$, we infer

$$\begin{aligned} T := \int_f \Big(c_2(\tilde{x} - \tilde{x}_f) + c_3(\tilde{y} - \tilde{y}_f)\Big)\, \mathbf{n}_f \cdot [\mathbf{t}_f \wedge (\mathbf{x}(\tilde{\mathbf{x}}) - \mathbf{x}_f)]\, \mathrm{d}f = \\ \int_f \Big(c_2(\tilde{x} - \tilde{x}_f) + c_3(\tilde{y} - \tilde{y}_f)\Big)\, (\mathbf{x}(\tilde{\mathbf{x}}) - \mathbf{x}_f) \cdot [\mathbf{n}_f \wedge \mathbf{t}_f]\, \mathrm{d}f = 0. \end{aligned} \tag{2.39}$$

We now choose $\mathbf{t}_f$ such that the (tangential to the face) vector $\mathbf{n}_f \wedge \mathbf{t}_f$ has components (c_2, c_3) with respect to the local coordinate system $(\tilde{x}, \tilde{y})$. Then, from (2.39) we get

$$T = \int_f \Big(c_2^2(\tilde{x} - \tilde{x}_f)^2 + c_3^2(\tilde{y} - \tilde{y}_f)^2\Big)\, \mathrm{d}f = 0,$$

which implies $c_2 = c_3 = 0$. Therefore, $(\boldsymbol{\tau}_h\, \mathbf{n})_{|f} = \mathbf{0}$, see (2.38), and the proof is complete. □

The global interpolation operator $\mathcal{I}_h : W^r(\Omega) \to \Sigma_h$ is then defined by glueing the local contributions provided by $\mathcal{I}_E$. More precisely, for every $\boldsymbol{\tau} \in W^r(\Omega)$ and $E \in \mathcal{T}_h$, we set

$$(\mathcal{I}_h \boldsymbol{\tau})_{|E} := \mathcal{I}_E \boldsymbol{\tau}_{|E}.$$

We now present the following Lemma, which is used to proof some error estimates for the interpolation operator.

Lemma 2.2.2. *Suppose that assumptions* (**B1**), (**B2**) *and* (**B3**) *are fulfilled. Given* $E \in \mathcal{T}_h$, *let* $\mathbf{w} \in [H^1(E)]^3$ *be a solution of the problem:*

$$\begin{cases} -\,\mathbf{div}(\mathbb{C}\boldsymbol{\varepsilon}(\mathbf{w})) = \mathbf{g} & \text{in } E \\ (\mathbb{C}\boldsymbol{\varepsilon}(\mathbf{w}))\mathbf{n} = \mathbf{h} & \text{on } \partial E, \end{cases} \tag{2.40}$$

where $\mathbf{g} \in [L^2(E)]^3$ *and* $\mathbf{h} \in [L^2(\partial E)]^3$ *satisfy the compatibility condition*

$$\int_E \mathbf{g} \cdot \mathbf{r}\ dE + \int_{\partial E} \mathbf{h} \cdot \mathbf{r}\ df = 0 \qquad \forall \mathbf{r} \in RM(E). \tag{2.41}$$

Then it holds:

$$||\mathbb{C}\boldsymbol{\varepsilon}(\mathbf{w})||_{0,E} \lesssim h_E ||\mathbf{g}||_{0,E} + h_E^{1/2} ||\mathbf{h}||_{0,\partial E}. \tag{2.42}$$

Proof. For the proof of this Lemma, one can use the same steps detailed in [15]. □

Therefore, we have the following error estimates for the interpolation operator $\mathcal{I}_h$.

Proposition 2.2.3. *Under assumptions* (**B1**), (**B2**) *and* (**B3**), *for the interpolation operator* $\mathcal{I}_E$ *defined in* (2.33), *the following estimates hold:*

$$||\boldsymbol{\tau} - \mathcal{I}_E \boldsymbol{\tau}||_{0,E} \lesssim h_E |\boldsymbol{\tau}|_{1,E} \qquad \forall \boldsymbol{\tau} \in \widetilde{\Sigma}(E) \cap \Big[H^1(E)\Big]^{3\times 3} \tag{2.43}$$

and

$$||\,\mathbf{div}(\boldsymbol{\tau} - \mathcal{I}_E \boldsymbol{\tau})||_{0,E} \lesssim h_E |\,\mathbf{div}\,\boldsymbol{\tau}|_{1,E} \quad \forall \boldsymbol{\tau} \in \widetilde{\Sigma}(E) \cap \Big[H^1(E)\Big]^{3\times 3} \text{ s.t. } \mathbf{div}\,\boldsymbol{\tau} \in [H^1(E)]^3. \tag{2.44}$$

Proof. Let $\boldsymbol{\tau} \in \widetilde{\Sigma}(E) \cap [H^1(E)]^{3\times 3}$, and let $\mathbf{w} \in [H^1(E)]^3$ be such that $\boldsymbol{\tau} = \mathbb{C}\boldsymbol{\varepsilon}(\mathbf{w})$, see (2.30). In addition, consider $\mathcal{I}_E\boldsymbol{\tau} \in \Sigma_h(E)$ and $\mathbf{w}^* \in [H^1(E)]^3$ such that $\mathcal{I}_E\boldsymbol{\tau} = \mathbb{C}\boldsymbol{\varepsilon}(\mathbf{w}^*)$, see (2.13). Hence, setting $\boldsymbol{\delta} := (\mathbf{w} - \mathbf{w}^*) \in [H^1(E)]^3$, it holds:

$$\boldsymbol{\tau} - \mathcal{I}_E\boldsymbol{\tau} = \mathbb{C}\boldsymbol{\varepsilon}(\boldsymbol{\delta}). \tag{2.45}$$

Furthermore, using (2.33), (2.16) and (2.18), we infer that $\boldsymbol{\delta} \in [H^1(E)]^3$ satisfies:

$$\begin{cases} \mathbf{div}(\mathbb{C}\boldsymbol{\varepsilon}(\boldsymbol{\delta})) = \mathbf{div}\,\boldsymbol{\tau} - (\boldsymbol{\alpha}_{\mathcal{I}_E} + \boldsymbol{\omega}_{\mathcal{I}_E} \wedge (\mathbf{x} - \mathbf{x}_E)) & \text{on } E \\ (\mathbb{C}\boldsymbol{\varepsilon}(\boldsymbol{\delta}))\mathbf{n} = \displaystyle\sum_{f\in\partial E} \left(\boldsymbol{\tau}\,\mathbf{n} - \frac{1}{|f|}\int_f (\boldsymbol{\tau}\,\mathbf{n})\,\mathrm{d}f \right) \chi_f & \text{on } \partial E, \end{cases} \tag{2.46}$$

where χ_f denotes the characteristic function of the face f and it holds

$$\boldsymbol{\alpha}_{\mathcal{I}_E} = \frac{1}{|E|} \left(\sum_{f\in\partial E} \int_f (\boldsymbol{\tau}\,\mathbf{n})\,\mathrm{d}f \right), \tag{2.47}$$

and $\boldsymbol{\omega}_{\mathcal{I}_E}$ is the unique solution of the 3×3 linear system

$$\int_E \left(\mathbf{x} - \mathbf{x}_E\right) \wedge \left[\boldsymbol{\omega}_{\mathcal{I}_E} \wedge \left(\mathbf{x} - \mathbf{x}_E\right)\right] \,\mathrm{d}E = \sum_{f\in\partial E} \int_f \left(\mathbf{x} - \mathbf{x}_E\right) \wedge (\boldsymbol{\tau}\,\mathbf{n})\,\mathrm{d}f. \tag{2.48}$$

Applying Lemma 2.2.2 with:

$$\begin{cases} \mathbf{g} := (\boldsymbol{\alpha}_{\mathcal{I}_E} + \boldsymbol{\omega}_{\mathcal{I}_E} \wedge (\mathbf{x} - \mathbf{x}_E)) - \mathbf{div}\,\boldsymbol{\tau} \\ \mathbf{h} := \displaystyle\sum_{f\in\partial E} \left(\boldsymbol{\tau}\,\mathbf{n} - \frac{1}{|f|}\int_f (\boldsymbol{\tau}\,\mathbf{n})\,\mathrm{d}f \right) \chi_f, \end{cases} \tag{2.49}$$

we get

$$||\boldsymbol{\tau} - \mathcal{I}_E\boldsymbol{\tau}||_{0,E} = ||\mathbb{C}\boldsymbol{\varepsilon}(\boldsymbol{\delta})||_{0,E} \lesssim h_E||\mathbf{g}||_{0,E} + h_E^{1/2}||\mathbf{h}||_{0,\partial E}. \tag{2.50}$$

We now estimate $\mathbf{g}$ and $\mathbf{h}$. We denote respectively with $\Pi_{0,E}$, $\Pi_{RM,E}$ and $\Pi_{0,\partial E}$ the L^2-projection operators onto the constant functions on E, onto the space $RM(E)$ (cf. (2.11)), and onto the piecewise constant functions on ∂E. Let's start with the first equation of (2.49). Using the divergence theorem and a direct computation we have

$$\Pi_{RM,E}\,\mathbf{div}\,\boldsymbol{\tau} = \boldsymbol{\alpha}_{\mathcal{I}_E} + \boldsymbol{\omega}_{\mathcal{I}_E} \wedge (\mathbf{x} - \mathbf{x}_E)\,. \tag{2.51}$$

Noting that $[\mathcal{P}_0(E)]^3 \subset RM(E)$, from the properties of the L^2-projection operator, we get

$$\begin{aligned} ||\mathbf{g}||_{0,E} &= ||\boldsymbol{\alpha}_{\mathcal{I}_E} + \boldsymbol{\omega}_{\mathcal{I}_E} \wedge (\mathbf{x} - \mathbf{x}_E) - \mathbf{div}\,\boldsymbol{\tau}||_{0,E} \\ &= ||\Pi_{RM,E}\,\mathbf{div}\,\boldsymbol{\tau} - \mathbf{div}\,\boldsymbol{\tau}||_{0,E} \\ &\leq ||\Pi_{0,E}\,\mathbf{div}\,\boldsymbol{\tau} - \mathbf{div}\,\boldsymbol{\tau}||_{0,E} \\ &\lesssim ||\,\mathbf{div}\,\boldsymbol{\tau}||_{0,E} \end{aligned} \tag{2.52}$$

and in particular

$$||\mathbf{g}||_{0,E} \lesssim h_E |\,\mathbf{div}\,\boldsymbol{\tau}|_{1,E}. \tag{2.53}$$

Now we focus our attention on the second equation of (2.49). We remark that:

$$\mathbf{h} = \sum_{f\in\partial E}\left(\boldsymbol{\tau}\,\mathbf{n} - \frac{1}{|f|}\int_f (\boldsymbol{\tau}\,\mathbf{n})\;\mathrm{d}f\right)\chi_f = \sum_{f\in\partial E}\left(\boldsymbol{\tau} - \frac{1}{|f|}\int_f \boldsymbol{\tau}\;\mathrm{d}f\right)\mathbf{n}\chi_f = (\boldsymbol{\tau} - \Pi_{0,\partial E}\boldsymbol{\tau})\,\mathbf{n}. \tag{2.54}$$

Hence, using a standard approximation estimate and a trace inequality, we get

$$\begin{aligned} ||\mathbf{h}||_{0,\partial E} = ||(\boldsymbol{\tau} - \Pi_{0,\partial E}\boldsymbol{\tau})\mathbf{n}||_{0,\partial E} &\leq ||\boldsymbol{\tau} - \Pi_{0,\partial E}\boldsymbol{\tau}||_{0,\partial E} \\ &\lesssim h_E^{1/2}|\boldsymbol{\tau}|_{1/2,\partial E} \\ &\lesssim h_E^{1/2}|\boldsymbol{\tau}|_{1,E}. \end{aligned} \tag{2.55}$$

Taking into account (2.52) and (2.55), from (2.50) we obtain estimate (2.43).

We now notice that from (2.45), (2.46) and (2.49), we have:

$$\mathbf{div}(\boldsymbol{\tau} - \mathcal{I}_E\boldsymbol{\tau}) = -\mathbf{g}. \tag{2.56}$$

Then, using (2.53), we immediately get (2.44).

□

2.2.2 The *ellipticity-on-the-kernel* and *inf-sup* conditions

The proposed approach satisfies the compatibility conditions. First, we notice that (see (2.26), (2.13) and (2.27), (2.21)):

$$\mathbf{div}(\Sigma_h) \subseteq U_h. \tag{2.57}$$

Then, we introduce the discrete kernel $K_h \subseteq \Sigma_h$:

$$K_h = \{\boldsymbol{\tau}_h \in \Sigma_h \,:\, (\mathbf{div}\,\boldsymbol{\tau}_h, \mathbf{v}_h) = 0 \quad \forall \mathbf{v}_h \in U_h\},$$

and we infer from (2.57) that $\boldsymbol{\tau}_h \in K_h$ implies $\mathbf{div}\,\boldsymbol{\tau}_h = \mathbf{0}$. Hence, it holds:

$$||\boldsymbol{\tau}_h||_\Sigma = ||\boldsymbol{\tau}_h||_0 \qquad \forall \boldsymbol{\tau}_h \in K_h. \tag{2.58}$$

This is essentially the property that leads to the following *ellipticity-on-the-kernel* condition.

Proposition 2.2.4. *For the method described in Section 2.1, there exists a constant $\alpha > 0$ such that*

$$a_h(\boldsymbol{\tau}_h, \boldsymbol{\tau}_h) \geq \alpha\,||\boldsymbol{\tau}_h||_\Sigma^2 \qquad \forall \boldsymbol{\tau}_h \in K_h. \tag{2.59}$$

Proof. Fix $E \in \mathcal{T}_h$. By (2.23), (2.24) and (2.25), using the techniques of [22, 45], one has:

$$||\boldsymbol{\tau}_h||^2_{0,E} \lesssim a^h_E(\boldsymbol{\tau}_h, \boldsymbol{\tau}_h) \lesssim ||\boldsymbol{\tau}_h||^2_{0,E} \qquad \forall \boldsymbol{\tau}_h \in \Sigma_h(E).$$

By recalling (2.28), we get the existence of $\alpha > 0$ such that

$$a_h(\boldsymbol{\tau}_h, \boldsymbol{\tau}_h) \geq \alpha \, ||\boldsymbol{\tau}_h||^2_0 \qquad \forall \boldsymbol{\tau}_h \in \Sigma_h.$$

Estimate (2.59) now follows by recalling (2.58). □

For the discrete *inf-sup* condition, we need the following *commuting diagram property.*

Proposition 2.2.5. *For the operator $\mathcal{I}_h : W^r(\Omega) \to \Sigma_h$ it holds:*

$$\mathbf{div}(\mathcal{I}_h \boldsymbol{\tau}) = \Pi_{RM}(\mathbf{div}\, \boldsymbol{\tau}) \qquad \forall \boldsymbol{\tau} \in W^r(\Omega), \tag{2.60}$$

where Π_{RM} denotes the L^2-projection operator onto the space of the rigid body motions, see (2.11).

Proof. It is sufficient to prove property (2.60) locally, in each element $E \in \mathcal{T}_h$. Fix now $\mathbf{r} \in RM(E)$ and $\boldsymbol{\tau} \in W^r(E)$. We have:

$$\begin{aligned} \int_E \mathbf{div}\, \boldsymbol{\tau} \cdot \mathbf{r} \, \mathrm{d}E &= \int_{\partial E} (\boldsymbol{\tau}\mathbf{n}) \cdot \mathbf{r} \, \mathrm{d}f \qquad\qquad \text{(by (2.33))} \\ &= \int_{\partial E} (\mathcal{I}_E \boldsymbol{\tau})\mathbf{n} \cdot \mathbf{r} \, \mathrm{d}f \qquad \text{(integration by parts)} \\ &= \int_E \mathbf{div}(\mathcal{I}_E \boldsymbol{\tau}) \cdot \mathbf{r} \, \mathrm{d}E \end{aligned} \tag{2.61}$$

From (2.61) and the definition of L^2-projection operator, we get $\mathbf{div}(\mathcal{I}_E \boldsymbol{\tau}) = \Pi_{RM}(\mathbf{div}\, \boldsymbol{\tau})$ on E. □

Using Proposition 2.2.5 the following discrete *inf-sup* condition follows from the theory developed in [15].

Proposition 2.2.6. *Suppose that assumptions* (**B1**), (**B2**) *and* (**B3**) *are fulfilled. Then, there exists $\beta > 0$ such that*

$$\sup_{\boldsymbol{\tau}_h \in \Sigma_h} \frac{(\mathbf{div}\, \boldsymbol{\tau}_h, \mathbf{v}_h)}{||\boldsymbol{\tau}_h||_\Sigma} \geq \beta ||\mathbf{v}_h||_U \qquad \forall\, \mathbf{v}_h \in U_h.$$

2.2.3 Error estimates

We denote with $\mathcal{P}_0(\mathcal{T}_h)$ the space of piecewise constant functions with respect to the given mesh $\mathcal{T}_h$. Using the techniques developed in [15], one can prove the following result.

Proposition 2.2.7. *Suppose that assumptions* (**B1**), (**B2**) *and* (**B3**) *are fulfilled. For every $(\boldsymbol{\sigma}_I, \mathbf{u}_I) \in \Sigma_h \times U_h$ and every $\boldsymbol{\sigma}_\pi \in [\mathcal{P}_0(\mathcal{T}_h)]^{3\times 3}_s$, the following error equation holds:*

$$||\boldsymbol{\sigma} - \boldsymbol{\sigma}_h||_\Sigma + ||\mathbf{u} - \mathbf{u}_h||_U \lesssim ||\boldsymbol{\sigma} - \boldsymbol{\sigma}_I||_\Sigma + ||\mathbf{u} - \mathbf{u}_I||_U + h\, ||\,\mathbf{div}\, \boldsymbol{\sigma}_I||_{0,\Omega} + ||\boldsymbol{\sigma} - \boldsymbol{\sigma}_\pi||_{0,\Omega}.$$

A suitable choice of $\mathbf{u}_I$, $\boldsymbol{\sigma}_I$, and $\boldsymbol{\sigma}_\pi$ leads to the following error estimate, see [15].

Theorem 2.2.8. *Let $(\boldsymbol{\sigma}, \mathbf{u}) \in \Sigma \times U$ be the solution of Problem (1.74), and let $(\boldsymbol{\sigma}_h, \mathbf{u}_h) \in \Sigma_h \times U_h$ be the solution of the discrete problem (2.29). Suppose that assumptions (**B1**), (**B2**) and (**B3**) are fulfilled. Assuming $\boldsymbol{\sigma}_{|E} \in [H^1(E)]^{3\times 3}$ and $(\mathbf{div}\ \boldsymbol{\sigma})_{|E} \in [H^1(E)]^3$, the following estimate holds true:*

$$||\boldsymbol{\sigma} - \boldsymbol{\sigma}_h||_\Sigma + ||\mathbf{u} - \mathbf{u}_h||_U \lesssim C(\Omega, \boldsymbol{\sigma}, \mathbf{u})\, h,$$

where $C(\Omega, \boldsymbol{\sigma}, \mathbf{u})$ is independent of h but depends on the domain Ω and on the Sobolev regularity of $\boldsymbol{\sigma}$ and $\mathbf{u}$.

2.3 Numerical results

In this section we numerically assess the proposed VEM approach by means of a selection of test problems where the analytical solution is available. Furthermore, we consider a more realistic, though simple, example.

2.3.1 Accuracy assessment on a cubic domain

We consider the standard unit cube $\Omega = [0, 1]^3$ as the domain of our problems and we take the following four types of mesh:

- `Cube`, a mesh composed by standard structured cubes;
- `Tetra`, a Delaunay tetrahedralization of the domain Ω;
- `CVT`, a Voronoi tassellation obtained by the Lloyd algorithm [60];
- `Rand`, a Voronoi tassellation achieved with random control points.

We remark that the meshes `CVT` and `Rand` are very challenging. Indeed, they could have some elements with small faces and edges, and we remark that such case is *not* covered by the developed theory, i.e., assumptions (**B1**), (**B2**) and (**B3**). However, the numerical results show that the proposed methods are fairly robust with respect to this geometric situation. These two types of meshes are build via the `voro++` library [77].

In order to assess the convergence rate, for each type of mesh, we define the following mesh-size h:

$$h := \frac{1}{N_E} \sum_{i=1}^{N_E} h_E$$

where we recall that N_E is the number of elements in the mesh, and h_E is the diameter of the polyhedron E. The accuracy and the convergence rate assessment is carried out using the following error norms:

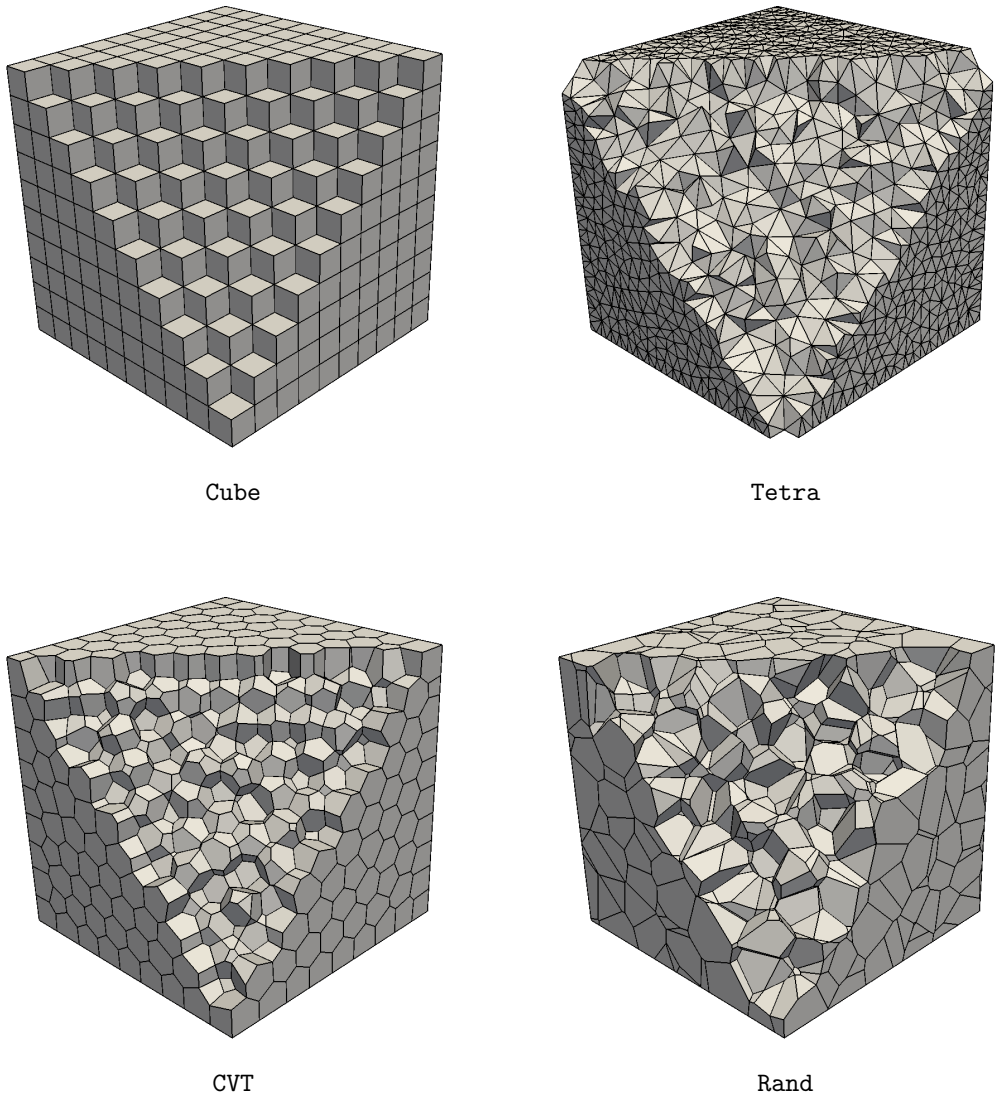

Figure 2.2: Overview of adopted meshes for convergence assessment numerical tests.

- L^2 error norm for the displacement field:

$$E_{\mathbf{u}} := \left(\sum_{E \in \mathcal{T}_h} \int_E |\mathbf{u} - \mathbf{u}_h|^2 \, \mathrm{d}E \right)^{1/2} = ||\mathbf{u} - \mathbf{u}_h||_0.$$

- L^2 error on the divergence:

$$E_{\boldsymbol{\sigma},\mathbf{div}} := \left(\sum_{E \in \mathcal{T}_h} \int_E |\,\mathbf{div}(\boldsymbol{\sigma} - \boldsymbol{\sigma}_h)|^2 \, \mathrm{d}E \right)^{1/2} = ||\,\mathbf{div}\,\boldsymbol{\sigma} - \mathbf{div}\,\boldsymbol{\sigma}_h||_0.$$

- L^2 error on the projection:

$$E_{\boldsymbol{\sigma},\Pi} := \left(\sum_{E \in \mathcal{T}_h} \int_E |\boldsymbol{\sigma} - \Pi_E \boldsymbol{\sigma}_h|^2 \, \mathrm{d}E \right)^{1/2} = ||\boldsymbol{\sigma} - \Pi_E \boldsymbol{\sigma}_h||_0.$$

- Discrete error norm for the stress field:

$$E_{\boldsymbol{\sigma}} := \left(\sum_{f \in \mathcal{F}_h} h_f \int_f \kappa \, |(\boldsymbol{\sigma} - \boldsymbol{\sigma}_h)\mathbf{n}|^2 \, \mathrm{d}f \right)^{1/2},$$

  where $\mathcal{F}_h$ is the set of faces for $\mathcal{T}_h$ and $\kappa = \frac{1}{2}\mathrm{tr}(\mathbb{D})$ (the material is here homogeneous). We remark that the quantity above scales like the internal elastic energy, with respect to the size of the domain and of the elastic coefficients, i.e., $\sim h$.

The above error quantities are computed by means of suitable quadrature rules based on sub-triangulation and sub-tetrahedralization methods.

Example 1 (compressible material and mixed BC). We consider an elastic problem where a trigonometric solution is a-priori selected. Accordingly, the applied loads are determined. Moreover, homogeneous Dirichlet boundary conditions are imposed on three faces of the cube ($x = 0$, $y = 0$, $z = 0$), as well as homogeneous Neumann boundary conditions on the remaining faces. The material is assumed to be homogeneous and isotropic. More precisely, the displacement solution and the loads are as follows:

$$\begin{cases} u_1 = u_2 = u_3 = 10\, S(x,y,z) \\ f_1 = -10\pi^2((\lambda+\mu)\cos(\pi x)\sin(\pi y + \pi z) - (\lambda + 4\mu)S(x,y,z)) \\ f_2 = -10\pi^2((\lambda+\mu)\cos(\pi y)\sin(\pi x + \pi z) - (\lambda + 4\mu)S(x,y,z)) \\ f_3 = -10\pi^2((\lambda+\mu)\cos(\pi z)\sin(\pi x + \pi y) - (\lambda + 4\mu)S(x,y,z)), \end{cases}$$

where $S(x,y,z) = \sin(\pi x)\sin(\pi y)\sin(\pi z)$. The Lamé constants are here set as $\lambda = 1$ and $\mu = 1$.

Figure 2.3 reports the h-convergence of the proposed method for Example 1. As expected, for the considered method, the asymptotic convergence rate is approximately equal to 1 for all error norms and meshes. The $E_{\mathbf{u}}$ plot seems to exhibit a different convergence rate with respect to the theoretical result, but this fact is essentially related to the nature of the problem and the mesh-size. Indeed, refining the meshes, one can observe that the convergence rate draws near to 1. In addition, the convergence graphs of each type of mesh are close to each other and this fact confirms the robustness of the proposed method with respect to the element shape.

Example 2 (nearly incompressible material). We again consider a problem with known analytical solution. A nearly incompressible material is chosen by selecting Lamé constants as $\lambda = 10^5$, $\mu = 0.5$. The test is designed by choosing a required solution for

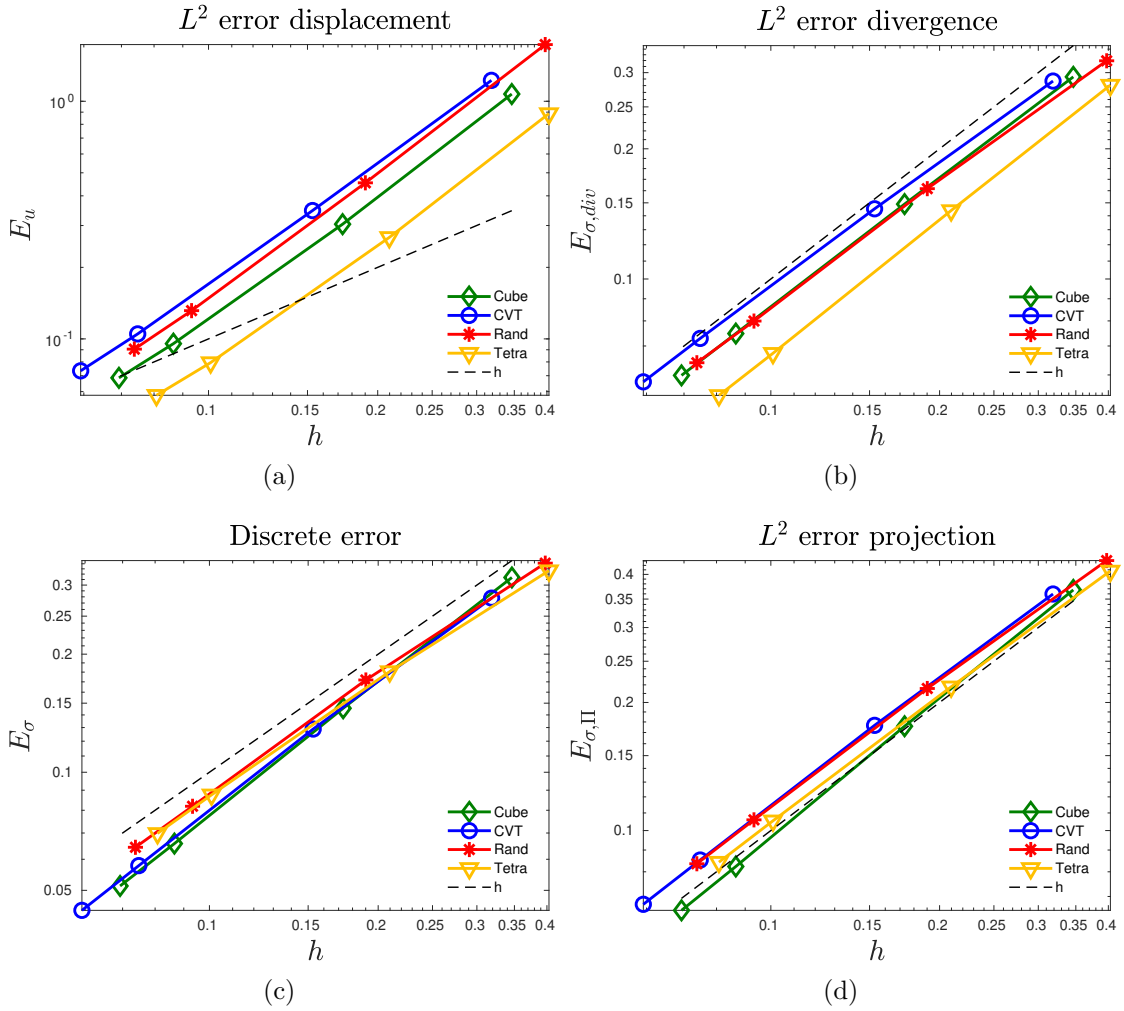

Figure 2.3: Example 1 (compressible material and mixed BCs). h-convergence results for all meshes.

the displacement field and deriving the load $\mathbf{f}$ accordingly. The displacement solution is as follows:

$$\begin{cases} u_1 = \sin(2\pi x)^2 \left(\cos(2\pi y)\sin(2\pi y)\sin(2\pi z)^2 - \cos(2\pi z)\sin(2\pi z)\sin(2\pi y)^2\right) \\ u_2 = \sin(2\pi y)^2 \left(\cos(2\pi z)\sin(2\pi z)\sin(2\pi x)^2 - \cos(2\pi x)\sin(2\pi x)\sin(2\pi z)^2\right) \\ u_3 = \sin(2\pi z)^2 \left(\cos(2\pi x)\sin(2\pi x)\sin(2\pi y)^2 - \cos(2\pi y)\sin(2\pi y)\sin(2\pi x)^2\right) \end{cases}$$

In Figure 2.4 we report the convergence results for the proposed VEM approach. It can be clearly seen that our method shows the expected asymptotic rate of convergence for each kind of mesh.The $E_{\mathbf{u}}$ plot seems to have a different convergence rate with respect to the theoretical result, but this fact is essentially related to the nature of the problem and the mesh-size. Hence, refining the meshes, one can observe that the convergence rate draws

near to 1. Moreover, also in this case the convergence lines are close to each other and this fact further confirms the robustness of the proposed scheme with respect to element shape.

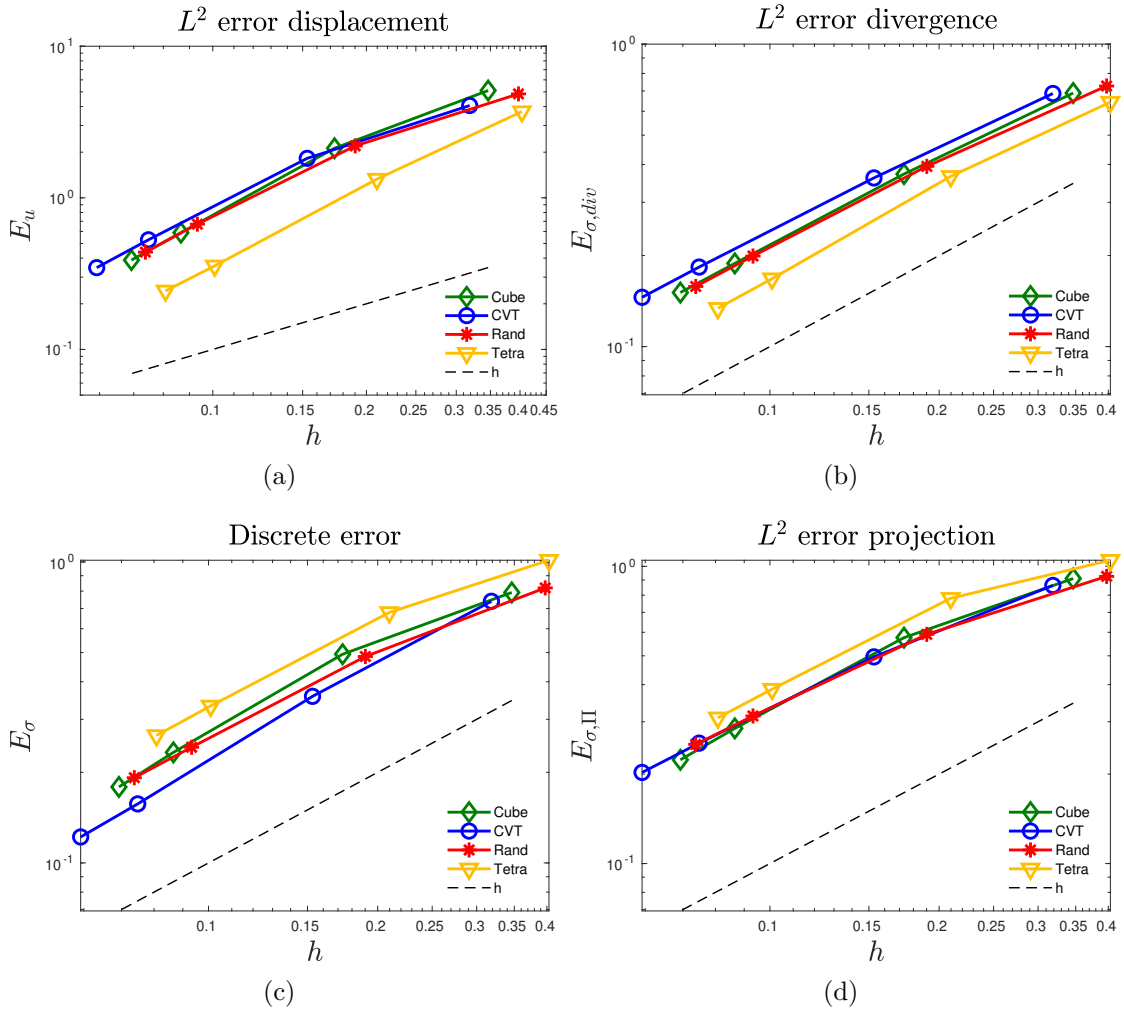

Figure 2.4: Example 2 (nearly incompressible material). h-convergence results for all meshes.

Example 3 (unloaded body). We consider a problem with polynomial solution, non-homogeneous Dirichlet boundary conditions and zero loading. We take a homogeneous and isotropic material with Lamé constants $\lambda = 1$ and $\mu = 1$ (compressible case). As in the previous examples, the test is defined by choosing a required solution and deriving the

correspondig body load $\mathbf{f} = \mathbf{0}$, as indicated in the following:

$$\begin{cases} u_1 = 2x^3 - 3xy^2 - 3xz^2 \\ u_2 = 2y^3 - 3yx^2 - 3yz^2 \\ u_3 = 2z^3 - 3zy^2 - 3zx^2 \\ \mathbf{f} = \mathbf{0} \end{cases}$$

We remark that this is a typical example where the displacement field is nontrivial, while stresses are divergence-free. As expected, this latter feature is numerically satisfied by the proposed VEM scheme. Indeed, in Table 2.1 the errors $E_{\boldsymbol{\sigma},\mathbf{div}}$ are close to the machine precision at each mesh refinement step. The other error behaviours are similar to the ones showed in the previous examples so we do not report such graphs.

Step	`Cube`	`Tetra`	`CVT`	`Rand`
1	2.1904e-14	4.7821e-14	2.2369e-14	2.9712e-14
2	4.7351e-14	1.2589e-13	4.5054e-14	6.4063e-14
3	1.0024e-13	2.0757e-13	8.7751e-14	1.3174e-13
4	1.1793e-13	2.7652e-13	1.0922e-13	1.6482e-13

Table 2.1: Example 3 (unloaded body). h-convergence results for error $E_{\boldsymbol{\sigma},\mathbf{div}}$.

2.3.2 L-shaped domain test

In this subsection, we consider a problem for which we do not know the analytical solution. First of all, we take the 3D L-shaped domain $\Omega = A \setminus B$, where $A = [0,2] \times [0,1] \times [0,2]$ while $B = (1,2] \times [0,1] \times (1,2]$. Then, we study the following problem: find $(\boldsymbol{\sigma}, \mathbf{u})$ such that

$$\begin{cases} -\mathbf{div}\,\boldsymbol{\sigma} = \mathbf{f} & \text{in } \Omega \\ \boldsymbol{\sigma} = \mathbb{C}\boldsymbol{\varepsilon}(\mathbf{u}) & \text{in } \Omega \\ \mathbf{u} = \mathbf{0} & \text{in } \partial\Omega_D \\ \boldsymbol{\sigma}\mathbf{n} = \mathbf{0} & \text{in } \partial\Omega_{N_0} \\ \boldsymbol{\sigma}\mathbf{n} = \boldsymbol{\psi} & \text{in } \partial\Omega_{N_1}, \end{cases}$$

where the boundary $\partial\Omega$ is divided into three regular disjoint parts:

$$\begin{aligned} \partial\Omega_D &= \{(x,y,z) \in \partial\Omega \ : \ z = 2\} \\ \partial\Omega_{N_1} &= \{(x,y,z) \in \partial\Omega \ : \ x = 2\} \\ \partial\Omega_{N_0} &= \partial\Omega \setminus (\partial\Omega_D \cup \partial\Omega_{N_1}). \end{aligned}$$

Furthermore, we take the loading term $\mathbf{f} = (0,0,-0.001)^T$ and boundary traction $\boldsymbol{\psi} = (0,0,0.-0.008)^T$. The material is homogeneous and isotropic with Lamé coefficients $\lambda = 1$ and $\mu = 1$ (compressible material). For this simulation we use a `Tetra` mesh.

In Figure 2.5 we report both the mesh of our domain, and the deformed body the force application. For a more significant visualization, we overlap the two images and we use the transparency to show the unloaded body. Finally, contours representing the von Mises equivalent stress distribution are reported in Figure 2.6. We remark that the discrete stress distribution $\boldsymbol{\sigma}_h$ is not known inside the polyhedrons, but its projection $\Pi_E \boldsymbol{\sigma}_h$ onto the constant tensors is computable. Thus, in Figure 2.6 we have used this latter quantity to approximate and display the von Mises equivalent stress. As already mentioned, the analytical solution to this problem is not available. Consequently, a quantitative evaluation of the method performance cannot be easily performed (one possible way is, of course, to take advantage of a reference discrete solution, computed on a very fine mesh). However, a qualitative inspection of Figure 2.6 shows that both the computed deformed shape, and the von Mises equivalent stress distribution are realistic.

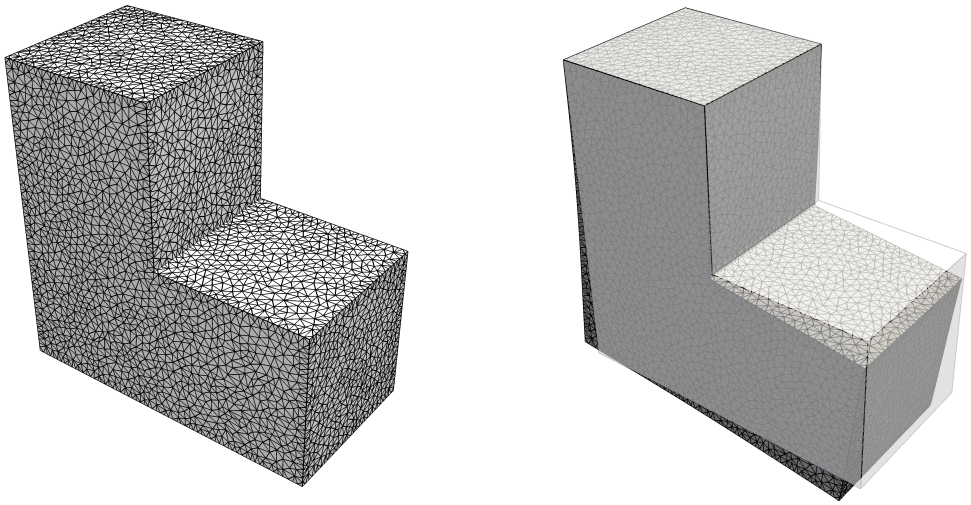

(a) (b)

Figure 2.5: L-shaped domain test. Contours representing the problem: (a) unloaded body and (b) deformed body.

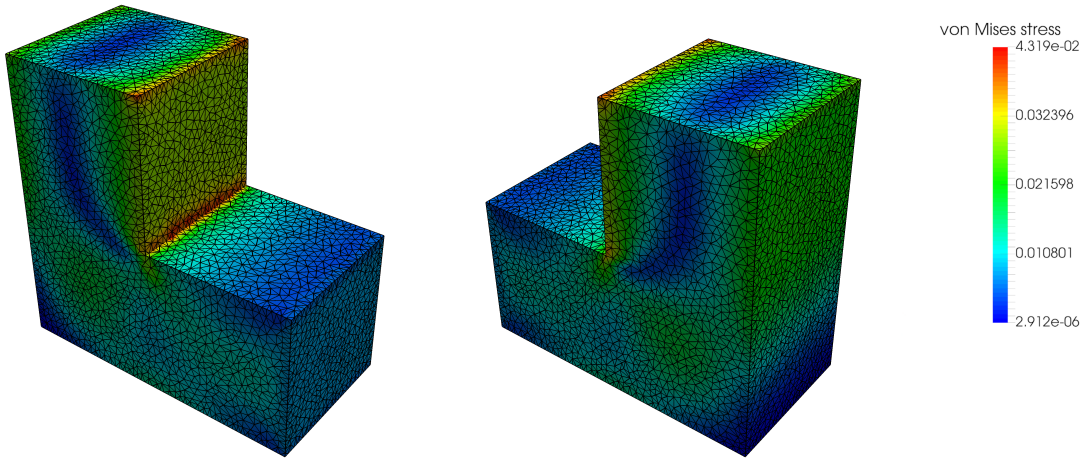

(a) (b)

Figure 2.6: L-shaped domain test. Contours representing the von Mises equivalent distribution: (a) front view and (b) rear view.

Chapter 3

Hybridization of a low-order Virtual Element Method

In Chapter 2, we introduced an interesting low-order Virtual Element Method for 3D linear elasticity problems. The main feature of this method is that the VEM concept is primarily applied to the stresses, while the displacement field is modeled with polynomail functions, in accordance with the classical Finite Element procedure. The reason of this choice is that we need more flexibility in order to simultaneously manage the $H(\mathbf{div})$-conformity and the symmetry of the stress. Another important property of the proposed scheme is that the tractions, which are the stress degrees of freedom, are not defined on the vertices of the mesh (as FEM), but they are entirely local to each polyhedron face. Therefore, there is the possibility to apply the hybridization procedure to our Virtual Element Method.

The hybridization technology was born in 1965 [57] as an implementation technique (for FEM) for solving the linear elasticity problems. The idea of this primordial procedure was to exploit the Lagrange multipliers to impose the continuity constraints on the inter-elements and to use the static condensation to lead to solving a linear system for a matrix that is symmetric and positive definite instead of the original indefinite one. In 1985 [7], the aim of this procedure changed a little bit. Besides, to produce computational advantages, the idea was to employ the extra information inferred from the Lagrange multipliers to produce a better approximation of the continuous displacement solution.

The aim of this chapter is to present the hybridization technique of a low-order VEM for Hellinger-Reissner elasticity problems showing both the computational and theoretical aspects. For simplicity, we will present the analysis of the method for a bi-dimensional problem.

The chapter is organized as follows. In Section 3.1, we introduce the computational aspects of the hybridization technique, in particular, we show the algorithm of static condensation. We devote Section 3.2 to the design of a virtual element method. Section 3.3 shows some interesting theoretical results, while in Section 3.4, we give possible post-processing, exploiting some information derived from the Lagrange multipliers. Finally, in Section 3.5 we provide some experiments to give numerical evidence of the proposed VEM approach for both two and three dimensional problems.

The results of this chapter can be found in [55].

3.1 Hybridization procedure

In this section, we present the hybridization technique for a mixed virtual element method designed on the elasticity problems (see Section 1.3). Here, in particular, we will describe the computational aspects of this technology, while we will postpone the issue of a possible post-processing in the Section 3.4.

First of all, we recall the typical discrete formulation of elasticity Problem (1.66) with non-homogeneous Dirichlet boundary conditions, see Section 2.1.3:

$$\begin{cases} \text{Find } (\boldsymbol{\sigma}_h, \mathbf{u}_h) \in \Sigma_h \times U_h \text{ such that} \\ a_h(\boldsymbol{\sigma}_h, \boldsymbol{\tau}_h) + (\mathbf{div}\, \boldsymbol{\tau}_h, \mathbf{u}_h) = \langle \mathbf{g}, \boldsymbol{\tau}_h\, \mathbf{n} \rangle \quad \forall \boldsymbol{\tau}_h \in \Sigma_h \\ (\mathbf{div}\, \boldsymbol{\sigma}_h, \mathbf{v}_h) = -(\mathbf{f}, \mathbf{v}_h) \qquad\qquad \forall \mathbf{v}_h \in U_h, \end{cases} \tag{3.1}$$

where Σ_h and U_h are the global discrete spaces for the stress and displacement field, respectively, while $a_h(\cdot,\cdot)$ is a suitable approximation of the corresponding bilinear form $a(\cdot,\cdot)$. More details about possible choices of the spaces for a conforming low-order VEM can be found in [15, 54]. The linear system associated with (3.1) has the following form

$$\begin{pmatrix} A & B \\ B^T & 0 \end{pmatrix} \begin{pmatrix} \boldsymbol{\sigma}_h \\ \mathbf{u}_h \end{pmatrix} = \begin{pmatrix} G \\ F \end{pmatrix} \tag{3.2}$$

whose matrix is indefinite. The hybridization procedure is an implementational technique for mixed method which leads to solve a linear system with a symmetric and positive definite instead of the original indefinite one (3.2). To carry it out, this procedure is split into two different steps: the imposition of the stress $H(\mathbf{div})$-conformity requirement through the introduction of suitable Lagrange multipliers, and the static condensation algorithm.

First step: introduction of Lagrange multipliers. We notice that the possibility to perform hybridization highly depends on the particular features of the discrete scheme, and it is not always possible. Therefore, to apply this step and this technology, we must not have nodal degrees of freedom for the stress field, as happens, for instance, for the method proposed in Chapter 2 or in [15]. Denoting by $\boldsymbol{\lambda}_h$ the Lagrange multipliers, the resulting linear system has the following form

$$\begin{pmatrix} \tilde{A} & \tilde{B} & \tilde{C} \\ \tilde{B}^T & O & O \\ \tilde{C}^T & O & O \end{pmatrix} \begin{pmatrix} \boldsymbol{\sigma}_h \\ \mathbf{u}_h \\ \boldsymbol{\lambda}_h \end{pmatrix} = \begin{pmatrix} \tilde{G} \\ \tilde{F} \\ O \end{pmatrix} \tag{3.3}$$

where the symbol $\sim$ here highlights that the quantity under consideration refers to the (discontinuous) stress space, rather then the conforming one. Moreover, we remark that the third equation

$$\tilde{C}^T \boldsymbol{\sigma}_h = O \tag{3.4}$$

represents the traction continuity for the stress field by means of the multipliers.

Immediately, we notice that, in this first phase, we have an increase in the dimension of our linear system: we add the Lagrange multipliers and we double the number of the stress degrees of freedom on the internal interfaces. Therefore, it is counter-productive to stop at this point, because we do not see any improvement in the hybridization technique, but on the contrary, we worsen the situation. So, the next step is fundamental.

Remark 12. *We observe that a reasonable choice of the space of multipliers leads to obtain the same discrete solution of the linear system (3.2), although the dimension of the stress vector is obviously different.*

Second step: static condensation algorithm. We observe that one of the advantages to having discontinuous stress degrees of freedom is that the matrices $\tilde{A}$ and $\tilde{B}$, corresponding to the discrete bilinear form $a_h(\cdot,\cdot)$ and the mixed term $(\mathbf{div}\,\cdot,\cdot)$ are block diagonal matrices. Each block corresponds to the information of a single element in our discretization. Hence, the matrix $\tilde{A}$ is a block diagonal matrix, whose inverse can be found in a fast and cheap way. Then we can compute $\boldsymbol{\sigma}_h$ via:

$$\boldsymbol{\sigma}_h = \tilde{A}^{-1}(\tilde{G} - \tilde{B}\mathbf{u}_h - \tilde{C}\boldsymbol{\lambda}_h). \tag{3.5}$$

Subtracting (3.5) into the second and third equations of (3.3) we have

$$\begin{pmatrix} \tilde{B}^T\tilde{A}^{-1}\tilde{B} & \tilde{B}^T\tilde{A}^{-1}\tilde{C} \\ \tilde{C}^T\tilde{A}^{-1}\tilde{B} & \tilde{C}^T\tilde{A}^{-1}\tilde{C} \end{pmatrix} \begin{pmatrix} \mathbf{u}_h \\ \boldsymbol{\lambda}_h \end{pmatrix} = \begin{pmatrix} \tilde{B}^T\tilde{A}^{-1}\tilde{G} - \tilde{F} \\ \tilde{C}^T\tilde{A}^{-1}\tilde{G} \end{pmatrix} \tag{3.6}$$

which is symmetric and positive definite.
Now, recalling again that $\tilde{A}$ and $\tilde{B}$ are block matrices, then we have that $\tilde{B}^T\tilde{A}^{-1}\tilde{B}$ is a block diagonal matrix, too. As before, it can be inverted in a straightforward way and we get

$$\mathbf{u}_h = (\tilde{B}^T\tilde{A}^{-1}\tilde{B})^{-1}\left[(\tilde{B}^T\tilde{A}^{-1}\tilde{C})\boldsymbol{\lambda}_h + \tilde{B}^T\tilde{A}^{-1}\tilde{G} - \tilde{F}\right]. \tag{3.7}$$

Now, substituting $\mathbf{u}_h$ in the third equation, our system has the following form

$$H\boldsymbol{\lambda}_h = R \tag{3.8}$$

where

$$H = (-\tilde{C}^T\tilde{A}^{-1}\tilde{B})(\tilde{B}^T\tilde{A}^{-1}\tilde{B})^{-1}(\tilde{B}^T\tilde{A}^{-1}\tilde{C}) - \tilde{C}^T\tilde{A}^{-1}\tilde{C} \tag{3.9}$$

and

$$R = -\tilde{C}^T\tilde{A}^{-1}\tilde{G} + (C^T\tilde{A}^{-1}\tilde{B})(\tilde{B}^T\tilde{A}^{-1}\tilde{B})^{-1}(\tilde{B}^T\tilde{A}^{-1}\tilde{G} - \tilde{F}). \tag{3.10}$$

The matrix H is symmetric and positive definite. This is an advantage from a computational viewpoint. Indeed, one can use an "ad-hoc" procedure to solve (3.8), for instance Cholesky decomposition. Once we have $\boldsymbol{\lambda}_h$, the displacement and then the stress vectors can be obtained explicitly via matrix-vector multiplication, see (3.7) and (3.5).

Remark 13. *The Lagrange multiplier field has the physical interpretation of (generalized) displacements. As we will see in Section 3.4, we will employ it to design a higher-order (non-conforming) approximation of the displacement field.*

3.2 The Virtual Element Method

Following the steps of Section 2.1, we present the virtual element approximation stemming from the hybridization procedure. Let $\{\mathcal{T}_h\}_h$ be a sequence decomposition of Ω into general polygons E satisfying the assumption (**A1**) and (**A2**) listed in Section 1.1.3. For simplicity, we assume that the material tensor $\mathbb{D}$ is piecewise constant with respect to the decomposition $\mathcal{T}_h$, see Chapter 2.

3.2.1 The discrete spaces

To describe the local spaces employed in our VE scheme, we first need to introduce these two "elementary" spaces: $RM(E)$ and $R(e)$, which are the bi-dimensional counterparts of $RM(E)$ and $T_h(f)$, see Section 2.1.1.

Space $RM(E)$. It is the space of local infinitesimal rigid body motions:

$$RM(E) := \left\{ \mathbf{r}(\mathbf{x}) = \boldsymbol{\alpha} + \beta\big(\mathbf{x} - \mathbf{x}_E\big)^{\perp} \quad \text{s.t.} \quad \boldsymbol{\alpha} \in \mathbb{R}^2 \text{ and } \beta \in \mathbb{R} \right\}, \tag{3.11}$$

where if $\mathbf{c} = (c_1, c_2)^T$ is a generic vector in $\mathbb{R}^2$, we denote by $\mathbf{c}^{\perp} = (c_2, -c_1)^T$ its counter-clockwise rotation. The dimension of $RM(E)$ is 3.

Space $R(e)$. For each edge $e \in \partial E$, we introduce

$$R(e) = \{\boldsymbol{\psi}(s) = c\,\mathbf{t}_e + p_1(s)\,\mathbf{n}_e \quad c \in \mathbb{R}, \quad p_1(s) \in \mathcal{P}_1(e)\} \tag{3.12}$$

where $\mathbf{n}_e$ is the outward normal to the edge e, and $\mathbf{t}_e$ is the tangent vector to the edge e, in accordance with its direction. The dimension of such space is 3, indeed:

- the tangential component is determined by a single scalar value $c \in \mathbb{R}$;
- the polynomial $p_1(s) \in \mathcal{P}_1(e)$ is one variable polynomial with respect to the local edge coordinate system so it is determined by two parameters, as illustrated here below:

$$p_1(s) := d_1 + d_2(s - s_e). \tag{3.13}$$

Therefore, this space consists of vector functions whose tangential component is constant (first term of (3.12)), while the normal component is a linear (one-variable) polynomial (the last term of (3.12)).

Stress space. Starting from $RM(E)$ and $R(e)$ we can define our local approximation space for the stress field:

$$\begin{aligned} \Sigma_h(E) = \Big\{ \boldsymbol{\tau}_h \in & H(\mathbf{div}; E) \ : \ \exists \mathbf{w}^* \in \Big[H^1(E)\Big]^2 \text{ such that } \boldsymbol{\tau}_h = \mathbb{C}\boldsymbol{\varepsilon}(\mathbf{w}^*); \\ & (\boldsymbol{\tau}_h\,\mathbf{n})_{|e} \in R(e) \quad \forall e \in \partial E; \quad \mathbf{div}\,\boldsymbol{\tau}_h \in RM(E) \Big\}. \end{aligned} \tag{3.14}$$

Accordingly, every local virtual function $\boldsymbol{\sigma}_h \in \Sigma_h(E)$ is uniquely determined by the following degrees of freedom, see also (3.12).

- For each edge e of the element E, the degree of freedom which determines the tangential component of the tractions:

$$\boldsymbol{\tau}_h \to \int_e (\boldsymbol{\tau}_h \, \mathbf{n})_{|e} \cdot \mathbf{t}_e \ \mathrm{d}s. \tag{3.15}$$

- For each edge e of the element E, the two degrees of freedom which determine the normal component of the tractions:

$$\tau_h \to \int_e (\boldsymbol{\tau}_h \, \mathbf{n})_{|e} \cdot p_1(s) \, \mathbf{n}_e \ \mathrm{d}s \qquad \forall p_1(s) \in \mathcal{P}_1(e). \tag{3.16}$$

Firstly, we notice that $\mathbf{div}\, \boldsymbol{\tau}_h \in RM(E)$ is completely determined by

$$(\boldsymbol{\tau}_h \, \mathbf{n})_{|e} := c_e \, \mathbf{t}_e + p_{1,e}(s) \, \mathbf{n}_e,$$

where e is an edge of E. Indeed, denoting $\boldsymbol{\varphi} : \partial E \to \mathbb{R}^2$ such that $\boldsymbol{\varphi}_{|e} = c_e \, \mathbf{t}_e + p_{1,e}(s) \, \mathbf{n}_e$, the obvious compatibility condition

$$\int_E \mathbf{div}\, \boldsymbol{\tau}_h \cdot \mathbf{r} \ \mathrm{d}E = \int_{\partial E} \boldsymbol{\varphi} \cdot \mathbf{r} \ \mathrm{d}s \qquad \forall \mathbf{r} \in RM(E), \tag{3.17}$$

allows to compute $\mathbf{div}\, \boldsymbol{\tau}_h$ using the information on the boundary. More precisely, setting (cf (3.11))

$$\mathbf{div}\, \boldsymbol{\tau}_h = \boldsymbol{\alpha}_E + \beta_E (\mathbf{x} - \mathbf{x}_C)^{\perp}, \tag{3.18}$$

from (3.17) we infer that the vector $\boldsymbol{\alpha}_E$ can be computed as follows (cf. (3.13))

$$\boldsymbol{\alpha}_E = \frac{1}{|E|} \int_{\partial E} \boldsymbol{\varphi} \ \mathrm{d}s = \frac{1}{|E|} \sum_{e \in \partial E} \int_e (c_e \, \mathbf{t}_e + d_{1,e} \, \mathbf{n}_e) \ \mathrm{d}s, \tag{3.19}$$

while the coefficient β_E, in front of the rotational term, is given by

$$\begin{aligned} \beta_E &= \frac{1}{\int_E |\mathbf{x} - \mathbf{x}_E|^2 \, dE} \int_{\partial E} \boldsymbol{\varphi} \cdot (\mathbf{x} - \mathbf{x}_E)^{\perp} \ \mathrm{d}s \\ &= \frac{1}{\int_E |\mathbf{x} - \mathbf{x}_E|^2 \, dE} \sum_{e \in \partial E} \int_e (c_e \mathbf{t}_e + p_{1,e}(s) \, \mathbf{n}_e) \cdot (\mathbf{x} - \mathbf{x}_E)^{\perp} \ \mathrm{d}s. \end{aligned} \tag{3.20}$$

Therefore, see Figure 3.1, we infer that the dimension of this space is

$$\dim(\Sigma_h(E)) := \nu_E = 3n_e^E.$$

Since, in the hybridization procedure, no inter-element continuity is required, we define the global space as follows

$$\tilde{\Sigma}_h(\mathcal{T}_h) = \left\{ \boldsymbol{\tau}_h \in \left[L^2(\Omega) \right]^{2\times 2} \ : \ \boldsymbol{\tau}_{h_{|E}} \in \Sigma_h(E) \quad \forall E \in \mathcal{T}_h \right\}. \tag{3.21}$$

The dimension of $\tilde{\Sigma}_h(\mathcal{T}_h)$ is thus given by

$$\dim(\tilde{\Sigma}_h(\mathcal{T}_h)) = \nu_E \, N_E,$$

where we recall that N_E is the number of polygons in $\mathcal{T}_h$.

Remark 14. *We observe that the local approximation space for the stress field is the same as the conforming low-order VEM [15]. The crucial point lies in the definition of global stress space. Indeed, we have that the conforming approximation space is characterized as follows:*

$$\Sigma_h := \tilde{\Sigma}_h(\mathcal{T}_h) \cap H(\mathbf{div}, \Omega). \tag{3.22}$$

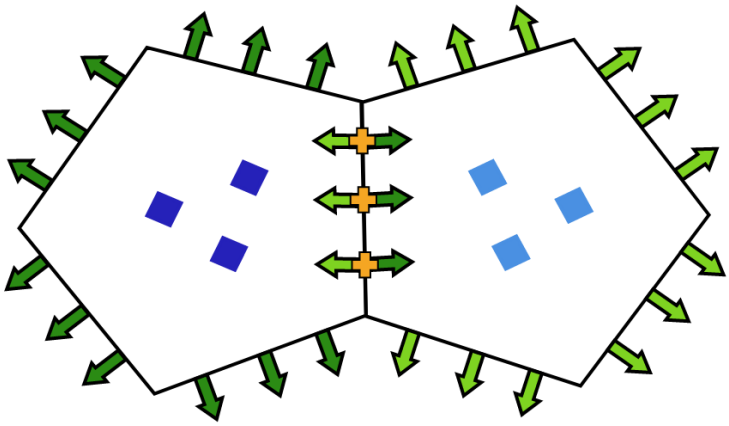

Figure 3.1: Overview of the degrees of freedom. The degrees of freedom are denoted as follows: square for displacement, arrow for stress and cross for Lagrange multiplier. Dark colors are referred to the left element, while light ones to the right.

Displacement space. The local approximation space for the displacement field is defined by, see (3.11)

$$U_h(E) = \left\{ \mathbf{v}_h \in \left[L^2(E)\right]^2 \ : \ \mathbf{v}_h \in RM(E) \right\}. \tag{3.23}$$

Accordingly, for the local space $U_h(E)$ the following degrees of freedom can be taken:

$$\mathbf{v}_h \to \int_E \mathbf{v}_h \cdot \mathbf{r} \, \mathrm{d}E \qquad \forall \mathbf{r} \in RM(E) \tag{3.24}$$

and it follows, see Figure 3.1, that

$$\dim(U_h(E)) = 3.$$

The global space is defined by gluing together all local spaces which is thus set as

$$U_h = \left\{ \mathbf{v}_h \in \left[L^2(\Omega)\right]^2 \ : \ \mathbf{v}_{h_{|E}} \in U_h(E), \quad \forall E \in \mathcal{T}_h \right\}. \tag{3.25}$$

The dimension of this space is

$$\dim(U_h) = 3\, N_E.$$

Lagrange multiplier space. Given $\mathcal{E}_h^I$, the set of the internal edges of $\mathcal{T}_h$, we define the space of the Lagrange multipliers by (cf. (3.12)):

$$\Lambda_h(\mathcal{E}_h^I) := \left\{ \boldsymbol{\mu}_h \in \left[L^2(\mathcal{E}_h^I)\right]^2 : \ \boldsymbol{\mu}_{h|e} \in R(e) \quad \forall\, e \in \mathcal{E}_h^I \right\}, \tag{3.26}$$

where, with a little abuse of notation, we denote with $L^2(\mathcal{E}_h^I)$ the L^2 space defined on the interior skeleton of $\mathcal{T}_h$, i.e., the union of $e \in \mathcal{E}_h^I$. We observe that the Lagrange multipliers are defined only on the internal edges $\mathcal{E}_h^I$ because their role will be to match the normal stresses insisting on interior interfaces, see Figure 3.1. Indeed a tensor field $\boldsymbol{\tau}$ is $H(\mathbf{div})$-regular if its normal component $\boldsymbol{\tau}\,\mathbf{n}$ does not jump across any interface inside Ω. To force such a continuity we consider the bilinear form

$$c_h(\cdot,\cdot) : \tilde{\Sigma}_h(\mathcal{T}_h) \times \Lambda_h(\mathcal{E}_h^I) \to \mathbb{R} \tag{3.27}$$

defined as:

$$c_h(\boldsymbol{\tau}_h, \boldsymbol{\mu}_h) := -\sum_{E \in \mathcal{T}_h} \int_{\partial E^I} \boldsymbol{\mu}_h \cdot \boldsymbol{\tau}_h\, \mathbf{n} \ \mathrm{d}s \qquad \forall \boldsymbol{\tau}_h \in \tilde{\Sigma}_h(\mathcal{T}_h),\ \forall \boldsymbol{\mu}_h \in \Lambda_h(\mathcal{E}_h^I), \tag{3.28}$$

where $\partial E^I = \partial E \cap \mathcal{E}_h^I$.

Moreover, using the same steps detailed in [39] for the proof, we have the following Lemma, which guarantees the good choice of the space of multipliers.

Lemma 3.2.1. *If $\boldsymbol{\tau}_h \in \tilde{\Sigma}_h(\mathcal{T}_h)$, then $\boldsymbol{\tau}_h \in \Sigma_h$ iff*

$$c_h(\boldsymbol{\mu}_h, \boldsymbol{\tau}_h) = 0 \qquad \forall \boldsymbol{\mu}_h \in \Lambda_h(\mathcal{E}_h^I). \tag{3.29}$$

3.2.2 The local forms

The local mixed and loading terms are designed accordingly with the description of Section 2.1.2, so we report the following terms.

The local bilinear form $a_E(\cdot,\cdot)$. As usual, in the VEM procedure, see Section 1.2, the local bilinear for

$$a_E(\boldsymbol{\sigma}_h, \boldsymbol{\tau}_h) = \int_E \mathbb{D}\boldsymbol{\sigma}_h : \boldsymbol{\tau}_h \ \mathrm{d}E \tag{3.30}$$

is not computable for a general couple $(\boldsymbol{\sigma}_h, \boldsymbol{\tau}_h) \in \Sigma_h(E) \times \Sigma_h(E)$. So, we need to define a suitable projection operator onto the local polynomial functions. We introduce

$$\Pi_E : \Sigma_h(E) \to [\mathcal{P}_0(E)]_s^{2\times 2}$$

as follows

$$a_E(\Pi_E \boldsymbol{\tau}_h, \boldsymbol{\pi}_0) = a_E(\boldsymbol{\tau}_h, \boldsymbol{\pi}_0) \quad \forall \boldsymbol{\pi}_0 \in [\mathcal{P}_0(E)]_s^{2\times 2}. \tag{3.31}$$

Therefore, Π_E is a projection operator onto the constant symmetric tensor functions and it is computable from the degrees of freedom. Indeed, using the divergence theorem and the fact that each $\boldsymbol{\pi}_0 \in [\mathcal{P}_0(E)]_s^{2\times 2}$ can be written as $\boldsymbol{\pi}_0 = \mathbb{C}\boldsymbol{\varepsilon}(\mathbf{p}_1)$, with $\mathbf{p}_1 \in [\mathcal{P}_1(E)]^2$, we rewrite the right-hand side of (3.31) as

$$\begin{aligned} a_E(\boldsymbol{\tau}_h, \boldsymbol{\pi}_0) &= \int_E \mathbb{D}\boldsymbol{\tau}_h : \boldsymbol{\pi}_0 \, \mathrm{d}E \\ &= \int_E \mathbb{D}\boldsymbol{\tau}_h : \mathbb{C}\boldsymbol{\varepsilon}(\mathbf{p}_1) \, \mathrm{d}E = \int_E \boldsymbol{\tau}_h : \boldsymbol{\varepsilon}(\mathbf{p}_1) \, \mathrm{d}E \\ &= -\int_E \mathbf{div}\, \boldsymbol{\tau}_h \cdot \mathbf{p}_1 \, \mathrm{d}E + \int_{\partial E} (\boldsymbol{\tau}_h \, \mathbf{n}) \cdot \mathbf{p}_1 \, \mathrm{d}s \end{aligned} \tag{3.32}$$

which is clearly computable from the knowledge of the degrees of freedom. Then, the approximation of $a_E(\cdot,\cdot)$ reads:

$$\begin{aligned} a_E^h(\boldsymbol{\sigma}_h, \boldsymbol{\tau}_h) &:= a_E(\Pi_E \, \boldsymbol{\sigma}_h, \Pi_E \boldsymbol{\tau}_h) + s_E\left((I - \Pi_E)\boldsymbol{\sigma}_h, (I - \Pi_E)\boldsymbol{\tau}_h\right) \\ &= \int_E \mathbb{D}(\Pi_E \boldsymbol{\sigma}_h) : (\Pi_E \boldsymbol{\tau}_h) \, \mathrm{d}E + s_E\left((I - \Pi_E)\boldsymbol{\sigma}_h, (I - \Pi_E)\boldsymbol{\tau}_h\right), \end{aligned} \tag{3.33}$$

where $s_E(\cdot,\cdot)$ is a suitable stabilization term. We propose the following choice:

$$s_E(\boldsymbol{\sigma}_h, \boldsymbol{\tau}_h) := \kappa_E \, h_E \int_{\partial E} \boldsymbol{\sigma}_h \mathbf{n} \cdot \boldsymbol{\tau}_h \mathbf{n} \, \mathrm{d}s. \tag{3.34}$$

Above, κ_E is a positive constant to be chosen according to $\mathbb{D}$. For instance, in the numerical examples of Section 3.5, κ_E is set equal to $\frac{1}{2}\mathrm{tr}(\mathbb{D}_{|E})$.

The continuity condition. Given an element $E \in \mathcal{T}_h$ and an edge $e \in \partial E \cap \mathcal{E}_h^I$ we have that for every $\boldsymbol{\tau}_h \in \Sigma_h(E)$ and $\boldsymbol{\mu}_h \in \Lambda_h(\mathcal{E}_h^I)$ the term

$$\int_e \boldsymbol{\mu}_h \cdot \boldsymbol{\tau}_h \, \mathbf{n} \, \mathrm{d}s \tag{3.35}$$

is computable thanks to the degrees of freedom and the Lagrange multipliers. Therefore, there is not need to introduce any approximation of the global term $c_h(\boldsymbol{\mu}_h, \boldsymbol{\tau}_h)$.

The boundary term. For a sufficiently regular function $\mathbf{g}$, this term can be split on each edge $e \in \mathcal{E}_h^B$ as follows

$$\langle \mathbf{g}, \boldsymbol{\tau}_h \, \mathbf{n} \rangle = \int_{\partial\Omega} \mathbf{g} \cdot \boldsymbol{\tau}_h \, \mathbf{n} \, \mathrm{d}s = \sum_{e \in \mathcal{E}_h^B} \int_e \mathbf{g} \cdot \boldsymbol{\tau}_h \, \mathbf{n}_e \, \mathrm{d}s. \tag{3.36}$$

Since $\boldsymbol{\tau}_h \in \Sigma_h(E)$ and in particular $\boldsymbol{\tau}_h \, \mathbf{n}_e$ is a polynomial function, this term is computable.

3.2.3 The discrete scheme

We present the hybrid discrete scheme which is represented at matrix level by (3.3) as follows:

$$\begin{cases} \text{Find } (\boldsymbol{\sigma}_h, \mathbf{u}_h, \boldsymbol{\lambda}_h) \in \tilde{\Sigma}_h(\mathcal{T}_h) \times U_h \times \Lambda_h(\mathcal{E}_h^I) \text{ such that} & \\ a_h(\boldsymbol{\sigma}_h, \boldsymbol{\tau}_h) + (\mathbf{div}\, \boldsymbol{\tau}_h, \mathbf{u}_h) + c_h(\boldsymbol{\lambda}_h, \boldsymbol{\tau}_h) =< \mathbf{g}, \boldsymbol{\tau}_h\, \mathbf{n} > & \forall \boldsymbol{\tau}_h \in \tilde{\Sigma}_h(\mathcal{T}_h), \\ (\mathbf{div}\, \boldsymbol{\sigma}_h, \mathbf{v}_h) = -(\mathbf{f}, \mathbf{v}_h) & \forall \mathbf{v} \in U_h, \\ c_h(\boldsymbol{\mu}_h, \boldsymbol{\sigma}_h) = 0 & \forall \boldsymbol{\mu}_h \in \Lambda_h(\mathcal{E}_h^I). \end{cases} \tag{3.37}$$

It is easy to prove that the two discrete Problems (3.1) and (3.37) are equivalent. In this particular case, equilavence means that if $(\boldsymbol{\sigma}_h, \mathbf{u}_h, \boldsymbol{\lambda}_h) \in \tilde{\Sigma}_h(\mathcal{T}_h) \times U_h \times \Lambda_h(\mathcal{E}_h^I)$ solves Problem (3.37), then $(\boldsymbol{\sigma}_h, \mathbf{u}_h) \in \Sigma_h \times U_h$ and is the solution of Problem (3.1). Moreover if $(\boldsymbol{\sigma}_h, \mathbf{u}_h) \in \Sigma_h \times U_h$ is the solution of Problem (3.1), then there is a unique $\boldsymbol{\lambda}_h \in \Lambda_h(\mathcal{E}_h^I)$ such that $(\boldsymbol{\sigma}_h, \mathbf{u}_h, \boldsymbol{\lambda}_h)$ is the solution of Problem (3.37).

3.3 Error analysis

Since the hybridization technique of Section 3.1 can be seen as a computational way to solve the original linear system stemming from the discrete Problem (3.1) (cf. (3.2)), the error estimates developed in [15] hold also for the stress and displacement solutions of the equivalent problem (3.37). In particular, the following result holds true.

Theorem 3.3.1. *Let $(\boldsymbol{\sigma}, \mathbf{u}) \in \Sigma \times U$ be the solution of Problem (1.73), and let $(\boldsymbol{\sigma}_h, \mathbf{u}_h) \in \tilde{\Sigma}_h(\mathcal{T}_h) \times U_h$ be the discrete stress and displacement solution of Problem (3.37). Under assumptions* **(A1)** *and* **(A2)** *on the mesh, and supposing $(\boldsymbol{\sigma}, \mathbf{u})$ sufficiently regular, the following estimate holds true:*

$$||\boldsymbol{\sigma} - \boldsymbol{\sigma}_h||_\Sigma + ||\mathbf{u} - \mathbf{u}_h||_U \lesssim h. \tag{3.38}$$

It remains to study the convergence to $\mathbf{u}$ of the Lagrange multipliers $\boldsymbol{\lambda}_h$ (we recall that the multipliers are physically a displacement field). It is useful to recall, see [15], that there exist an interpolation operator

$$\mathcal{I}_h : W^r(\Omega) \to \Sigma_h$$

where

$$W^r(\Omega) := \left\{ \boldsymbol{\tau} \ : \ \boldsymbol{\tau} \in [L^r(\Omega)]_s^{2\times 2} \quad \text{s.t.} \quad \mathbf{div}\, \boldsymbol{\tau} \in \left[L^2(\Omega)\right]^2 \right\}. \tag{3.39}$$

Such an operator is obtained by glueing the local contributions. We define the local interpolator $\mathcal{I}_E : W^r(E) \to \Sigma_h(E)$ as

$$\int_{\partial E} (\mathcal{I}_E\, \boldsymbol{\tau}) \mathbf{n} \cdot \boldsymbol{\varphi}_* \ \mathrm{d}s = \int_{\partial E} \boldsymbol{\tau}\, \mathbf{n} \cdot \boldsymbol{\varphi}_* \ \mathrm{d}s \quad \forall \boldsymbol{\varphi}_h \in R_*(\partial E), \tag{3.40}$$

where

$$R_*(\partial E) := \left\{ \boldsymbol{\varphi}_* \in \left[L^2(\partial E)\right]^2 \,:\, (\boldsymbol{\varphi}_*)_{|e} = \boldsymbol{\gamma}_e + \delta_e(\mathbf{x} - \mathbf{x}_E)^\perp \;\; \boldsymbol{\gamma}_e \in \mathbb{R}^2, \delta_e \in \mathbb{R}, \, \forall e \in \partial E \right\}.$$

The operator $\mathcal{I}_h$ satisfies the following commuting diagram property:

$$\mathbf{div}(\mathcal{I}_h \boldsymbol{\tau}) = \Pi_{RM}(\mathbf{div}\, \boldsymbol{\tau}) \quad \forall \boldsymbol{\tau} \in W^r(\Omega), \tag{3.41}$$

where Π_{RM} denotes the L^2-projection onto the space of the rigid body motions. Furthermore, the following error estimates hold true.

Proposition 3.3.2. *Under the standard mesh assumptions* (**A1**) *and* (**A2**)*, for the interpolation operator $\mathcal{I}_E$ defined in* (3.40) *and for each $\boldsymbol{\tau}$ sufficiently regular we have*

$$\begin{cases} ||\boldsymbol{\tau} - \mathcal{I}_E \boldsymbol{\tau}||_{0,E} \lesssim h_E |\boldsymbol{\tau}|_{1,E} \\ ||\,\mathbf{div}(\boldsymbol{\tau} - \mathcal{I}_E \boldsymbol{\tau})||_{0,E} \lesssim h_E |\,\mathbf{div}\, \boldsymbol{\tau}|_{1,E}. \end{cases} \tag{3.42}$$

3.3.1 A superconvergence result

Henceforth, we will suppose Ω to be a convex polyogn (or a domain sufficiently regular for the application of the shift theorem); moreover, in Problem (1.66) we consider homogeneous Dirichlet boundary conditions, i.e., $\mathbf{g} = \mathbf{0}$. Our aim is to prove that the L^2-projection of $\mathbf{u}$ onto the rigid body motion,

$$\bar{\mathbf{u}}_h = \Pi_{RM} \mathbf{u}, \tag{3.43}$$

superconverges to $\mathbf{u}$.

Theorem 3.3.3. *Let $(\boldsymbol{\sigma}, \mathbf{u}) \in \Sigma \times U$ be the solution of Problem* (1.66) *and let $(\boldsymbol{\sigma}_h, \mathbf{u}_h) \in \Sigma_h \times U_h$ be the solution of the discrete Problem* (3.1)*. Then, assuming the solution is sufficiently regular and considering the standard mesh assumptions* (**A1**) *and* (**A2**)*, the following estimate holds true:*

$$||\bar{\mathbf{u}}_h - \mathbf{u}_h||_0 \lesssim h^2. \tag{3.44}$$

Proof. Let $\boldsymbol{\varphi} \in [H^2(\Omega)]^2 \cap [H_0^1(\Omega)]^2$ be the solution of the linear elasticity problem:

$$\begin{cases} \mathbf{div}(\mathbb{C}\boldsymbol{\varepsilon}(\boldsymbol{\varphi})) = \bar{\mathbf{u}}_h - \mathbf{u}_h & \text{in } \Omega \\ \boldsymbol{\varphi} = \mathbf{0} & \text{on } \partial\Omega. \end{cases} \tag{3.45}$$

Due to standard regularity results (Ω is supposed to be convex), we have

$$||\boldsymbol{\varphi}||_2 \leq C ||\bar{\mathbf{u}}_h - \mathbf{u}_h||_0. \tag{3.46}$$

Set $\boldsymbol{\xi} = \mathbb{C}\boldsymbol{\varepsilon}(\boldsymbol{\varphi})$, let $\mathcal{I}_h \boldsymbol{\xi}$ be the interpolation of $\boldsymbol{\xi}$ defined in (3.40). Using (3.41), (3.45) and recalling that that $(\bar{\mathbf{u}}_h - \mathbf{u}_h)_{|E} \in RM(E)$, we get

$$\mathbf{div}(\mathcal{I}_h \boldsymbol{\xi}) := \Pi_{RM}\, (\mathbf{div}\, \boldsymbol{\xi}) = \Pi_{RM}\, (\bar{\mathbf{u}}_h - \mathbf{u}_h) = \bar{\mathbf{u}}_h - \mathbf{u}_h. \tag{3.47}$$

Therefore, using the definition of $\bar{\mathbf{u}}_h$, we have

$$\begin{aligned} ||\bar{\mathbf{u}}_h - \mathbf{u}_h||_0^2 &= \int_\Omega (\bar{\mathbf{u}}_h - \mathbf{u}_h) \cdot (\bar{\mathbf{u}}_h - \mathbf{u}_h) \ \mathrm{d}\Omega \\ &= \int_\Omega \mathbf{div}(\mathcal{I}_h \boldsymbol{\xi}) \cdot (\bar{\mathbf{u}}_h - \mathbf{u}_h) \ \mathrm{d}\Omega \\ &= \int_\Omega \mathbf{div}(\mathcal{I}_h \boldsymbol{\xi}) \cdot (\mathbf{u} - \mathbf{u}_h) \ \mathrm{d}\Omega. \end{aligned} \tag{3.48}$$

From (1.74), (3.1) and (3.48) we infer

$$||\bar{\mathbf{u}}_h - \mathbf{u}_h||_0^2 = \int_\Omega \mathbf{div}(\mathcal{I}_h \boldsymbol{\xi}) \cdot (\mathbf{u} - \mathbf{u}_h) \ \mathrm{d}\Omega = a_h(\boldsymbol{\sigma}_h, \mathcal{I}_h\boldsymbol{\xi}) - a(\boldsymbol{\sigma}, \mathcal{I}_h\boldsymbol{\xi}). \tag{3.49}$$

Now, employing the definition of the projection operator Π_E (cf. (3.31)), we get

$$\begin{aligned} &a_h(\boldsymbol{\sigma}_h, \mathcal{I}_h\boldsymbol{\xi}) - a(\boldsymbol{\sigma}, \mathcal{I}_h\boldsymbol{\xi}) \\ &= \sum_{E\in\mathcal{T}_h} \left[a_E^h(\boldsymbol{\sigma}_h, \mathcal{I}_E\boldsymbol{\xi}) - a_E(\boldsymbol{\sigma}, \mathcal{I}_E\boldsymbol{\xi})\right] \\ &= \sum_{E\in\mathcal{T}_h} \left[a_E(\Pi_E\boldsymbol{\sigma}_h, \Pi_E(\mathcal{I}_E\boldsymbol{\xi})) - a_E(\boldsymbol{\sigma}, \mathcal{I}_E\boldsymbol{\xi}) + s_E\left((I-\Pi_E)\boldsymbol{\sigma}_h, (I-\Pi_E)\mathcal{I}_E\boldsymbol{\xi}\right)\right] \\ &= \sum_{E\in\mathcal{T}_h} \left[a_E\left(\Pi_E\boldsymbol{\sigma}_h, \mathcal{I}_E\boldsymbol{\xi}\right) - a_E(\boldsymbol{\sigma}, \mathcal{I}_E\boldsymbol{\xi}) + s_E\left((I-\Pi_E)\boldsymbol{\sigma}_h, (I-\Pi_E)\mathcal{I}_E\boldsymbol{\xi}\right)\right] \\ &= \sum_{E\in\mathcal{T}_h} \left[a_E\left((\Pi_E - I)\boldsymbol{\sigma}_h, \mathcal{I}_E\boldsymbol{\xi}\right) + a_E(\boldsymbol{\sigma}_h - \boldsymbol{\sigma}, \mathcal{I}_E\boldsymbol{\xi}) + s_E\left((I-\Pi_E)\boldsymbol{\sigma}_h, (I-\Pi_E)\mathcal{I}_E\boldsymbol{\xi}\right)\right] \\ &= T_1 + T_2 + T_3. \end{aligned} \tag{3.50}$$

We bound the three terms T_1, T_2 and T_3 in (3.50) separately.

To estimate the term T_1, we first write:

$$\begin{aligned} T_1 :&= \sum_{E\in\mathcal{T}_h} a_E\left((\Pi_E - I)\boldsymbol{\sigma}_h, \mathcal{I}_E\boldsymbol{\xi}\right) \\ &= \sum_{E\in\mathcal{T}_h} \left[a_E\left((\Pi_E - I)(\boldsymbol{\sigma}_h - \boldsymbol{\sigma}), \mathcal{I}_E\boldsymbol{\xi}\right) + a_E\left((\Pi_E - I)\boldsymbol{\sigma}, \mathcal{I}_E\boldsymbol{\xi}\right)\right] \\ &= \sum_{E\in\mathcal{T}_h} a_E\left((\Pi_E - I)(\boldsymbol{\sigma}_h - \boldsymbol{\sigma}), \mathcal{I}_E\boldsymbol{\xi} - \boldsymbol{\xi}\right) + \sum_{E\in\mathcal{T}_h} a_E\left((\Pi_E - I)(\boldsymbol{\sigma}_h - \boldsymbol{\sigma}), \boldsymbol{\xi} - \Pi_E\boldsymbol{\xi}\right) \\ &+ \sum_{E\in\mathcal{T}_h} a_E\left((\Pi_E - I)\boldsymbol{\sigma}, \mathcal{I}_E\boldsymbol{\xi} - \boldsymbol{\xi}\right) + \sum_{E\in\mathcal{T}_h} a_E\left((\Pi_E - I)\boldsymbol{\sigma}, \boldsymbol{\xi} - \Pi_E\boldsymbol{\xi}\right). \end{aligned} \tag{3.51}$$

Now, by employing the continuity of $a_E(\cdot,\cdot)$, standard polynomial approximation results, Proposition 3.3.2 and estimate (3.38), we have

$$\begin{aligned} T_1 &\lesssim \left(||\boldsymbol{\sigma}_h - \boldsymbol{\sigma}||_0 + ||\boldsymbol{\sigma} - \Pi_h\boldsymbol{\sigma}||_0\right)\left(||\mathcal{I}_h\boldsymbol{\xi} - \boldsymbol{\xi}||_0 + ||\boldsymbol{\xi} - \Pi_h\boldsymbol{\xi}||_0\right) \\ &\lesssim h\left(||\mathcal{I}_h\boldsymbol{\xi} - \boldsymbol{\xi}||_0 + ||\boldsymbol{\xi} - \Pi_h\boldsymbol{\xi}||_0\right) \lesssim h^2|\boldsymbol{\xi}|_1 \\ &\lesssim h^2||\boldsymbol{\varphi}||_2, \end{aligned} \tag{3.52}$$

where Π_h is the operator that locally coincides with Π_E, for every $E \in \mathcal{T}_h$.

To estimate the term T_2, we recall that $\boldsymbol{\xi} := \mathbb{C}\boldsymbol{\varepsilon}(\boldsymbol{\varphi})$ to write

$$\begin{aligned} T_2 := a(\boldsymbol{\sigma}_h - \boldsymbol{\sigma}, \mathcal{I}_h\boldsymbol{\xi}) &= \int_\Omega \mathbb{D}\,(\boldsymbol{\sigma}_h - \boldsymbol{\sigma}) : \mathcal{I}_h\boldsymbol{\xi}\ \mathrm{d}\Omega \\ &= \int_\Omega \mathbb{D}\,(\boldsymbol{\sigma}_h - \boldsymbol{\sigma}) : (\mathcal{I}_h\boldsymbol{\xi} - \boldsymbol{\xi})\ \mathrm{d}\Omega + \int_\Omega \mathbb{D}\,(\boldsymbol{\sigma}_h - \boldsymbol{\sigma}) : \boldsymbol{\xi}\ \mathrm{d}\Omega \\ &= \int_\Omega \mathbb{D}\,(\boldsymbol{\sigma}_h - \boldsymbol{\sigma}) : (\mathcal{I}_h\boldsymbol{\xi} - \boldsymbol{\xi})\ \mathrm{d}\Omega + \int_\Omega \mathbb{D}\,(\boldsymbol{\sigma}_h - \boldsymbol{\sigma}) : \mathbb{C}\boldsymbol{\varepsilon}(\boldsymbol{\varphi})\ \mathrm{d}\Omega \\ &= \int_\Omega \mathbb{D}\,(\boldsymbol{\sigma}_h - \boldsymbol{\sigma}) : (\mathcal{I}_h\boldsymbol{\xi} - \boldsymbol{\xi})\ \mathrm{d}\Omega + \int_\Omega \mathbf{div}\,(\boldsymbol{\sigma}_h - \boldsymbol{\sigma}) \cdot \boldsymbol{\varphi}\ \mathrm{d}\Omega, \end{aligned}$$

where an integration by parts has been used in the last step. Now, we recall (see (3.41)) that

$$(\mathbf{div}(\boldsymbol{\sigma}_h - \boldsymbol{\sigma}), \mathbf{q}_h) = 0, \quad \forall \mathbf{q}_h \in U_h(E),$$

Hence, taking $\mathbf{q}_h = \bar{\boldsymbol{\varphi}}_h := \Pi_{RM}\boldsymbol{\varphi}$, we obtain

$$T_2 = \int_\Omega \mathbb{D}\,(\boldsymbol{\sigma}_h - \boldsymbol{\sigma}) : (\mathcal{I}_h\boldsymbol{\xi} - \boldsymbol{\xi})\ \mathrm{d}\Omega + \int_\Omega \mathbf{div}\,(\boldsymbol{\sigma}_h - \boldsymbol{\sigma}) \cdot (\boldsymbol{\varphi} - \bar{\boldsymbol{\varphi}}_h)\ \mathrm{d}\Omega. \tag{3.53}$$

Employing Proposition 3.3.2 and (3.38) we have

$$\begin{aligned} T_2 &\lesssim ||\boldsymbol{\sigma}_h - \boldsymbol{\sigma}||_\Sigma(||\boldsymbol{\xi} - \mathcal{I}_h\,\boldsymbol{\xi}||_0 + ||\boldsymbol{\varphi} - \bar{\boldsymbol{\varphi}}_h||_0) \\ &\lesssim h(||\boldsymbol{\xi} - \mathcal{I}_h\,\boldsymbol{\xi}||_0 + ||\boldsymbol{\varphi} - \bar{\boldsymbol{\varphi}}_h||_0) \lesssim h^2(|\boldsymbol{\xi}|_1 + |\boldsymbol{\varphi}|_1) \\ &\lesssim h^2||\boldsymbol{\varphi}||_2. \end{aligned} \tag{3.54}$$

Concerning the term T_3, it holds:

$$\begin{aligned} T_3 &= \sum_{E\in\mathcal{T}_h} s_E\left((I - \Pi_E)\boldsymbol{\sigma}_h, (I - \Pi_E)\mathcal{I}_E\boldsymbol{\xi}\right) \\ &= \sum_{E\in\mathcal{T}_h} \kappa_E h_E \int_{\partial E} \left[(I - \Pi_E)\boldsymbol{\sigma}_h\mathbf{n}\right]\left[(I - \Pi_E)(\mathcal{I}_E\boldsymbol{\xi})\mathbf{n}\right]\ \mathrm{d}s \\ &\lesssim \sum_{E\in\mathcal{T}_h} h_E^{1/2}||(I - \Pi_E)\boldsymbol{\sigma}_h\mathbf{n}||_{0,\partial E} h_E^{1/2}||(I - \Pi_E)(\mathcal{I}_E\boldsymbol{\xi})\mathbf{n}||_{0,\partial E}. \end{aligned} \tag{3.55}$$

Under assumption (**A1**) and (**A2**), using the same technique developed in [15, 31], we have that

$$h_E^{1/2}||\boldsymbol{\tau}_h\mathbf{n}||_{0,\partial E} \lesssim ||\boldsymbol{\tau}_h\mathbf{n}||_{-1/2,\partial E} \lesssim ||\boldsymbol{\tau}_h||_{0,E} + h_E||\,\mathbf{div}\,\boldsymbol{\tau}_h||_{0,E} \qquad \forall \boldsymbol{\tau}_h \in \Sigma_h(E). \tag{3.56}$$

From (3.55) and (3.56) we then deduce

$$\begin{aligned} T_3 \lesssim &\left(\sum_{E\in\mathcal{T}_h}\left[||(I - \Pi_E)\boldsymbol{\sigma}_h||_{0,E}^2 + h_E^2||\,\mathbf{div}\,\boldsymbol{\tau}_h||_{0,E}^2\right]\right)^{1/2} \cdot \\ &\left(\sum_{E\in\mathcal{T}_h}\left[||(I - \Pi_E)\mathcal{I}_E\boldsymbol{\xi}||_{0,E}^2 + h_E^2||\,\mathbf{div}(\mathcal{I}_E\boldsymbol{\xi})||_{0,E}^2\right]\right)^{1/2}. \end{aligned} \tag{3.57}$$

It holds

$$\begin{aligned} ||(I-\Pi_E)\boldsymbol{\sigma}_h||_{0,E}^2 &= ||(\boldsymbol{\sigma}_h-\boldsymbol{\sigma})+(\boldsymbol{\sigma}-\Pi_E\boldsymbol{\sigma}_h)||_{0,E}^2 \\ &\lesssim ||\boldsymbol{\sigma}_h-\boldsymbol{\sigma}||_{0,E}^2+||\boldsymbol{\sigma}-\Pi_E\boldsymbol{\sigma}_h||_{0,E}^2 \end{aligned} \tag{3.58}$$

and

$$\begin{aligned} ||(I-\Pi_E)\mathcal{I}_E\boldsymbol{\xi}||_{0,E}^2 &= ||(\mathcal{I}_E\boldsymbol{\xi}-\boldsymbol{\xi})+(\boldsymbol{\xi}-\Pi_E(\mathcal{I}_E\boldsymbol{\xi}))||_{0,E}^2 \\ &= ||(\mathcal{I}_E\boldsymbol{\xi}-\boldsymbol{\xi})+(\boldsymbol{\xi}-\Pi_E\boldsymbol{\xi})+(\Pi_E(\boldsymbol{\xi}-\mathcal{I}_E\boldsymbol{\xi}))||_{0,E}^2 \\ &\lesssim ||\mathcal{I}_E\boldsymbol{\xi}-\boldsymbol{\xi}||_{0,E}^2+||\boldsymbol{\xi}-\Pi_E\boldsymbol{\xi}||_{0,E}^2+||\Pi_E(\boldsymbol{\xi}-\mathcal{I}_E\boldsymbol{\xi})||_{0,E}^2. \end{aligned} \tag{3.59}$$

Therefore, we use (3.58), (3.59), the continuity of Π_h, Proposition 3.3.2 and (3.38), to get

$$\begin{aligned} T_3 &\lesssim (||\boldsymbol{\sigma}-\boldsymbol{\sigma}_h||_0+||\boldsymbol{\sigma}-\Pi_h\boldsymbol{\sigma}||_0+h||\operatorname{\mathbf{div}}\boldsymbol{\sigma}_h||_0)\cdot \\ &\qquad (||\boldsymbol{\xi}-\mathcal{I}_h\boldsymbol{\xi}||_0+||\boldsymbol{\xi}-\Pi_h\boldsymbol{\xi}||_0+h||\operatorname{\mathbf{div}}(\mathcal{I}_h\boldsymbol{\xi})||_0) \\ &\lesssim h^2|\boldsymbol{\xi}|_1\lesssim h^2||\boldsymbol{\varphi}||_2. \end{aligned} \tag{3.60}$$

Above, we have also used the estimate $||\operatorname{\mathbf{div}}\boldsymbol{\sigma}_h||_0\lesssim 1$. Now estimate (3.44) follows from (3.46), (3.48), (3.50), (3.52), (3.54) and (3.60). □

3.3.2 Error estimate for the Lagrangre multipliers

The next result gives some information about the convergence of the Lagrange multipliers. To this end we introduce the following two norms on $\Lambda_h(\mathcal{E}_h^I)$:

$$|\boldsymbol{\mu}_h|_{0,h}^2=\sum_{e\in\mathcal{E}_h^I}||\boldsymbol{\mu}_h||_{0,e}^2 \tag{3.61}$$

$$|\boldsymbol{\mu}_h|_{-1/2,h}^2=\sum_{e\in\mathcal{E}_h^I}h_e\,||\boldsymbol{\mu}_h||_{0,e}^2. \tag{3.62}$$

We also need to define the L^2-projection operator

$$\Pi_0^\partial:\left[L^2(\mathcal{E}_h^I)\right]^2\to\left[\mathcal{P}_0(\mathcal{E}_h^I)\right]^2\subseteq\Lambda_h(\mathcal{E}_h^I),$$

such that

$$\int_e\Pi_0^\partial\mathbf{u}\cdot\mathbf{p}\;\mathrm{d}s=\int_e\mathbf{u}\cdot\mathbf{p}\;\mathrm{d}s\quad\forall\mathbf{p}\in[\mathcal{P}_0(e)]^2,\,\forall e\in\mathcal{E}_h^I. \tag{3.63}$$

Theorem 3.3.4. *Let $(\boldsymbol{\sigma},\mathbf{u})$ be the solution of Problem (1.66), and let $(\boldsymbol{\sigma}_h,\mathbf{u}_h,\boldsymbol{\lambda}_h)\in\tilde{\Sigma}_h(\mathcal{T}_h)\times U_h\times\Lambda_h(\mathcal{E}_h^I)$ be the solution of the discrete Problem (3.37). For every element $E\in\mathcal{T}_h$ and edge $e\in\partial E\cap\mathcal{E}_h^I$, if $\{\mathcal{T}_h\}_h$ is regular, it holds*

$$||\Pi_0^\partial(\boldsymbol{\lambda}_h-\mathbf{u})||_{0,e}\lesssim h_E^{1/2}||\boldsymbol{\sigma}-\boldsymbol{\sigma}_h||_{0,E}+h_E^{-1/2}||\bar{\mathbf{u}}_h-\mathbf{u}_h||_{0,E}, \tag{3.64}$$

where $\bar{\mathbf{u}}_h:=\Pi_{RM}\mathbf{u}$, see (3.43).

Proof. Given an element $E \in \mathcal{T}_h$, we fix an edge $e \in \partial E \cap \mathcal{E}_h^I$. Using the unisolvence of the degrees of freedom of $\Sigma_h(E)$, we infer that there exists a unique function $\tilde{\boldsymbol{\tau}}_h \in \Sigma_h(E)$ such that

$$\begin{cases} \tilde{\boldsymbol{\tau}}_h \mathbf{n}_e = \Pi_0^\partial \left(\boldsymbol{\lambda}_h - \mathbf{u}\right), & \text{on } e \\ \tilde{\boldsymbol{\tau}}_h \mathbf{n}_{\tilde{e}} = \mathbf{0} & \forall \tilde{e} \neq e. \end{cases} \tag{3.65}$$

Then, recalling that $\mathbf{div}\, \tilde{\boldsymbol{\tau}}_h \in RM(E)$, an integration by parts, equations (3.65) and an inverse estimate for polynomials, give

$$\begin{aligned} ||\,\mathbf{div}\, \tilde{\boldsymbol{\tau}}_h||_{0,E}^2 &= \int_E \mathbf{div}\, \tilde{\boldsymbol{\tau}}_h \cdot \mathbf{div}\, \tilde{\boldsymbol{\tau}}_h \mathrm{d}E = \int_{\partial E} \tilde{\boldsymbol{\tau}}_h \mathbf{n} \cdot \mathbf{div}\, \tilde{\boldsymbol{\tau}}_h \,\mathrm{d}s \\ &\leq ||\Pi_0^\partial \left(\boldsymbol{\lambda}_h - \mathbf{u}\right)||_{0,e} ||\,\mathbf{div}\, \tilde{\boldsymbol{\tau}}_h||_{0,e} \\ &\lesssim ||\Pi_0^\partial \left(\boldsymbol{\lambda}_h - \mathbf{u}\right)||_{0,e} h_E^{-1/2} ||\,\mathbf{div}\, \tilde{\boldsymbol{\tau}}_h||_{0,E}. \end{aligned} \tag{3.66}$$

Hence, we get

$$h_E ||\,\mathbf{div}\, \tilde{\boldsymbol{\tau}}_h||_{0,E} \lesssim h_E^{1/2} ||\Pi_0^\partial \left(\boldsymbol{\lambda}_h - \mathbf{u}\right)||_{0,e}. \tag{3.67}$$

Using Lemma 5.1 of [15], from (3.65) and (3.67) we obtain

$$h_E ||\,\mathbf{div}\, \tilde{\boldsymbol{\tau}}_h||_{0,E} + ||\tilde{\boldsymbol{\tau}}_h||_{0,E} \lesssim h_E^{1/2} ||\Pi_0^\partial \left(\boldsymbol{\lambda}_h - \mathbf{u}\right)||_{0,e}. \tag{3.68}$$

Now, in the first equation of (3.37) we take $\boldsymbol{\tau}_h \in \tilde{\Sigma}_h(\mathcal{T}_h)$ such that

$$\boldsymbol{\tau}_h = \tilde{\boldsymbol{\tau}}_h \quad \text{in } E, \quad \text{and} \quad \boldsymbol{\tau}_h = \mathbf{0} \quad \text{in } \Omega \setminus E, \tag{3.69}$$

and using (3.65) we have

$$\int_E \mathbb{D}\boldsymbol{\sigma}_h : \tilde{\boldsymbol{\tau}}_h \,\mathrm{d}E + \int_E \mathbf{u}_h \cdot \mathbf{div}\, \tilde{\boldsymbol{\tau}}_h \,\mathrm{d}E - \int_e \boldsymbol{\lambda}_h \cdot \Pi_0^\partial (\boldsymbol{\lambda}_h - \mathbf{u}) \,\mathrm{d}s = 0. \tag{3.70}$$

On the other hand, employing the constitutive law in (1.66) and the Green's formula, we infer

$$\int_E \mathbb{D}\boldsymbol{\sigma} : \tilde{\boldsymbol{\tau}}_h \,\mathrm{d}E + \int_E \mathbf{u} \cdot \mathbf{div}\, \tilde{\boldsymbol{\tau}}_h \,\mathrm{d}E - \int_e \mathbf{u} \cdot \Pi_0^\partial (\boldsymbol{\lambda}_h - \mathbf{u}) \,\mathrm{d}s = 0. \tag{3.71}$$

Using (3.70) and (3.71) and recalling the fact that $\mathbf{div}\, \tilde{\boldsymbol{\tau}}_h \in RM(E)$ we get

$$\begin{aligned} ||\Pi_0^\partial (\boldsymbol{\lambda}_h - \mathbf{u})||_{0,e}^2 &= \int_e \Pi_0^\partial (\boldsymbol{\lambda}_h - \mathbf{u}) \cdot \Pi_0^\partial (\boldsymbol{\lambda}_h - \mathbf{u}) \,\mathrm{d}s \\ &= \int_e (\boldsymbol{\lambda}_h - \mathbf{u}) \cdot \Pi_0^\partial (\boldsymbol{\lambda}_h - \mathbf{u}) \,\mathrm{d}s \\ &= \int_E \mathbb{D}(\boldsymbol{\sigma}_h - \boldsymbol{\sigma}) : \tilde{\boldsymbol{\tau}}_h \,\mathrm{d}E + \int_E (\mathbf{u}_h - \mathbf{u}) \cdot \mathbf{div}\, \tilde{\boldsymbol{\tau}}_h \,\mathrm{d}E \\ &= \int_E \mathbb{D}(\boldsymbol{\sigma}_h - \boldsymbol{\sigma}) : \tilde{\boldsymbol{\tau}}_h \,\mathrm{d}E + \int_E (\mathbf{u}_h - \bar{\mathbf{u}}_h) \cdot \mathbf{div}\, \tilde{\boldsymbol{\tau}}_h \,\mathrm{d}E. \end{aligned} \tag{3.72}$$

Finally (3.72) and (3.68) give (3.64). □

As a consequence of the Theorem above, we have the following corollary, whose proof is immediate (cf. (3.64), (3.38) and (3.73)).

Corollary 3.3.5. *For each element $E \in \mathcal{T}_h$ and for every edge $e \in \partial E$, we have*

$$|\Pi_0^\partial(\boldsymbol{\lambda}_h - \mathbf{u})|_{-1/2,h} \lesssim h||\boldsymbol{\sigma} - \boldsymbol{\sigma}_h||_{0,\Omega} + ||\bar{\mathbf{u}}_h - \mathbf{u}_h||_{0,\Omega} \tag{3.73}$$

and

$$|\Pi_0^\partial(\boldsymbol{\lambda}_h - \mathbf{u})|_{-1/2,h} \lesssim h^2. \tag{3.74}$$

3.4 Post-processing

In the present section, we introduce a post-processing procedure which leads to achieve a better approximation for the displacement field. More precisely, we will employ the available information, the Lagrange multipliers $\boldsymbol{\lambda}_h$, to construct a non-conforming VEM approximation $\mathbf{u}_h^*$ converging to $\mathbf{u}$ faster than $\mathbf{u}_h$.

Let's start to present the framework of non-conforming VEM, see [18] for more details.

3.4.1 Non-conforming Sobolev spaces

Given $\{\mathcal{T}_h\}_h$, a sequence of regular decomposition of Ω, we define the broken H^1 space on $\mathcal{T}_h$ as

$$H^1(\mathcal{T}_h) := \prod_{E\in\mathcal{T}_h} H^1(E) = \left\{ v \in L^2(\Omega) : v_{|E} \in H^1(E) \right\}. \tag{3.75}$$

Then in particular

$$\left[H^1(\mathcal{T}_h)\right]^2 := \prod_{E\in\mathcal{T}_h} \left[H^1(E)\right]^2 \tag{3.76}$$

is the space of vector-valued functions that, locally, are in $[H^1(E)]^2$. For the vector space (3.76), we introduce the corresponding broken seminorm and norm

$$|\mathbf{v}|^2_{1,\mathcal{T}_h} := \sum_{E\in\mathcal{T}_h} ||\nabla \mathbf{v}||^2_{0,E}, \qquad ||\mathbf{v}||^2_{1,\mathcal{T}_h} := \sum_{E\in\mathcal{T}_h} ||\mathbf{v}||^2_{1,E}. \tag{3.77}$$

In order to define non-conforming Sobolev spaces associated with polygonal decomposition, we need to fix some additional notation. Let e be an edge in $\mathcal{E}_h^I$. Then, there are two adjacent elements $E^\pm$ which share the same edge e. We write $\mathbf{n}_{E^+}$, $\mathbf{n}_{E^-}$ for the exterior unit normal on ∂E^+ and ∂E^-, respectively. Then, for $\mathbf{v} \in [H^1(\mathcal{T}_h)]^2$, we define the jump operator across an edge $e \in \mathcal{E}_h$ as

$$[\![\mathbf{v}]\!] := \begin{cases} \mathbf{v}^+ \otimes \mathbf{n}_{E^+} + \mathbf{v}^- \otimes \mathbf{n}_{E^-} & \text{on } e \in \mathcal{E}_h^I \\ \mathbf{v} \otimes \mathbf{n}_e & \text{on } e \in \mathcal{E}_h^B, \end{cases} \tag{3.78}$$

where $\otimes$ denotes the usual tensor product of vectors. Now, using the previous notation and always considering the problem with homogeneous Dirichlet boundary conditions, we introduce the global non-conforming H^1 space as follows

$$H_0^{1,nc}(\mathcal{T}_h) := \left\{ \mathbf{v} \in \left[H^1(\mathcal{T}_h)\right]^2 \, : \, \int_e [\![\mathbf{v}]\!] \, \mathrm{d}s = 0 \quad \forall e \in \mathcal{E}_h \right\}. \tag{3.79}$$

We remark that the seminorm $|\cdot|_{1,\mathcal{T}_h}$ is a norm for functions in $H_0^{1,nc}(\mathcal{T}_h)$ and that the following Poincaré inequality holds true (see [18, 66]):

$$||\mathbf{v}||_0 \lesssim |\mathbf{v}|_{1,\mathcal{T}_h} \quad \forall \mathbf{v} \in H_0^{1,nc}(\mathcal{T}_h). \tag{3.80}$$

3.4.2 A low-order non-conforming Virtual Element Method

We briefly highlight the main features of a low-order non-conforming VEM according to [18, 66]. Given a polygon $E \in \mathcal{T}_h$, we define the local non-conforming virtual space as

$$U_h^*(E) := \left\{ \mathbf{v}_h^* \in \left[H^1(E)\right]^2 \, : \, \frac{\partial \mathbf{v}_h^*}{\partial \mathbf{n}} = \nabla \mathbf{v}_h^* \mathbf{n} \in [\mathcal{P}_0(e)]^2 \quad \forall e \in \partial E, \quad \Delta \mathbf{v}_h^* = \mathbf{0} \right\}. \tag{3.81}$$

Accordingly, for the local spaces $U_h^*(E)$, we can take the following degrees of freedom:

$$\mathbf{v}_h^* \to \frac{1}{|e|} \int_e \mathbf{v}_h^* \, \mathrm{d}s. \tag{3.82}$$

Therefore, we infer that the dimension of space (3.81) is

$$\dim(U_h^*(E)) := 2n_e^E, \tag{3.83}$$

where we recall that n_e^E is the number of element edges. The unisolvence of the degrees of freedom defined in (3.82) is given by the following proposition, whose proof can be found, i.e., in [18].

Proposition 3.4.1. *Let E a simple polygon with n_e^E edges, and let $U_h^*(E)$ be the space defined in (3.81). The degrees of freedom (3.82) are unisolvent for $U_h^*(E)$.*

The global non-conforming virtual element space is given by

$$U_h^*(\mathcal{T}_h) := \left\{ \mathbf{v}_h^* \in H_0^{1,nc}(\mathcal{T}_h) \, : \, \mathbf{v}_{h|_E}^* \in U_h^*(E) \quad \forall \, E \in \mathcal{T}_h \right\}. \tag{3.84}$$

We also need to recall the projection operator $\Pi^\nabla : [H^1(E)]^2 \to [\mathcal{P}_1(E)]^2$, defined by

$$\begin{aligned} &\int_E \nabla(\Pi^\nabla \mathbf{v}_h^*) : \nabla \mathbf{q} \, \mathrm{d}E = \int_E \nabla \mathbf{v}_h^* : \nabla \mathbf{q} \, \mathrm{d}E \quad \forall \mathbf{q} \in [\mathcal{P}_1(E)]^2 \\ &\int_{\partial E} \Pi^\nabla \mathbf{v}_h^* \, \mathrm{d}E = \int_{\partial E} \mathbf{v}_h^* \, \mathrm{d}E. \end{aligned} \tag{3.85}$$

Furthermore, the following estimates will be useful in the sequel.

Proposition 3.4.2. *Under assumptions* (**A1**) *and* (**A2**), *for every* $E \in \mathcal{T}_h$ *and every* $\mathbf{v}_h^* \in U_h^*(E)$, *it holds*

$$|\mathbf{v}_h^*|_{1,E} \lesssim h_E^{-1} ||\mathbf{v}_h^*||_{0,E} \tag{3.86}$$

and

$$||\mathbf{v}_h^*||_{0,E} \lesssim h_E^{1/2} ||\Pi_0^\partial \mathbf{v}_h^*||_{0,\partial E}. \tag{3.87}$$

Proof. We first notice that, since $\mathbf{v}_h^* \in U_h^*(E)$ is harmonic in E, we have

$$|\mathbf{v}_h^*|_{1,E}^2 = \int_{\partial E} \nabla \mathbf{v}_h^* \mathbf{n} \cdot \mathbf{v}_h^* \, \mathrm{d}s \leq ||\nabla \mathbf{v}_h^* \mathbf{n}||_{0,\partial E} \, ||\mathbf{v}_h^*||_{0,\partial E}. \tag{3.88}$$

Recalling that $(\nabla \mathbf{v}_h^* \mathbf{n})_{|\partial E}$ is a piecewise constant vectorial function, under assumptions (**A1**) and (**A2**), the 1D inverse estimate

$$||\nabla \mathbf{v}_h^* \mathbf{n}||_{0,\partial E} \lesssim h_E^{-1/2} ||\nabla \mathbf{v}_h^* \mathbf{n}||_{-1/2,\partial E}$$

holds true. Therefore, we get (cf. [15] and recall again that $\mathbf{div}\, \nabla \mathbf{v}_h^* = 0$)

$$||\nabla \mathbf{v}_h^* \mathbf{n}||_{0,\partial E} \lesssim h_E^{-1/2} ||\nabla \mathbf{v}_h^*||_{0,E} = h_E^{-1/2} |\mathbf{v}_h^*|_{1,E}. \tag{3.89}$$

Hence, from (3.88) we get

$$|\mathbf{v}_h^*|_{1,E} \lesssim h_E^{-1/2} ||\mathbf{v}_h^*||_{0,\partial E}. \tag{3.90}$$

We then exploit a scaled trace inequality, see for instance [42], to infer that it holds

$$|\mathbf{v}_h^*|_{1,E} \lesssim h_E^{-1/2} ||\mathbf{v}_h^*||_{0,E}^{1/2} \left(|\mathbf{v}_h^*|_{1,E}^2 + h_E^{-2} ||\mathbf{v}_h^*||_{0,E}^2 \right)^{1/4}. \tag{3.91}$$

Hence, we get

$$|\mathbf{v}_h^*|_{1,E} \lesssim h_E^{-1/2} ||\mathbf{v}_h^*||_{0,E}^{1/2} \, |\mathbf{v}_h^*|_{1,E}^{1/2} + h_E^{-1} ||\mathbf{v}_h^*||_{0,E}. \tag{3.92}$$

Using the Young's inequality, we obtain

$$|\mathbf{v}_h^*|_{1,E} \lesssim \frac{1}{2\delta} h_E^{-1} ||\mathbf{v}_h^*||_{0,E} + \frac{\delta}{2} |\mathbf{v}_h^*|_{1,E} + h_E^{-1} ||\mathbf{v}_h^*||_{0,E}, \tag{3.93}$$

where $\delta > 0$ is at our disposal. We now choose δ sufficiently small to absorb in the left-hand side the second term of the right-hand side, and thus get (3.86).

To prove (3.87), we first split $\mathbf{v}_h^* \in U_h^*(E)$ as

$$\mathbf{v}_h^* = (\mathbf{v}_h^* - \bar{\mathbf{v}}_h^*) + \bar{\mathbf{v}}_h^* = \mathbf{w}_h^* + \bar{\mathbf{v}}_h^*, \tag{3.94}$$

where the constant vector $\bar{\mathbf{v}}_h^*$ is defined by

$$\bar{\mathbf{v}}_h^* = \frac{1}{|\partial E|} \int_{\partial E} \mathbf{v}_h^* \, \mathrm{d}s.$$

and $\mathbf{w}_h^* := \mathbf{v}_h^* - \bar{\mathbf{v}}_h^*$. Then, a direct computation shows that

$$||\mathbf{v}_h^*||_{0,E} \leq ||\mathbf{w}_h^*||_{0,E} + ||\bar{\mathbf{v}}_h^*||_{0,E} \lesssim ||\mathbf{w}_h^*||_{0,E} + h_E^{1/2}||\bar{\mathbf{v}}_h^*||_{0,\partial E}. \tag{3.95}$$

To estimate $||\mathbf{w}_h^*||_{0,E}$, we notice that $\mathbf{w}_h^*$ has zero mean value on ∂E. Therefore, a Poincaré-type estimate gives, see for instance [72]:

$$||\mathbf{w}_h^*||_{0,E} \lesssim h_E|\mathbf{w}_h^*|_{1,E}. \tag{3.96}$$

Using that $\nabla\mathbf{w}_h^*\mathbf{n}$ is piecewise constant on ∂E, we get (cf. also (3.89))

$$\begin{aligned} |\mathbf{w}_h^*|_{1,E}^2 = \int_{\partial E} \nabla\mathbf{w}_h^*\mathbf{n}\cdot\mathbf{w}_h^*\,\mathrm{d}s = \int_{\partial E} \nabla\mathbf{w}_h^*\mathbf{n}\cdot\Pi_0^\partial\mathbf{w}_h^*\,\mathrm{d}s \leq ||\nabla\mathbf{w}_h^*\mathbf{n}||_{0,\partial E}||\Pi_0^\partial\mathbf{w}_h^*||_{0,\partial E} \\ \lesssim h_E^{-1/2}||\Pi_0^\partial\mathbf{w}_h^*||_{0,\partial E}|\mathbf{w}_h^*|_{1,E}. \end{aligned} \tag{3.97}$$

Therefore, we obtain

$$|\mathbf{w}_h^*|_{1,E} \lesssim h_E^{-1/2}||\Pi_0^\partial\mathbf{w}_h^*||_{0,\partial E}. \tag{3.98}$$

Combining (3.95), (3.96) and (3.98), we infer

$$||\mathbf{v}_h^*||_{0,E} \lesssim h_E^{1/2}\left(||\Pi_0^\partial\mathbf{w}_h^*||_{0,\partial E} + ||\bar{\mathbf{v}}_h^*||_{0,\partial E}\right). \tag{3.99}$$

We now notice that, since

$$\int_{\partial E}\Pi_0^\partial\mathbf{w}_h^*\cdot\bar{\mathbf{v}}_h^*\,\mathrm{d}s = 0,$$

it holds

$$||\Pi_0^\partial\mathbf{w}_h^*||_{0,\partial E} + ||\bar{\mathbf{v}}_h^*||_{0,\partial E} \lesssim ||\Pi_0^\partial\mathbf{w}_h^* + \bar{\mathbf{v}}_h^*||_{0,\partial E} = ||\Pi_0^\partial\mathbf{v}_h^*||_{0,\partial E}. \tag{3.100}$$

Now estimate (3.87) follows from (3.99) and (3.100). □

We are ready to prove the following convergence result for a suitable non-conforming post-processed displacement field.

Theorem 3.4.3. *Let $(\boldsymbol{\sigma},\mathbf{u}) \in \Sigma\times U$ be the solution of continuous Problem (1.66) and let $(\boldsymbol{\sigma}_h,\mathbf{u}_h,\boldsymbol{\lambda}_h) \in \tilde{\Sigma}_h(\mathcal{T}_h)\times U_h\times\Lambda_h(\mathcal{E}_h^I)$ be the discrete solution of Problem (3.37). Define $\mathbf{u}_h^* \in U_h^*(\mathcal{T}_h)$ such that it holds:*

$$\Pi_0^\partial(\mathbf{u}_h^* - \boldsymbol{\lambda}_h) = 0. \tag{3.101}$$

Then we have

$$||\mathbf{u} - \mathbf{u}_h^*||_0 \lesssim h^2. \tag{3.102}$$

In addition, if the family of meshes $\{\mathcal{T}_h\}_h$ is also quasi-uniform, it holds

$$|\mathbf{u} - \mathbf{u}_h^*|_{1,\mathcal{T}_h} \lesssim h. \tag{3.103}$$

Proof. For the displacement field $\mathbf{u}$, we define the non-conforming interpolant $\tilde{\mathbf{u}}_h^* \in U_h^*(\mathcal{T}_h)$ imposing:

$$\Pi_0^\partial(\tilde{\mathbf{u}}_h^* - \mathbf{u}) = \mathbf{0} \tag{3.104}$$

for each edge $e \in \mathcal{E}_h$. Due to Proposition 3.4.1, $\tilde{\mathbf{u}}_h^*$ is well-defined. Similarly, $\mathbf{u}_h^* \in U_h^*(\mathcal{T}_h)$ is well-defined by (3.101). Writing now

$$\mathbf{u} - \mathbf{u}_h^* = (\mathbf{u} - \tilde{\mathbf{u}}_h^*) + (\tilde{\mathbf{u}}_h^* - \mathbf{u}_h^*) \tag{3.105}$$

and using the triangle inequality, we have

$$||\mathbf{u} - \mathbf{u}_h^*||_0 \leq ||\mathbf{u} - \tilde{\mathbf{u}}_h^*||_0 + ||\tilde{\mathbf{u}}_h^* - \mathbf{u}_h^*||_0. \tag{3.106}$$

By standard arguments, see [18, 42], we get

$$||\mathbf{u} - \tilde{\mathbf{u}}_h^*||_0 \lesssim h^2. \tag{3.107}$$

To estimate $||\tilde{\mathbf{u}}_h^* - \mathbf{u}_h^*||_0$, we notice that from (3.101) and (3.104), we have

$$\Pi_0^\partial\,(\mathbf{u}_h^* - \tilde{\mathbf{u}}_h^*) = \Pi_0^\partial(\boldsymbol{\lambda}_h - \mathbf{u}). \tag{3.108}$$

Fix an element $E \in \mathcal{T}_h$; due to estimate (3.87) of Proposition 3.4.2 and to (3.108), we get

$$||\mathbf{u}_h^* - \tilde{\mathbf{u}}_h^*||_{0,E} \lesssim h_E^{1/2}||\Pi_0^\partial(\mathbf{u}_h^* - \tilde{\mathbf{u}}_h^*)||_{0,\partial E} = h_E^{1/2}||\Pi_0^\partial(\boldsymbol{\lambda}_h - \mathbf{u})||_{0,\partial E}. \tag{3.109}$$

Summing all the local estimates (3.109) and combining with Corollary 3.3.5, we get

$$||\mathbf{u}_h^* - \tilde{\mathbf{u}}_h^*||_0 \lesssim h^2. \tag{3.110}$$

Estimate (3.102) now follows from (3.106), (3.107) and (3.110). To prove (3.103), we observe that

$$|\mathbf{u} - \mathbf{u}_h^*|_{1,\mathcal{T}_h} \leq |\mathbf{u} - \tilde{\mathbf{u}}_h^*|_{1,\mathcal{T}_h} + |\tilde{\mathbf{u}}_h^* - \mathbf{u}_h^*|_{1,\mathcal{T}_h}. \tag{3.111}$$

By standard arguments, we have

$$|\mathbf{u} - \tilde{\mathbf{u}}_h^*|_{1,\mathcal{T}_h} \lesssim h. \tag{3.112}$$

Using the inverse estimate (3.86) of Proposition 3.4.2, we get

$$\begin{aligned} |\tilde{\mathbf{u}}_h^* - \mathbf{u}_h^*|_{1,\mathcal{T}_h} = \left(\sum_{E\in\mathcal{T}_h} |\tilde{\mathbf{u}}_h^* - \mathbf{u}_h^*|_{1,E}^2\right)^{1/2} &\lesssim \left(\sum_{E\in\mathcal{T}_h} h_E^{-2}||\tilde{\mathbf{u}}_h^* - \mathbf{u}_h^*||_{0,E}^2\right)^{1/2} \\ &\lesssim h^{-1}||\tilde{\mathbf{u}}_h^* - \mathbf{u}_h^*||_0, \end{aligned} \tag{3.113}$$

where in the last step we have used that the family of meshes is quasi-uniform. Since

$$||\tilde{\mathbf{u}}_h^* - \mathbf{u}_h^*||_0 \leq ||\tilde{\mathbf{u}}_h^* - \mathbf{u}||_0 + ||\mathbf{u} - \mathbf{u}_h^*||_0,$$

from (3.108) and (3.102), estimate (3.113) leads to

$$|\tilde{\mathbf{u}}_h^* - \mathbf{u}_h^*|_{1,\mathcal{T}_h} \lesssim h. \tag{3.114}$$

Estimate (3.103) now follows from (3.111), (3.112) and (3.114). □

3.5 Numerical Results

In this section, we validate the proposed VEM hybridized approach through some numerical experiments. We first give some numerical evidence to the theoretical results. Then, we compare the solving time of the conforming and hybridized VE method, showing the best performance of this latter procedure, especially for the 3D case. We will consider the following two test problems.

Test case 2D. Given $\Omega_1 = [0,1]^2$ the unit square, we consider the following analytical solution

$$\mathbf{u} := \begin{pmatrix} 0.5(\sin(2\pi x))^2 \sin(2\pi y)\cos(2\pi y) \\ -0.5(\sin(2\pi y))^2 \sin(2\pi x)\cos(2\pi x) \end{pmatrix}. \tag{3.115}$$

The loading term $\mathbf{f}$ is computed accordingly. For this problem we consider a homogeneous and isotropic material with Lamé coefficients $\lambda = 10^5$ and $\mu = 0.5$ (nearly incompressible material).

Test case 3D. Given the unit cube $\Omega_2 = [0,1]^3$, we consider a 3D elastic problem with the following exact displacement solution and load term:

$$\begin{cases} u1 = u2 = u3 = 10S(x,y,z) \\ f_1 = -10\pi^2((\lambda+\mu)cos(\pi x)sin(\pi y + \pi z) - (\lambda + 4\mu)S(x,y,z)) \\ f_2 = -10\pi^2((\lambda+\mu)cos(\pi y)sin(\pi x + \pi z) - (\lambda + 4\mu)S(x,y,z)) \\ f_3 = -10\pi^2((\lambda+\mu)cos(\pi z)sin(\pi x + \pi y) - (\lambda + 4\mu)S(x,y,z)) \end{cases} \tag{3.116}$$

where $S(x,y,z) = \sin(\pi x)\sin(\pi y)\sin(\pi z)$. In this case, we consider a compressible material where the Lamé constants are $\lambda = 1$ and $\mu = 1$.

Mesh. In order to test our problems we consider two packages of meshes of four types each, see Figure 3.2:

- **2D meshes.** The unit square Ω_1 is discretized as follows: i) `Square`, a uniform mesh composed by standard structured squares; ii) `Tria`, a Delanuay triangolation of the domain Ω_1 [78]; iii) `Hexagon`, a mesh composed by regular haxagons; iv) `Rand`, a mesh composed by random polygons generated with **Polymesher** [83].
- **3D meshes.** For the unit cube Ω_2, we take: a) `Cube`, a uniform mesh composed by standard structured cubes; b) `Tetra`, a Delanuay tetrahedralization of the domain Ω_2 [79]; c) `CVT`, a centroidal Voronoi tessellation [60]; d) `Rand`, random polyhedra thanks to Voronoi tessellation achieved with random control points.

We remark that the meshes `CVT` and `Rand` have interesting features which challenge the robustness of the virtual element approach. Indeed, they could have some elements with

tiny faces and edges, and we remark that such case is not covered by the developed theory, i.e., the assumptions (**A1**) and (**A2**) for the two-dimensional case and assumptions (**B1**), (**B2**) and (**B3**) for 3D. In order to assess the convergence rate, for each type of mesh, we define the following mesh-size h:

$$h := \frac{1}{N_E} \sum_{i=1}^{N_E} h_E$$

where we recall that N_E is the number of elements in the mesh, and h_E is the diameter of the polytopal element E. Moreover, as we have seen in the previous chapter, all the error quantities are computed through suitable quadrature rules based on the sub-triangulation and sub-tetrahedralization methods.

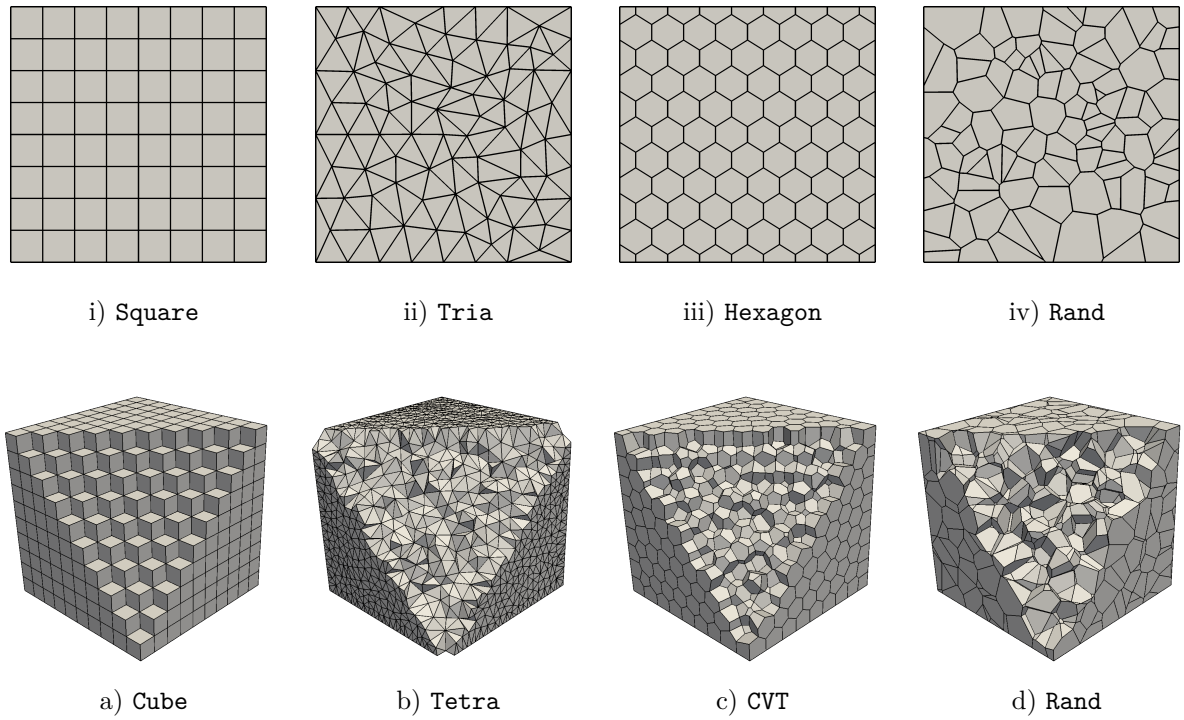

i) `Square` ii) `Tria` iii) `Hexagon` iv) `Rand`

a) `Cube` b) `Tetra` c) `CVT` d) `Rand`

Figure 3.2: Overview of adopted meshes: in the first row the meshes for test case 2D, while in the second row the meshes for test case 3D.

3.5.1 Convergence results

The first numerical results focus on the accuracy of the proposed VEM method using the hybridized procedure on the previous two test cases. To carry out this assessment we use the following error norms:

- L^2 error norm for the displacement field:

$$E_{\mathbf{u}} := \left(\sum_{E \in \mathcal{T}_h} \int_E |\mathbf{u} - \mathbf{u}_h|^2 \, \mathrm{d}E \right)^{1/2} = ||\mathbf{u} - \mathbf{u}_h||_0.$$

- L^2 error on the divergence:

$$E_{\boldsymbol{\sigma},\mathbf{div}} := \left(\sum_{E \in \mathcal{T}_h} \int_E |\,\mathbf{div}(\boldsymbol{\sigma} - \boldsymbol{\sigma}_h)|^2 \, \mathrm{d}E \right)^{1/2} = ||\,\mathbf{div}\,\boldsymbol{\sigma} - \mathbf{div}\,\boldsymbol{\sigma}_h||_0.$$

- L^2 error on the projection:

$$E_{\boldsymbol{\sigma},\Pi} := \left(\sum_{E \in \mathcal{T}_h} \int_E |\boldsymbol{\sigma} - \Pi_E \boldsymbol{\sigma}_h|^2 \, \mathrm{d}E \right)^{1/2} = ||\boldsymbol{\sigma} - \Pi_E \boldsymbol{\sigma}_h||_0.$$

- Discrete error norms for the stress field:

$$E_{\boldsymbol{\sigma}} := \left(\sum_{e \in \mathcal{E}_h} h_e \int_e \kappa \, |(\boldsymbol{\sigma} - \boldsymbol{\sigma}_h)\mathbf{n}|^2 \, \mathrm{d}s \right)^{1/2},$$

  where $\kappa = \frac{1}{2}\mathrm{tr}(\mathbb{D})$ (the material is here homogeneous). Here above, to avoid being too heavy, we use the bi-dimensional notation. For 3D problems, we need to consider the faces instead of the edges. Furthermore, we remark that for the internal edges (faces for 3D) $\boldsymbol{\sigma}_h\mathbf{n}$ is the mean value between the two contributes derived by the adjacent elements. Finally, we observe that the quantity above scales like the internal elastic energy, with respect to the size of the domain and of the elastic coefficients, i.e., $\sim h$.

Results. Figure 3.3 and Figure 3.4 report the h-convergence of the proposed method for test case 2D and 3D, respectively. Relative errors are displayed. As expected, the hybridization leads to an asymptotic convergence rate equal to 1 for all error norms and meshes (in fact, the hybridized schemes are equivalent to the original Hellinger-Reissner methods of [15] and [54]). In Figure 3.4, the $E_{\mathbf{u}}$ and $E_{\boldsymbol{\sigma}}$ plots seem to have a different convergence rate with respect to the theoretical result, but this fact is essentially related to the nature of the problem and the mesh-size. Indeed, refining the meshes, one can observe that, for each error, the convergence rate draws near to 1. Finally, the convergence graphs are very close to each other, which confirms the good robustness of the proposed VE method with respect to the mesh choice.

3.5.2 Post-processing results

The present section is split into two: we first show the superconvergence result, predicted by Theorem 3.3.3, then we exhibit the accuracy of our post-processing, also giving a non-conforming FEM reconstruction on the simplices (triangles and tetrahedra).

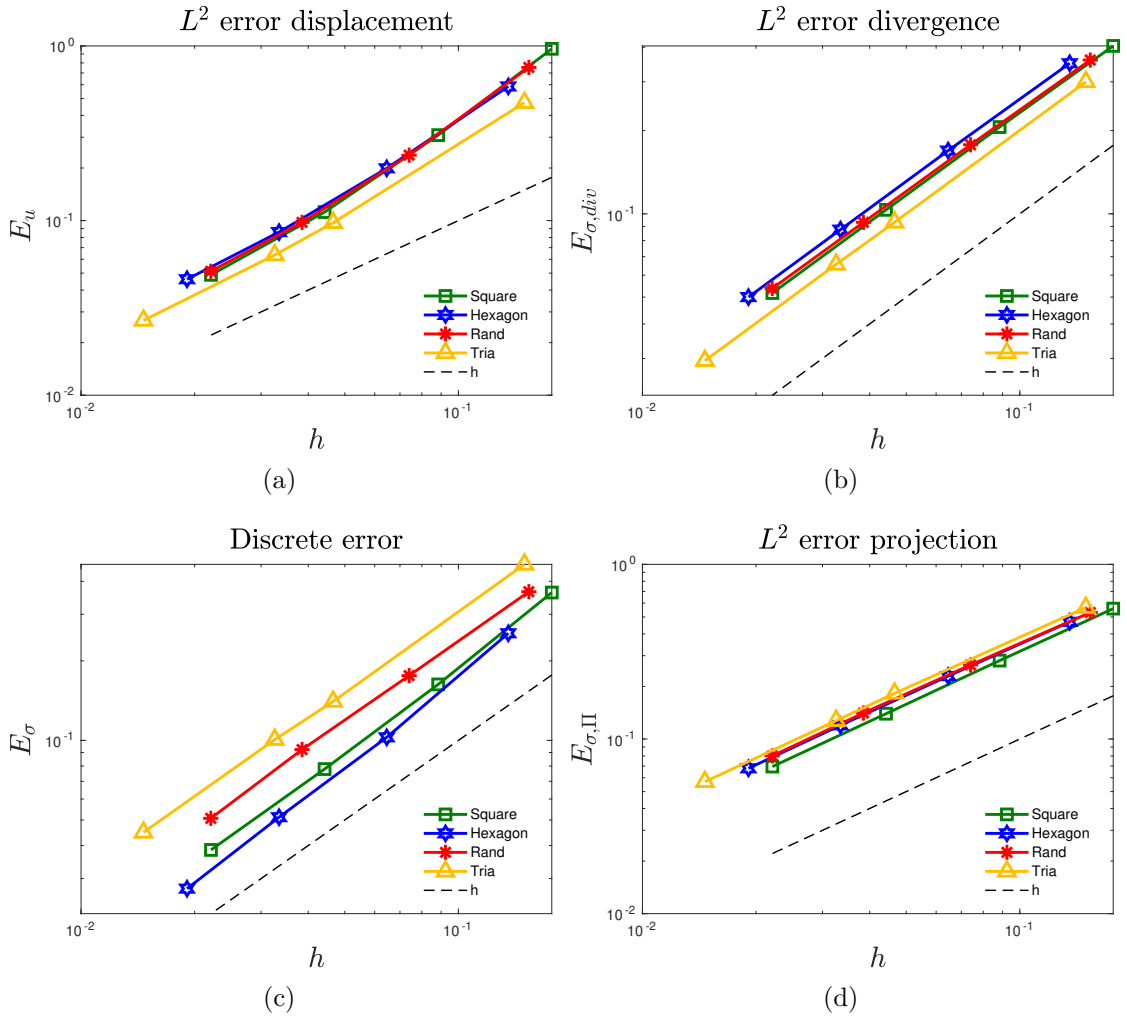

Figure 3.3: Convergence results. h-convergence results for the test case 2D and for all meshes.

Superconvergence. Let's start with the first numerical result and for this purpose we introduce the following error quantities:

- L^2 error norm of the projection onto rigid body motion of the displacement field:

$$E_{\mathbf{u}_{RM}} := \left(\sum_{E \in \mathcal{T}_h} \int_E |\Pi_{RM}\mathbf{u} - \mathbf{u}_h|^2 \, \mathrm{d}E \right)^{1/2} = ||\Pi_{RM}\mathbf{u} - \mathbf{u}_h||_0.$$

  According to Theorem 3.3.3, the expected behaviour of such error is $O(h^2)$ for sufficiently regular problems.

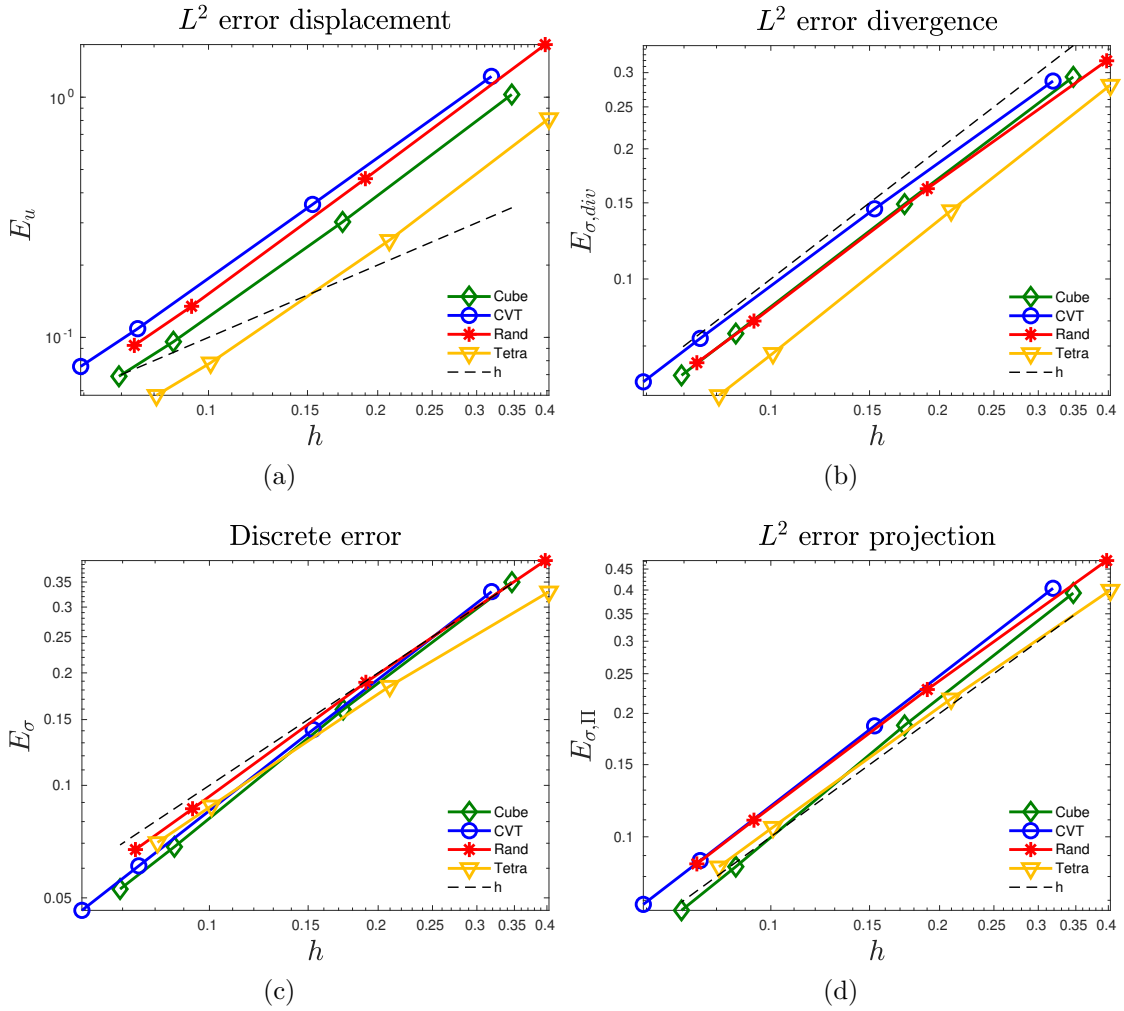

Figure 3.4: Convergence results. h-convergence results for the test case 3D and for all meshes.

- L^2 error norm of the projection onto constants of the displacement field:

$$E_{\mathbf{u}_0} := \left(\sum_{E \in \mathcal{T}_h} \int_E |\Pi_0 \mathbf{u} - \mathbf{u}_h|^2 \, \mathrm{d}E \right)^{1/2} = ||\Pi_0 \mathbf{u} - \mathbf{u}_h||_0.$$

  Since we do not develop a rigorous theoretical analysis for such quantity, we use the numerical investigation to study the behavior of $E_{\mathbf{u}_0}$.

Superconvergece results. In Figure 3.5 and Figure 3.6 we show the convergence lines for the previous errors. Again, relative errors are displayed. The convergence rate for the error norm $E_{\mathbf{u}_{RM}}$ is 2, in accordance with the theoretical results, see (3.44). Instead,

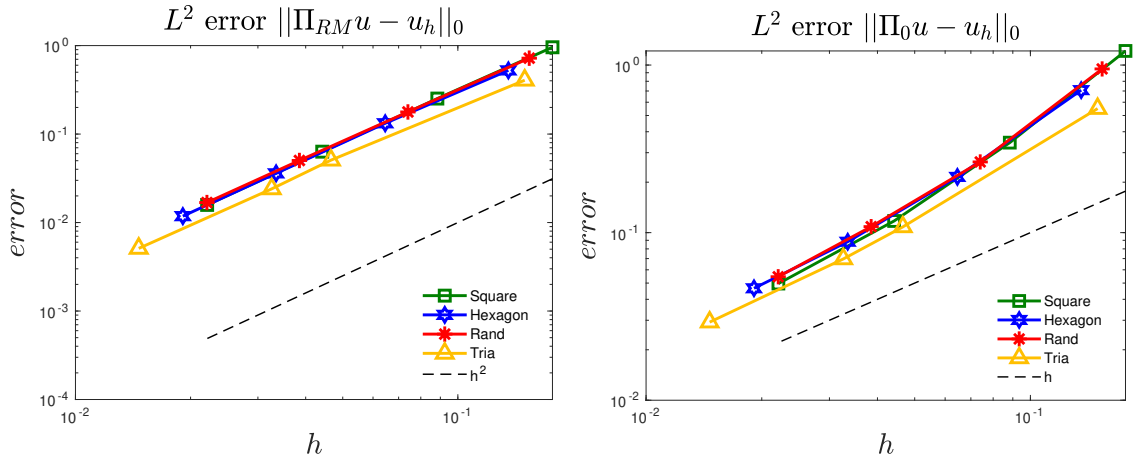

Figure 3.5: Superconvergence results. h-convergence results for test case 2D for all meshes.

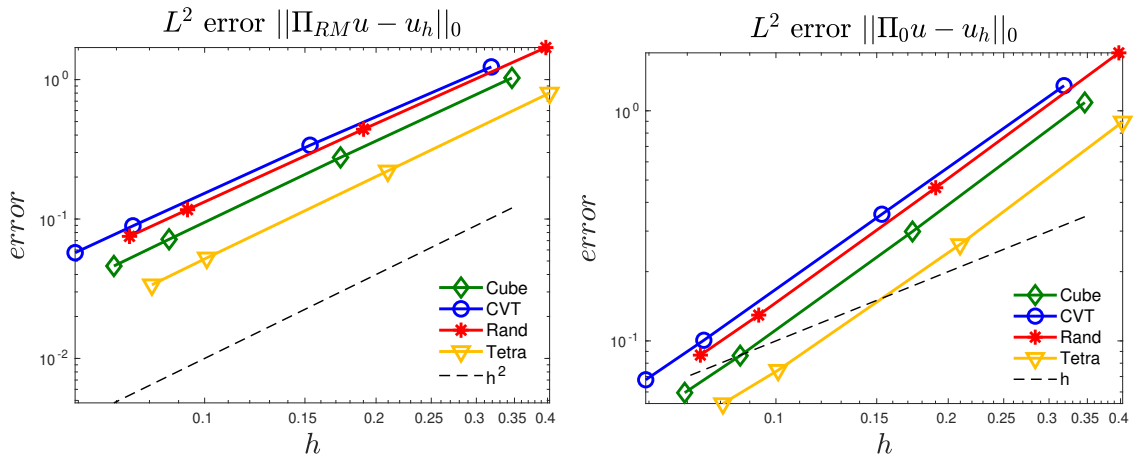

Figure 3.6: Superconvergence results. h-convergence results for test case 3D for all meshes.

the error norm $E_{\mathbf{u}_0}$ is only $O(h)$. This result suggests to us that the superconvergence behavior does not occur for the projection onto constants. Moreover, from these graphs, we can also appreciate the robustness of the VEM concerning element distortions. Indeed, the convergence lines for the four meshes (2D and 3D) are very close to each other.

Post-processing. Since the VE post-processing reconstruction is virtual inside the element, we need to involve the projection operator Π^{∇}, defined by (3.85). Then, we introduce

the following error measures

$$E^0_{\mathbf{u}^*_h} := ||\mathbf{u} - \Pi^\nabla \mathbf{u}^*_h||_0 = \left(\sum_{E \in \mathcal{T}_h} \int_E |\mathbf{u} - \Pi^\nabla \mathbf{u}^*_h|^2 \, \mathrm{d}E \right)^{1/2},$$

and

$$E^1_{\mathbf{u}^*_h} := |\mathbf{u} - \Pi^\nabla \mathbf{u}^*_h|_{1,\mathcal{T}_h} = \left(\sum_{E \in \mathcal{T}_h} \int_E |\nabla \mathbf{u} - \nabla(\Pi^\nabla \mathbf{u}^*_h)|^2 \, \mathrm{d}E \right)^{1/2}.$$

However, we remark that on simplices the function $\mathbf{u}^*_h$ is indeed computable: it corresponds to the vectorial version of the non-conforming Finite Element post-processed solution detailed in [52]. In such a case, the operator Π^∇ is simply the identity.

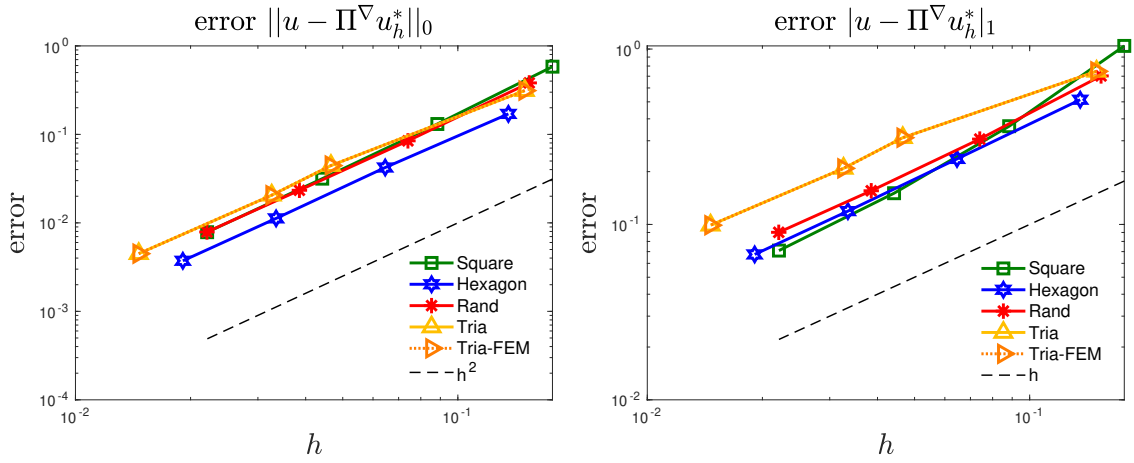

Figure 3.7: Post-processing. Convergence plots for the error $E^0_{\mathbf{u}^*_h}$ and $E^1_{\mathbf{u}^*_h}$ for test case 2D.

Post-processing results. In Figure 3.7 and Figure 3.8 we report the convergence lines for the errors $E^0_{\mathbf{u}^*_h}$ and $E^1_{\mathbf{u}^*_h}$ for both test cases. Relative errors are displaced. The convergence rate for the error $E^0_{\mathbf{u}^*_h}$ is approximately 2, while for the error $E^1_{\mathbf{u}^*_h}$ is 1, as expected by Theorem 3.4.3. Although estimate (3.103) has been proved only for quasi-uniform meshes, our numerical tests suggests that the same convergence behaviour occurs for more general situations (e.g., `Rand` meshes are not quasi-uniform but a first order convergence rate takes place). The convergence lines of the each mesh are close to each other, showing, one more time, the VEM robustness with respect to the deformation of the mesh. In the end, we can also notice that FEM and VEM reconstruction on the simplices (`Tria` and `Tetra` mesh) is the same, as expected.

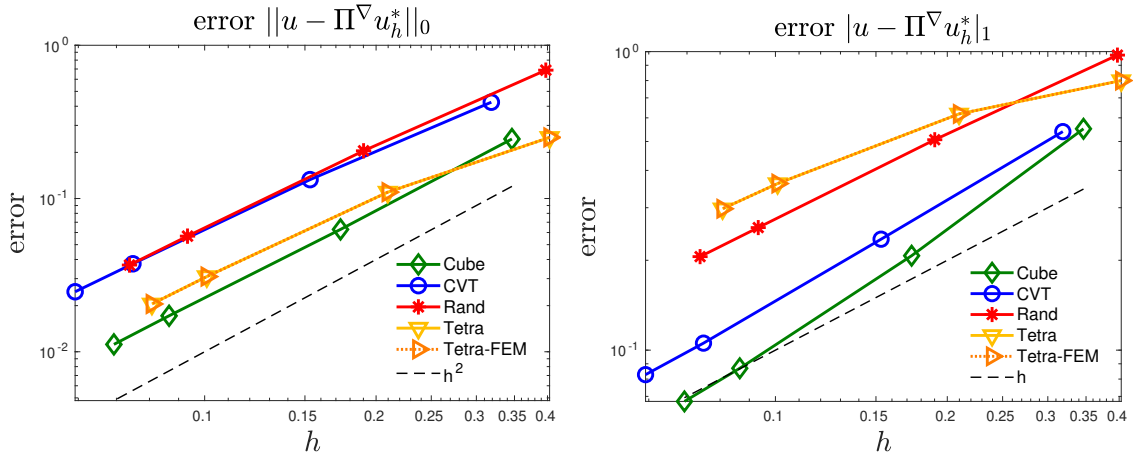

Figure 3.8: Post-processing. Convergence plots for the error $E^0_{\mathbf{u}^*_h}$ and $E^1_{\mathbf{u}^*_h}$ for test case 3D.

3.5.3 Comparison of solving time

Here we report our last numerical result for the hybridization. In this experiment, we qualitatively compare the solving time between the standard low-order VEM approach [15, 54] and the hybridization scheme procedure that we have shown in this chapter. We use the library PETSc, which is an open-source code [19, 20]. In particular, we use the direct solver MUMPS: LU factorization for the standard method; Cholesky for the hybridized one. Moreover, we run our test only on one processor in order to have the same setting for both cases. To better appreciate the results, we report only the 3D case for all meshes.

Results In Table 3.1 and in Table 3.2 we show a comparison between the solving time for the standard VE method and the time of the hybridization procedure (static condensation and solving time) for each mesh refinement step. Moreover, in the column "Hybrid", we also show the percentage of time used to solve the linear system (3.8). We can notice that, refining the meshes, the hybridization procedure has better performance (in time) than the standard procedure. Furthermore, focusing only on the hybridization technique, we observe that the time improvement becomes more and more effective as the solving process time dominates over the one needed to deal with the static condensation (this occurs for larger and larger systems). All the quantities are expressed in seconds.

	Cube			Tetra		
Step	Standard	Hybrid		Standard	Hybrid	
1	0.11	0.11	(38.02%)	0.12	0.11	(32.14%)
2	5.74	3.09	(82.06%)	3.80	2.28	(70.37%)
3	971.33	209.53	(97.15%)	568.12	284.78	(97.43%)
4	4178.47	903.67	(98.78%)	3393.64	1409.92	(98.33%)

Table 3.1: Comparison of solving time between standard approach and hybridization technique for test case 3D. We use `Cube` and `Tetra` meshes.

	CVT			Rand		
Step	Standard	Hybrid		Standard	Hybrid	
1	0.86	0.68	(63.22%)	1.22	0.91	(67.32%)
2	97.88	53.43	(94.88%)	161.21	72.13	(95.04%)
3	6877.68	53.43	(99.56%)	32 015.50	14 565.00	(99.70%)
4	128 626.00	41 000.70	(99.86%)	172 781.00	81 037.80	(99.91%)

Table 3.2: Comparison of solving time between standard approach and hybridization technique for test case 3D. We use `CVT` and `Rand` meshes.

Chapter 4

Numerical investigation of a Virtual Element Method for an augmented Lagrangian formulation

In Chapter 2 and Chapter 3, we introduced and analyzed a low-order virtual element method and its hybridization for linear elasticity problems, respectively. In all these cases, we considered the classical mixed formulation based on the Hellinger-Reissner principle, as the starting point of our discretization procedure. It is well known that for mixed Galerkin methods, we need to satisfy two compatibility conditions, *ellipticity-on-the-kernel* and *inf-sup*, to achieve stable and accurate methods. Such request is reflected in the fact that in the previous low-order VEM schemes (2D and 3D), we take the discrete local space of displacement as rigid body motion and not as the space of constant polynomials. Therefore, a way to use less information is to modify the original variational formulation.

In this chapter, we present a preliminary study for a virtual element scheme on the elasticity problem, but for a modified variational formulation. More precisely, we consider an augmented Lagragian formulation [47, 61]. The advantage, in considering this new formulation, is that the compatibility condition of *ellipticity-on-the-kernel* is automatically satisfied on the whole space of the divergence operator. All this, without changing the solution of the continuous problem. Such formulation allows, for instance, to design methods with a better approximation properties [40] or to give the possibility to reduce the discrete spaces without losing accuracy.

The aim of this chapter is to numerically investigate a virtual element method that is "minimal" for both the stresses and displacements. Since we have not yet developed a strong analysis about it, we will present the method and will show some insightful numerical experiments. For sake of simplicity, we will deal with only the bi-dimensional case, even if we implemented the code also for 3D problems.

The outline of the chapter follows. In Section 4.1 we briefly introduce the augmented Lagrangian formulation. Section 4.2 is devoted to the presentation of the VEM, while in Section 4.3 we introduce some numerical experiments that we have done in order to study the behavior of the proposed method. Finally, in Section 4.4 we draw some conclusions of

this investigation.

4.1 Augmented Lagrangian formulation

We present a different formulation of the elasticity problem (1.74), in the framework of the so-called augmented Lagrangian formulations [40, 46]. As we have said before, the main feature of the approach is the automatic fulfillment of the *ellipticity-on-the-kernel* condition.
Given $\Omega \subset \mathbb{R}^2$ a polygonal domain and $\mathbf{f} \in [L^2(\Omega)]^2$ the loading term, the new modified formulation reads as follows

$$\begin{cases} \text{Find } (\boldsymbol{\sigma}, \mathbf{u}) \in \Sigma \times U \text{ such that} \\ a(\boldsymbol{\sigma}, \boldsymbol{\tau}) + \gamma\,(\mathbf{div}\,\boldsymbol{\sigma}, \mathbf{div}\,\boldsymbol{\tau}) + (\mathbf{div}\,\boldsymbol{\tau}, \mathbf{u}) = -\gamma\,(\mathbf{f}, \mathbf{div}\,\boldsymbol{\tau}) \qquad \forall \boldsymbol{\tau} \in \Sigma \\ (\mathbf{div}\,\boldsymbol{\sigma}, \mathbf{v}) = -(\mathbf{f}, \mathbf{v}) \qquad \forall \mathbf{v} \in U, \end{cases} \tag{4.1}$$

where γ is a positive constant, which depends on the geometry and on the material parameters of the problem. Problem (4.1) is well-posed and admits the same unique solution of standard formulation (1.74), since

$$\mathbf{div}\,\boldsymbol{\sigma} + \mathbf{f} = \mathbf{0} \qquad \text{in } \left[L^2(\Omega)\right]^2. \tag{4.2}$$

However, the bilinear form

$$a_\gamma(\boldsymbol{\sigma}, \boldsymbol{\tau}) := a(\boldsymbol{\sigma}, \boldsymbol{\tau}) + \gamma\,(\mathbf{div}\,\boldsymbol{\sigma}, \mathbf{div}\,\boldsymbol{\tau}) \tag{4.3}$$

is now coercive *over the whole space* Σ. This allows for a different selection of discretization spaces. In particular, with respect to the choice detailed in [15], reduced spaces can be employed in connection with formulation (4.1).

4.2 The Virtual Element Method

Here, we present our proposed VE scheme for the augmented Lagrangian formulation. Let $\{\mathcal{T}_h\}_h$ be a sequence decomposition of the domain Ω into general polygons E satisfying the usual assumption (**A1**) and (**A2**), listed in Section 1.1.3. Following the steps of the previous chapters, we present the virtual element approximation stemming from formulation (4.1).

4.2.1 The local spaces

Stress space. The local approximation space for the stress field is:

$$\begin{aligned} \Sigma_h^0(E) = \Big\{ \boldsymbol{\tau}_h \in & H(\mathbf{div}; E) \;:\; \exists \mathbf{w}^* \in \left[H^1(E)\right]^2 \text{ such that } \boldsymbol{\tau}_h = \mathbb{C}\boldsymbol{\varepsilon}(\mathbf{w}^*); \\ & (\boldsymbol{\tau}_h\,\mathbf{n})_{|e} \in \mathbb{R}^2 \quad \forall e \in \partial E; \quad \mathbf{div}\,\boldsymbol{\tau}_h \in RM(E) \Big\}. \end{aligned} \tag{4.4}$$

For the space $\Sigma_h^0(E)$, we get the following degrees of freedom, see Figure 4.1:

$$\boldsymbol{\tau}_h \to \int_e (\boldsymbol{\tau}_h \mathbf{n})_{|e} \ \mathrm{d}s, \tag{4.5}$$

for each edge e of the element E. In particular, we observe that $\mathbf{div}\,\boldsymbol{\tau}_h$ is completely determined by $(\boldsymbol{\tau}_h\mathbf{n})_{|e}$, for $e \in \partial E$. Indeed, setting (cf. (3.11))

$$\mathbf{div}\,\boldsymbol{\tau}_h = \boldsymbol{\alpha}_E + \beta_E\Big(\mathbf{x} - \mathbf{x}_E\Big)^{\perp}, \tag{4.6}$$

and using the divergence theorem, we infer

$$\boldsymbol{\alpha}_E = \frac{1}{|E|} \sum_{e \in \partial E} \int_e (\boldsymbol{\tau}_h \mathbf{n})_{|e} \ \mathrm{d}s, \tag{4.7}$$

and

$$\beta_E = \frac{1}{\int_E |\mathbf{x} - \mathbf{x}_E|^2 \ dE} \sum_{e \in \partial E} \int_e (\boldsymbol{\tau}_h \mathbf{n})_{|e} \cdot (\mathbf{x} - \mathbf{x}_E)^{\perp} \ \mathrm{d}s. \tag{4.8}$$

Therefore, the dimension of $\Sigma_h^0(E)$ is:

$$\dim(\Sigma_h^0(E)) = 2\, n_e^E,$$

where we recall that n_e^E is the number of the edges of E.

Displacement space. The local approximation space for the displacement field is defined by:

$$U_h^0(E) = \left\{ \mathbf{v}_h \in \Big[L^2(\Omega)\Big]^2 \ : \ \mathbf{v}_h \in [\mathcal{P}_0(E)]^2 \right\}. \tag{4.9}$$

Accordingly, for the local space $U_h^0(E)$ the following degrees of freedom can be taken, see Figure 4.1:

$$\mathbf{v}_h \to \int_E \mathbf{v}_h \ \mathrm{d}E \tag{4.10}$$

and it follows that the dimension of $U_h^0(E)$ is

$$\dim(U_h^0(E)) = 2.$$

Remark 15. *The degrees of freedom of such augmented Lagrangian formulation are constant vectors compared to ones described in Chapter 3.*

4.2.2 The local forms

The local mixed and loading terms are designed accordingly with the description of Sections 2.1.2 and 3.2.2.

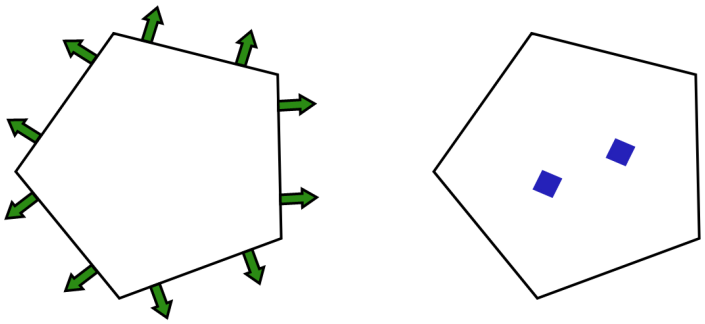

Figure 4.1: Schematic description of the local degrees of freedom: stresses (left); displacements (right).

The local mixed term. Given an element $E \in \mathcal{T}_h$, for every $\boldsymbol{\tau}_h \in \Sigma_h^0(E)$ and $\mathbf{v}_h \in U_h^0(E)$, we notice that

$$(\mathbf{div}\,\boldsymbol{\tau}_h, \mathbf{v}_h)_E = \int_E \mathbf{div}\,\boldsymbol{\tau}_h \cdot \mathbf{v}_h \, \mathrm{d}E \tag{4.11}$$

is computable from the knowledge of the degrees of freedom. Therefore, there is no need to introduce any approximation of the terms $(\mathbf{div}\,\boldsymbol{\tau}, \mathbf{u})$ and $(\mathbf{div}\,\boldsymbol{\sigma}, \mathbf{v})$.

The div-div term. For every $\boldsymbol{\tau}_h$, $\boldsymbol{\sigma}_h \in \Sigma_h^0(E)$, the term

$$(\mathbf{div}\,\boldsymbol{\sigma}_h, \mathbf{div}\,\boldsymbol{\tau}_h)_E = \int_E \mathbf{div}\,\boldsymbol{\sigma}_h \cdot \mathbf{div}\,\boldsymbol{\tau}_h \, \mathrm{d}E \tag{4.12}$$

is computable, see (4.6), (4.7) and (4.8).

The local bilinear form $a_E(\cdot,\cdot)$. The local bilinear form

$$a_E(\boldsymbol{\sigma}_h, \boldsymbol{\tau}_h) = \int_E \mathbb{D}\boldsymbol{\sigma}_h : \boldsymbol{\tau}_h \, \mathrm{d}E\,,$$

requires a slightly different treatment, since we need to introduce a suitable stress projection operator. More precisely, we define $\Pi_E^0 : \Sigma_h^0(E) \to [\mathcal{P}_0(E)]_s^{2\times 2}$ by the following condition

$$\int_E \Pi_E^0 \boldsymbol{\tau}_h : \boldsymbol{\pi}_0 \, \mathrm{d}E = \int_E \boldsymbol{\tau}_h : \boldsymbol{\pi}_0 \, \mathrm{d}E \qquad \forall \boldsymbol{\pi}_0 \in [\mathcal{P}_0(E)]_s^{2\times 2}\,. \tag{4.13}$$

Now, using the divergence theorem, the above condition becomes

$$\int_E \Pi_E^0 \boldsymbol{\tau}_h : \boldsymbol{\pi}_0 \, \mathrm{d}E = -\int_E \mathbf{div}\,\boldsymbol{\tau}_h \cdot \mathbf{p}_1 \, \mathrm{d}E + \int_{\partial E} (\boldsymbol{\tau}_h \mathbf{n}) \cdot \mathbf{p}_1 \, \mathrm{d}s, \tag{4.14}$$

where, given $\boldsymbol{\pi}_0 \in [\mathcal{P}_0(E)]_s^{2\times 2}$, the vectorial polynomial $\mathbf{p}_1 \in [\mathcal{P}_1(E)]^2$ is such that $\boldsymbol{\varepsilon}(\mathbf{p}_1) = \boldsymbol{\pi}_0$. Hence, the operator Π_E^0 is clearly computable. Then, the approximation of $a_E(\cdot,\cdot)$

reads:

$$\begin{aligned} a_E^h(\boldsymbol{\sigma}_h, \boldsymbol{\tau}_h) &:= a_E(\Pi_E^0 \boldsymbol{\sigma}_h, \Pi_E^0 \boldsymbol{\tau}_h) + s_E\left((I - \Pi_E^0)\boldsymbol{\sigma}_h, (I - \Pi_E^0)\boldsymbol{\tau}_h\right) \\ &= \int_E \mathbb{D}(\Pi_E^0 \boldsymbol{\sigma}_h) : (\Pi_E^0 \boldsymbol{\tau}_h) \, \mathrm{d}E + s_E\left((I - \Pi_E^0)\boldsymbol{\sigma}_h, (I - \Pi_E^0)\boldsymbol{\tau}_h\right), \end{aligned} \tag{4.15}$$

where $s_E(\cdot, \cdot)$ is the following stabilization term, see Chapter 2:

$$s_E(\boldsymbol{\sigma}_h, \boldsymbol{\tau}_h) := \kappa_E h_E \int_{\partial E} \boldsymbol{\sigma}_h \, \mathbf{n} \cdot \boldsymbol{\tau}_h \, \mathbf{n} \, \mathrm{d}s \tag{4.16}$$

The right-hand side terms. In this formulation we have two right-hand side terms: the loading term

$$(\mathbf{f}, \mathbf{v}_h) = \int_\Omega \mathbf{f} \cdot \mathbf{v}_h \, \mathrm{d}\Omega = \sum_{E \in \mathcal{T}_h} \int_E \mathbf{f} \cdot \mathbf{v}_h \, \mathrm{d}E, \tag{4.17}$$

and the term derived by (4.2)

$$(\mathbf{f}, \mathbf{div}\, \boldsymbol{\tau}_h) = \int_\Omega \mathbf{f} \cdot \mathbf{div}\, \boldsymbol{\tau}_h \, \mathrm{d}\Omega = \sum_{E \in \mathcal{T}_h} \int_E \mathbf{f} \cdot \mathbf{div}\, \boldsymbol{\tau}_h \, \mathrm{d}E. \tag{4.18}$$

To compute (4.17) and (4.18), we use suitable quadrature rules for polygonal domains, see for instance [70, 71, 80].

4.2.3 The discrete scheme

The global approximation space for the stress field is defined by glueing the local approximation spaces, see (4.4):

$$\Sigma_h^0 = \left\{ \boldsymbol{\tau}_h \in H(\mathbf{div}; \Omega) \ : \ \boldsymbol{\tau}_{h|E} \in \Sigma_h^0(E) \quad \forall E \in \mathcal{T}_h \right\}. \tag{4.19}$$

For the global approximation of the displacement field, we take, see (4.9):

$$U_h^0 = \left\{ \mathbf{v}_h \in \left[L^2(\Omega)\right]^2 \ : \ \mathbf{v}_{h|E} \in U_h^0(E) \quad \forall E \in \mathcal{T}_h \right\}. \tag{4.20}$$

In addition, given a local approximation of $a_E(\cdot, \cdot)$, see (4.15), we set

$$a_h(\boldsymbol{\sigma}_h, \boldsymbol{\tau}_h) := \sum_{E \in \mathcal{T}_h} a_E^h(\boldsymbol{\sigma}_h, \boldsymbol{\tau}_h). \tag{4.21}$$

Then, the method that we consider is defined by

$$\begin{cases} \text{Find } (\boldsymbol{\sigma}_h, \mathbf{u}_h) \in \Sigma_h^0 \times U_h^0 \text{ such that} \\ a_h(\boldsymbol{\sigma}_h, \boldsymbol{\tau}_h) + \gamma(\mathbf{div}\, \boldsymbol{\sigma}_h, \mathbf{div}\, \boldsymbol{\tau}_h) + (\mathbf{div}\, \boldsymbol{\tau}_h, \mathbf{u}_h) = -\gamma(\mathbf{f}, \mathbf{div}\, \boldsymbol{\tau}_h) & \forall \boldsymbol{\tau}_h \in \Sigma_h^0 \\ (\mathbf{div}\, \boldsymbol{\sigma}_h, \mathbf{v}_h) = -(\mathbf{f}, \mathbf{v}_h) & \forall \mathbf{v}_h \in U_h^0. \end{cases} \tag{4.22}$$

We remark that the couple (Σ_h^0, U_h^0) leads to a scheme for which a function $\boldsymbol{\tau}_h$ in the discrete kernel

$$K_h := \left\{ \boldsymbol{\tau}_h \in \Sigma_h^0 \,:\, (\mathbf{div}\,\boldsymbol{\tau}_h, \mathbf{v}_h) = 0 \quad \forall \mathbf{v}_h \in U_h \right\} \tag{4.23}$$

does not necessarily satisfies $\mathbf{div}\,\boldsymbol{\tau}_h = \mathbf{0}$ pointwise. If one uses (Σ_h^0, U_h^0) in connection with the standard Hellinger-Reissner formulation (1.74), this is severe drawback, which is overcome by the stabilizing effect of the augmented Lagrangian approach.

4.3 Numerical investigation

In this section, we present some numerical experiments that we have used to investigate the behavior and the approximation properties of the proposed VE method for this modified formulation. In Section 4.3.1, we address the accuracy of our scheme, showing what happens in three simple test cases, whereas in Section 4.3.2, we focus our attention on some further interesting issues about the proposed method.

We consider the unit square $\Omega = [0,1]^2$ as the domain of our problems. The material is assumed to be homogeneous and isotropic with the following Lamè coefficients: $\lambda = 1$ and $\mu = 1$ (compressible material). For these problems, the analytical solution is available and is chosen in terms of displacement field. The loading term $\mathbf{f}$ is computed accordingly. The problems are

- **Test case 1 (Patch test).** We consider the following data

$$\mathbf{u} = \begin{pmatrix} 3 \\ -2 \end{pmatrix}, \qquad \mathbf{f} = \mathbf{0}. \tag{4.24}$$

- **Test case 2 (Linear test).** In this test, we take the following data

$$\mathbf{u} = \begin{pmatrix} x + 5y - 3 \\ 2x + y + 1 \end{pmatrix}, \qquad \boldsymbol{\sigma} = \begin{bmatrix} 4 & 7 \\ 7 & 4 \end{bmatrix}, \qquad \mathbf{f} = \mathbf{0}. \tag{4.25}$$

  where solution is linear, the stress tensor constant and the loading term (and divergence) is a null vector.

- **Test case 3 (Quadratic test).** Here, we consider the following data

$$\mathbf{u} = \begin{pmatrix} x^2 \\ 0 \end{pmatrix}, \qquad \boldsymbol{\sigma} = \begin{bmatrix} 6x & 0 \\ 0 & 2x \end{bmatrix}, \qquad \mathbf{f} = \begin{pmatrix} -6 \\ 0 \end{pmatrix}. \tag{4.26}$$

  We have a linear stress tensor and a constant loading term (divergence).

Mesh. We consider the standard unit square $\Omega = [0,1]^2$ as the domain of our problems and we take the following eight types of meshes, see Figure 4.2:

- **standard meshes**:
  a) `Square`, a uniform standard structured squares meshes;
  b) `Tria`, a Delanuay triangolation of the domain Ω, see [78];
  c) `Hexagon`, a mesh composed by regular hexagons;
  d) `Rand`, a mesh composed by random polygons generated with **Polymesher** [83];
- **structured meshes,** that are created from `Square` mesh as follows:
  e) `2TriaR,` a uniform structured triangles meshes, each square is divided in two triangles by a diagonal;
  f) `2TriaHN,` starting from the previous mesh, we add a hanging node on diagonal, so this mesh is composed by quadrilaterals elements;
  g) `4TriaR,` a uniform structured triangles meshes, each square is divided in four triangles by the two diagonals;
  h) `4TriaD,` starting from the previous mesh we move the intersection of the diagonals in order to break the symmetry.

We underline that the `Rand` partitions could be interesting from the computational point of view. Indeed, such meshes contain small edges and so the robustness of the virtual element method will be severely tested. To assess the convergence rate, for each type of mesh, we define the mesh-size parameter h as the mean value of element diameters

$$h := \frac{1}{N_E} \sum_{i=1}^{N_E} h_E,$$

where we recall that h_E is the diameter of the element $E \in \mathcal{T}_h$, while N_E is the number of the elements in $\mathcal{T}_h$.

4.3.1 Accuracy assessment

The present section is devoted to the study of the accuracy of the proposed method and for this aim we consider the following error norms: $E_{\boldsymbol{\sigma}}$, $E_{\boldsymbol{\sigma},\mathbf{div}}$, $E_{\boldsymbol{\sigma},\Pi}$ and $E_{\mathbf{u}}$, whose definitions are in Section 3.5.1.

The numerical campaign has been conducted into two different chronological phases: at first, we have tested all our problems on the general standard meshes; later, in light of the results obtained, we have focused our attention on **Test case 3** evaluating it on the structured meshes. Here, for simplicity, we report the results divided by type of test.

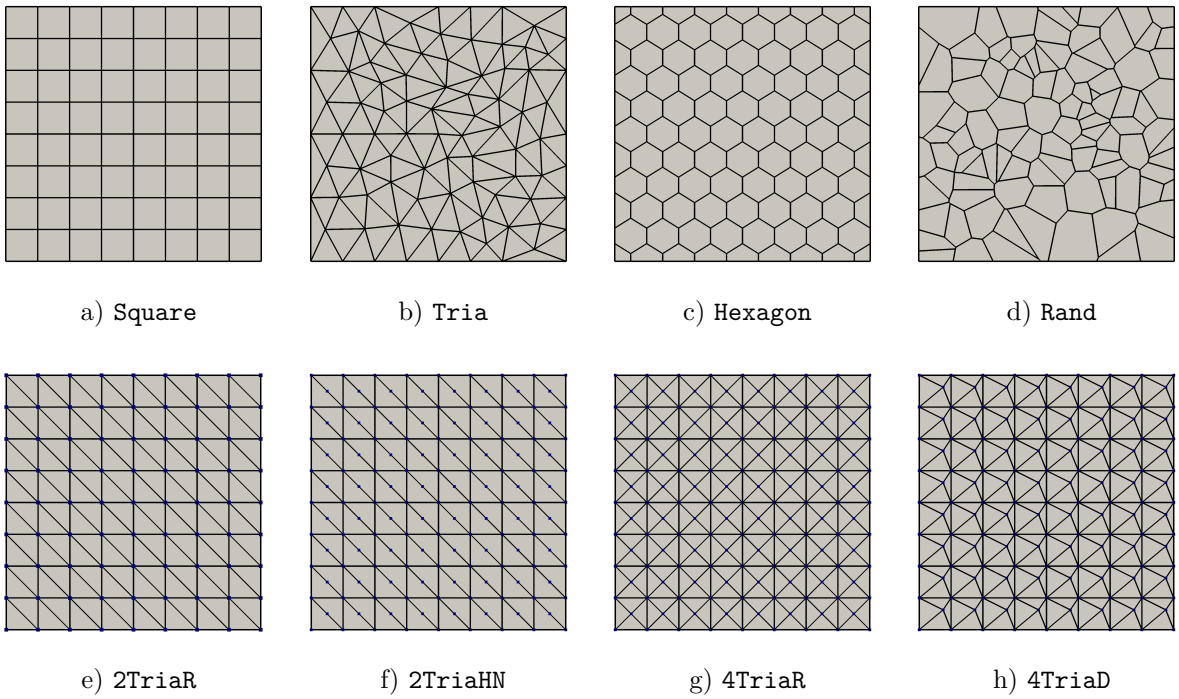

a) `Square` b) `Tria` c) `Hexagon` d) `Rand`

e) `2TriaR` f) `2TriaHN` g) `4TriaR` h) `4TriaD`

Figure 4.2: Overview of adopted meshes: in the first row the 2D standard meshes, while in the second row the 2D structured meshes.

Patch test results. In Tables 4.1, 4.2, 4.3 and 4.4, we provide the errors for standard meshes. All quantities behave as expected: indeed, they are close to the machine precision at each mesh refinement step. Moreover, we notice that, refining the mesh, the errors become larger. This fact can be ascribed to the conditioning of the global matrix of the problem.

Linear test results. Figure 4.3 reports the h-convergence of the proposed method for a linear test case. The asymptotic convergence rate is approximately equal to 1 for all errors and meshes, except for $E_{\boldsymbol{\sigma},\Pi}$ on the `Square` mesh, where the errors are exact up to machine precision. The convergence rate is what we expect, although we do not have stress errors ($E_{\boldsymbol{\sigma}}$, $E_{\boldsymbol{\sigma},\mathbf{div}}$ and $E_{\boldsymbol{\sigma},\Pi}$) close to the machine precision for all meshes. Indeed, we recall that the problem has constant stress tensor and null divergence. Moreover, since we employ constant degrees of freedom, we can not expect to have a convergence order greater than one unless we consider problems and meshes with specific properties, i.e., some symmetry.

Remark 16. *The same kind of results have been obtained also when the solution is a rigid body motion, but for the sake of brevity these results have been omitted.*

Quadratic test results. In Figure 4.4, we report the h-convergence for quadratic test on the standard and structured meshes. Immediately, we notice that the asymptotic con-

	Discrete error for the stress field			
Step	`Square`	`Tria`	`Hexagon`	`Rand`
1	6.29736e-15	3.67744e-14	1.11455e-14	1.17551e-14
2	8.87421e-15	8.52208e-13	1.92446e-14	2.23804e-14
3	1.54616e-14	1.86801e-12	4.63053e-14	1.69440e-13
4	2.88012e-14	2.44488e-11	1.31449e-13	3.10865e-13

Table 4.1: Test case 1 (Patch Test). h-convergence results for error $E_{\boldsymbol{\sigma}}$.

	L^2 error on the divergence			
Step	`Square`	`Tria`	`Hexagon`	`Rand`
1	1.15126e-13	1.98533e-13	2.74099e-13	1.32310e-13
2	1.13386e-13	7.95424e-12	1.19696e-12	8.52652e-13
3	1.13492e-13	2.77922e-11	4.96398e-12	8.95224e-12
4	1.13409e-13	5.91654e-10	3.20486e-11	3.51223e-11

Table 4.2: Test case 1 (Patch Test). h-convergence results for error $E_{\boldsymbol{\sigma},\mathbf{div}}$.

	L^2 error on the projection			
Step	`Square`	`Tria`	`Hexagon`	`Rand`
1	4.91119e-15	3.28548e-14	9.81103e-15	1.27816e-14
2	8.83546e-15	7.78224e-13	1.55481e-14	2.12182e-14
3	1.59807e-14	1.74302e-12	4.18572e-14	1.94968e-13
4	3.00927e-14	2.28223e-11	9.87118e-14	3.66368e-13

Table 4.3: Test case 1 (Patch Test). h-convergence results for error $E_{\boldsymbol{\sigma},\Pi}$.

	L^2 error for displacement field			
Step	`Square`	`Tria`	`Hexagon`	`Rand`
1	4.98458e-14	5.00449e-14	5.01009e-14	5.04163e-14
2	4.98429e-14	1.89908e-12	5.09036e-14	5.11523e-14
3	4.98625e-14	7.15558e-12	6.02846e-14	1.87605e-12
4	4.99291e-14	1.61151e-10	1.07341e-13	6.18440e-12

Table 4.4: Test case 1 (Patch Test). h-convergence results for error $E_{\mathbf{u}}$.

vergence rate is approximately equal to 1 for all error norms, but only for `Square`, `Hexagon`, `Rand`, `2TriaHN` and `4TriaR` meshes, while for `Tria`, `2TriaR` and `4TriaD` meshes we lose the convergence rate. Moreover, if we focus our attention on the L^2 error on the divergence, we can observe that, for `Square`, `Hexagon` and `4TriaR`, the convergence rate is 2. As we

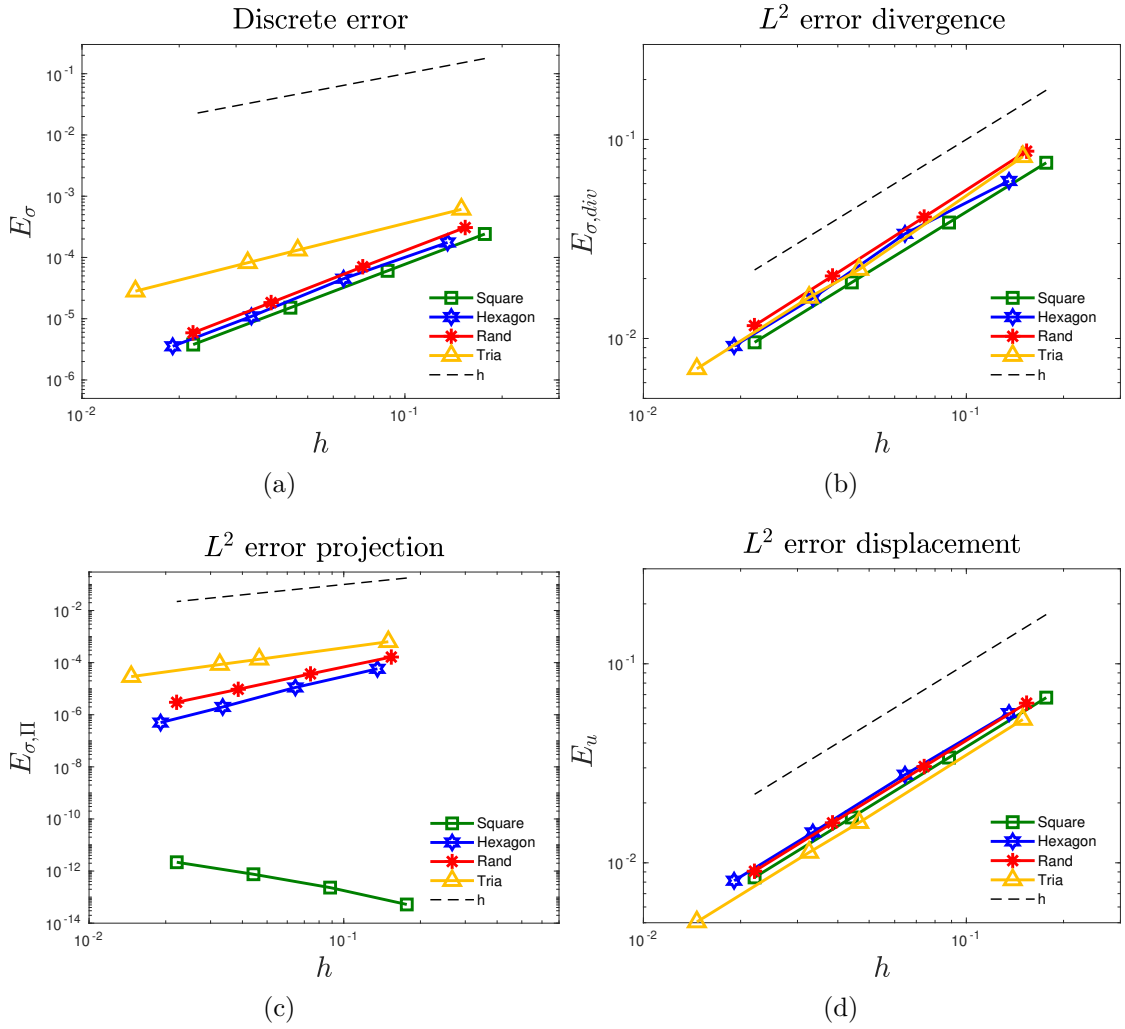

Figure 4.3: Test case 2 (Linear Test). h-convergence results for the standard meshes.

have said before, probably, this fact derives from some properties of the problem and the mesh. Moreover, from the Figure 4.4, we infer the following conjectures:

1. the comparison between `Rand` mesh, which is composed of general polygons including also the triangles, and `Tria` mesh suggests to us that, probably, the loss of convergence is not related to a single triangle, but a mesh with a cluster of triangular elements;

2. the comparison between `2TriaR` mesh and `2TriaHN` mesh suggests to us that, maybe, the trouble is not related to the shape of the elements, but something tied to the number of the edges;

3. the comparison between `4TriaR` and `4TriaD` says that the first one is probably a lucky case due to its structure and symmetry.

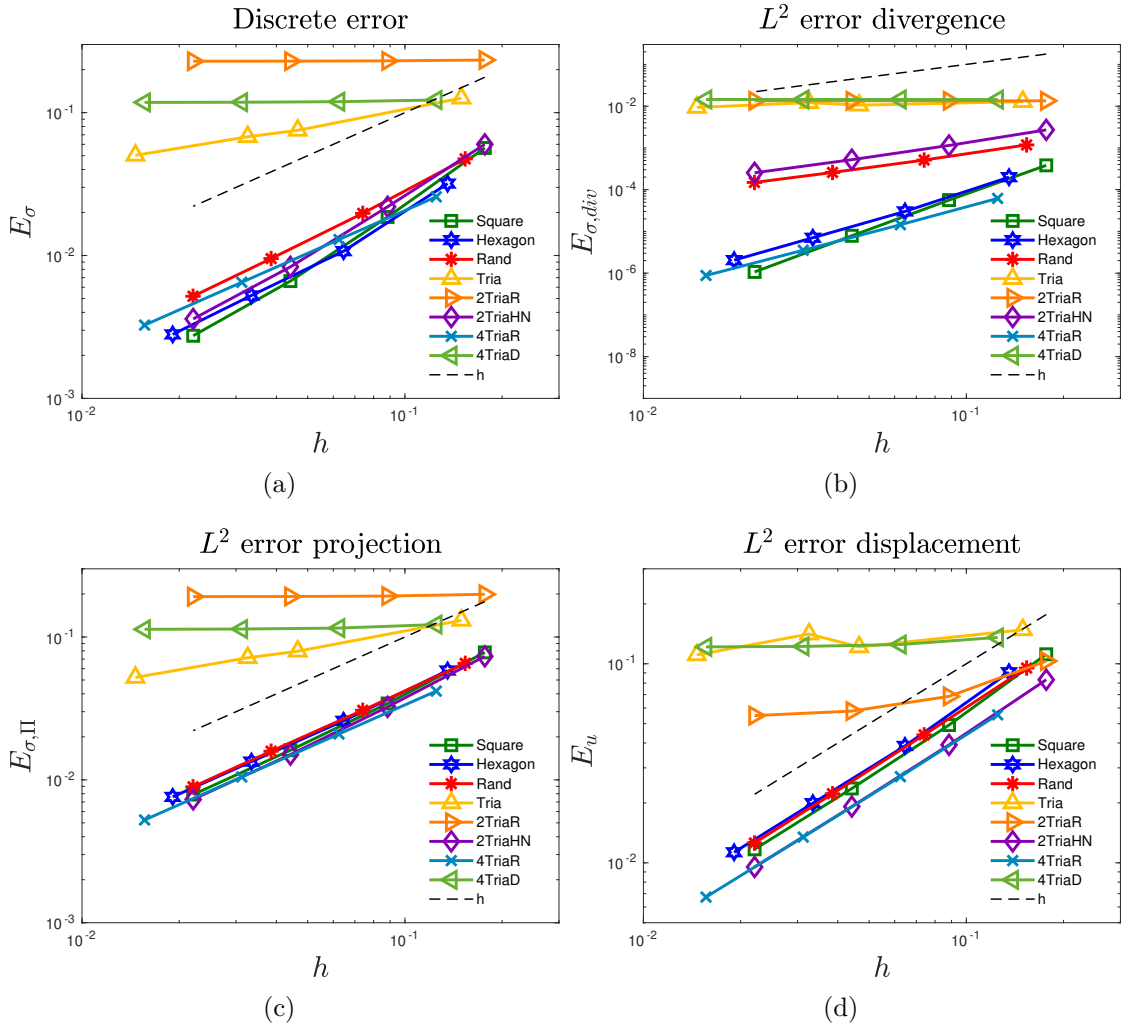

Figure 4.4: Test case 3 (Quadratic Test). h-convergence results for the standard and structured meshes.

Therefore, in general, it seems that our method does not work well on triangular meshes.

Remark 17. *To explore the second conjecture, i.e., the hypothesis that the number of edges plays a role, we also tried adding an extra point to the triangles in the meshes* `4TriaR` *and* `4TriaD`*. The results are similar to those obtained with* `2TriaNH`*.*

4.3.2 Some further issues about our method

In this section, we investigate other aspects of the proposed method. Considering the **Test case 3**, we deepen some interesting features about the divergence error, the best approximation result for the stress field, and the natural interpolation operator, that we do not define it but that we can infer from what we have seen in Chapter 2.

Investigation on the divergence error. The aim of the present test is to investigate the behavior of the stress degrees of freedom in the construction of the discrete divergence (cf. (4.6), (4.7) and (4.8)). First of all, we recall that the (local) discrete divergence can be written as follows

$$\mathbf{div}\,\boldsymbol{\sigma}_h := \boldsymbol{\alpha}_E + \beta_E(\mathbf{x}-\mathbf{x}_E)^{\perp},$$

and that the divergence of a quadratic function is a constant vector. Then, for this test case, we exploit the following error norms:

- the L^2 error norm of the constant part of divergence:

$$E_{\mathbf{div},\boldsymbol{\alpha}} = \left(\sum_{E\in\mathcal{T}_h} ||\,\mathbf{div}\,\boldsymbol{\sigma} - \boldsymbol{\alpha}_E||^2_{0,E}\right)^{1/2}, \tag{4.27}$$

- the L^2 error norm on the rotational part of divergence:

$$E_{\mathbf{div},\beta} = \left(\sum_{E\in\mathcal{T}_h} ||\beta_E(\mathbf{x}-\mathbf{x}_E)^{\perp}||^2_{0,E}\right)^{1/2}. \tag{4.28}$$

The idea is to examine the constant and the rotational part separately in order to understand the reason why, in the $E_{\boldsymbol{\sigma},\mathbf{div}}$ plot of the Figure 4.4, the convergence lines for `Tria`, `2TriaR` and `4TriaD` meshes are stagnant.

Results. In Tables 4.5, 4.6 and in Tables 4.7, 4.8 we report the $E_{\mathbf{div},\boldsymbol{\alpha}}$ and $E_{\mathbf{div},\beta}$ errors, respectively. We notice that the L^2 error norm on the constant part is close to the machine precision at each mesh refinement step. Instead, for the rotational part, we have two conflicting results. On the one hand, for `Tria`, `2TriaR` and `4TriaD` meshes the errors are constants. On the other hand, for the remaining meshes, the errors seem converge with rate 1. Hence, these results clarify the behavior of the L^2 error on the divergence in the Figure 4.4. Moreover, always considering the plots in Figure 4.4, we have that despite the stress degrees of freedom fix the constant part of the divergence, they do not converge to the continuous solution for `Tria`, `2TriaR` and `4TriaD` meshes. Hence, it seems that the triangular meshes are too "rigid" (in some sense) to ensure both the continuity of the tractions and the requirement that the divergence is in $RM(E)$.

Investigation on the best approximation of the stress field. In this second test, we want to numerically study the best approximation result for the stress field. In this investigation, we consider the following two discrete global spaces for the stress field:

$$\Sigma_h^0 = \left\{\boldsymbol{\tau}_h \in H(\mathrm{div};\Omega) \;:\; \boldsymbol{\tau}_{h|E} \in \Sigma_h^0(E) \quad \forall E\in\mathcal{T}_h\right\},$$

which is defined in (4.19) and

$$\tilde{\Sigma}_h^0 = \left\{\boldsymbol{\tau}_h \in \left[L^2(\Omega)\right]^{2\times 2} \;:\; \boldsymbol{\tau}_{h|E} \in \Sigma_h^0(E) \quad \forall E\in\mathcal{T}_h\right\}. \tag{4.29}$$

Step	Square	Tria	Hexagon	Rand
1	7.72793e-16	2.23175e-15	1.56482e-15	1.03244e-15
2	1.36127e-15	1.85703e-13	3.49287e-15	2.33071e-15
3	2.63964e-15	9.15831e-14	6.51563e-15	4.46223e-15
4	5.06186e-15	1.63717e-11	2.41610e-13	7.85365e-15

Table 4.5: Divergence error results. h-convergence results for error $E_{\mathbf{div},\boldsymbol{\alpha}}$ on standard meshes

Step	2TriaR	2TriaHN	4TriaR	4TriaD
1	2.02240e-15	2.23825e-15	2.96848e-15	2.28429e-15
2	3.88623e-15	4.38796e-15	5.98427e-15	4.76713e-15
3	7.44575e-15	8.26223e-15	1.13369e-14	9.57196e-15
4	1.50111e-14	1.71392e-14	2.30845e-14	1.93620e-14

Table 4.6: Divergence error results. h-convergence results for error $E_{\mathbf{div},\boldsymbol{\alpha}}$ on structured meshes

Step	Square	Tria	Hexagon	Rand
1	2.29254e-03	7.70329e-02	7.08047e-03	1.19239e-03
2	3.37544e-04	6.32102e-02	3.07257e-03	1.80474e-04
3	4.70813e-05	7.28872e-02	1.55001e-03	4.23038e-05
4	6.41623e-06	5.59572e-02	8.92862e-04	1.23026e-05

Table 4.7: Divergence error results. h-convergence results for error $E_{\mathbf{div},\beta}$ on standard meshes

Step	2TriaR	2TriaHN	4TriaR	4TriaD
1	8.04814e-02	1.62197e-02	8.61902e-02	3.70359e-04
2	8.04990e-02	6.86884e-03	8.66097e-02	8.68754e-05
3	8.05059e-02	3.13441e-03	8.67157e-02	2.12608e-05
4	8.05078e-02	1.52033e-03	8.67421e-02	5.28085e-06

Table 4.8: Divergence error results. h-convergence results for error $E_{\mathbf{div},\beta}$ on structured meshes.

The difference between these two spaces is that, in the first one we require continuous tractions on the inter-elements, while for the second this does not happen. Therefore, the problem that we want to study is the following: find $\boldsymbol{\sigma}_h \in \hat{\Sigma}_h^0$ such that

$$\inf_{\boldsymbol{\sigma}_h \in \hat{\Sigma}_h^0} \frac{1}{2} ||\boldsymbol{\sigma}_h - \boldsymbol{\sigma}||_{\Sigma}^2 = \inf_{\boldsymbol{\sigma}_h \in \hat{\Sigma}_h^0} \frac{1}{2} \left(||\boldsymbol{\sigma}_h - \boldsymbol{\sigma}||_{0,\Omega}^2 + ||\operatorname{\mathbf{div}} \boldsymbol{\sigma}_h - \operatorname{\mathbf{div}} \boldsymbol{\sigma}||_{0,\Omega}^2 \right), \tag{4.30}$$

where $\boldsymbol{\sigma}$ is the solution of the Problem (4.1) and $\hat{\Sigma}_h^0$ is our notation to denote one of the two spaces previously defined. The above problem is equivalent to find $\boldsymbol{\sigma}_h \in \hat{\Sigma}_h^0$ such that

$$\int_\Omega \mathbb{D}(\boldsymbol{\sigma}_h - \boldsymbol{\sigma}) : \boldsymbol{\tau}_h \, \mathrm{d}\Omega + \int_\Omega \operatorname{\mathbf{div}}(\boldsymbol{\sigma}_h - \boldsymbol{\sigma}) \cdot \operatorname{\mathbf{div}} \boldsymbol{\tau}_h \, \mathrm{d}\Omega = 0 \qquad \forall \boldsymbol{\tau}_h \in \hat{\Sigma}_h^0. \tag{4.31}$$

Using some algebraic steps, the equation (4.31) becomes

$$\int_\Omega \mathbb{D}\boldsymbol{\sigma}_h : \boldsymbol{\tau}_h \, \mathrm{d}\Omega + \int_\Omega \operatorname{\mathbf{div}} \boldsymbol{\sigma}_h \cdot \operatorname{\mathbf{div}} \boldsymbol{\tau}_h \, \mathrm{d}\Omega = \int_\Omega \mathbb{D}\boldsymbol{\sigma} : \boldsymbol{\tau}_h \, \mathrm{d}\Omega + \int_\Omega \operatorname{\mathbf{div}} \boldsymbol{\sigma} \cdot \operatorname{\mathbf{div}} \boldsymbol{\tau}_h \, \mathrm{d}\Omega, \quad \forall \boldsymbol{\tau}_h \in \hat{\Sigma}_h^0. \tag{4.32}$$

Now, thanks to VEM technology (4.15), the problem of the best approximation can be written as follows:

$$\begin{cases} \text{find } \boldsymbol{\sigma}_h \in \hat{\Sigma}_h^0 \text{ such that} \\ a_h(\boldsymbol{\sigma}_h, \boldsymbol{\tau}_h) + (\operatorname{\mathbf{div}} \boldsymbol{\sigma}_h, \operatorname{\mathbf{div}} \boldsymbol{\tau}_h) = a_h(\boldsymbol{\sigma}, \boldsymbol{\tau}_h) + (\operatorname{\mathbf{div}} \boldsymbol{\sigma}, \operatorname{\mathbf{div}} \boldsymbol{\tau}_h) \quad \forall \boldsymbol{\tau}_h \in \hat{\Sigma}_h^0. \end{cases} \tag{4.33}$$

The idea of this test is to numerically simulate the best approximation result for both stress spaces (4.19) and (4.29).

Results. In Figure 4.5 we report the error norms $E_{\boldsymbol{\sigma}}$ and $E_{\boldsymbol{\sigma},\mathbf{div}}$ for the investigation on the best approximation of the stress field. First of all, we notice that when we consider conforming discrete stresses for `Tria`, `2TriaR` and `4TriaD` meshes, we lose the convergence rate, while this does not occur when we take $\boldsymbol{\sigma}_h \in \tilde{\Sigma}_h^0$. In addition, for the remaining meshes, the errors seem to have the same convergent behavior. From these observations, it seems that the $H(\mathbf{div})$-conformity of the stress field, together with the structure of the mesh, could be one of the reasons for our troubles.

Investigation on the interpolation operator. In this final test, we would like to investigate some properties of natural interpolation operator. Following the steps of Section 2.2.1, we introduce the local natural interpolation operator $\mathcal{I}_E^0 : W^r(E) \to \Sigma_h^0(E)$, which is defined by:

$$\int_{\partial E} (\mathcal{I}_E^0 \boldsymbol{\tau}) \mathbf{n} \cdot \boldsymbol{\varphi}_* \, \mathrm{d}s = \int_{\partial E} (\boldsymbol{\tau}\, \mathbf{n}) \cdot \boldsymbol{\varphi}_* \, \mathrm{d}s \qquad \forall \boldsymbol{\varphi}_* \in R_*^0(\partial E), \tag{4.34}$$

where:

$$R_*^0(\partial E) = \left\{ \boldsymbol{\varphi}_* \in \left[L^2(\partial E) \right]^2 \, : \, \boldsymbol{\varphi}_{*|_e} = \boldsymbol{\gamma}_e, \quad \boldsymbol{\gamma}_e \in \mathbb{R}^2, \ \forall e \in \partial E \right\}. \tag{4.35}$$

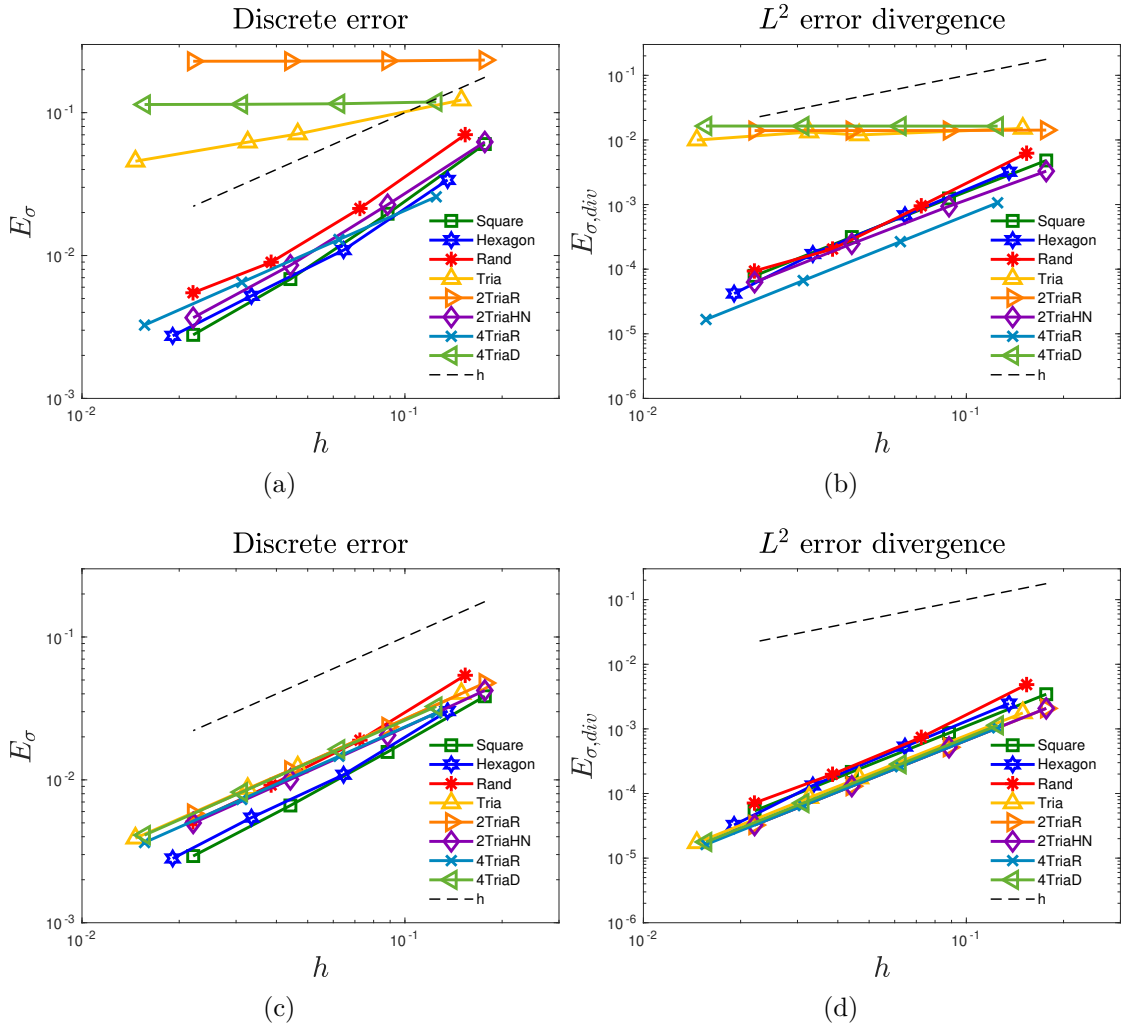

Figure 4.5: Best approximation results. h-convergence results for $E_{\boldsymbol{\sigma}}$ and $E_{\boldsymbol{\sigma},\mathbf{div}}$. In the first row, we consider stresses in Σ_h^0, while in the second one, we take stresses in $\tilde{\Sigma}_h^0$.

If $\boldsymbol{\tau}$ is sufficiently regular, the above condition is equivalent to require:

$$\int_e (\mathcal{I}_E^0 \boldsymbol{\tau})\mathbf{n} \cdot \boldsymbol{\alpha} \ \mathrm{d}s = \int_e \boldsymbol{\tau}\mathbf{n} \cdot \boldsymbol{\alpha} \ \mathrm{d}s \qquad \forall \boldsymbol{\alpha} \in \mathbb{R}^2, \ \forall e \in \partial E. \tag{4.36}$$

The local interpolated function $\mathcal{I}_E^0 \boldsymbol{\tau} \in \Sigma_h^0(E)$ is well-defined by condition (4.36). Therefore, the global interpolation operator $\mathcal{I}_h^0 : W^r(\Omega) \to \Sigma_h^0$ is just defined by glueing the local contributions as follows:

$$(\mathcal{I}_h^0 \tau)_{|E} := \mathcal{I}_E^0 \boldsymbol{\tau}_{|E} \quad \forall E \in \mathcal{T}_h, \forall \boldsymbol{\tau} \in W^r(\Omega).$$

Now set $\boldsymbol{\sigma}_I = \mathcal{I}_h^0 \boldsymbol{\sigma}$, we introduce the following L^2 error on divergence:

$$E_{\mathbf{div}\,\sigma_I} := \left(\sum_{E \in \mathcal{T}_h} \int_E |\,\mathbf{div}(\boldsymbol{\sigma} - \boldsymbol{\sigma}_I)|^2 \ \mathrm{d}E \right)^{1/2} = ||\,\mathbf{div}\,\boldsymbol{\sigma} - \mathbf{div}\,\boldsymbol{\sigma}_I||_0. \tag{4.37}$$

For simplicity, we consider **Test case 3** with Lamé coefficients $\lambda = 0$ and $\mu = 0.5$. Hence, the elastic fourth-order tensor $\mathbb{C}$ is the identity.

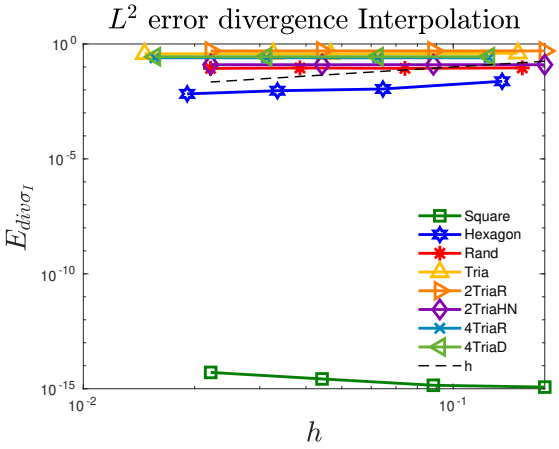

Figure 4.6: Interpolation operator results. h-convergence results for error $E_{\mathbf{div}\,\boldsymbol{\sigma}_I}$ all meshes.

Results. In Figure 4.6, we report the $E_{\mathbf{div}\,\sigma_I}$ plots for all meshes (standard and structured). Immediately, we can notice that for all meshes, except `Square` mesh, the errors do not converge. These results seem to suggest to us that the natural interpolation operator is not the best choice one can make. Hence, we probably need to find a more sophisticated interpolation operator in order to justify the behavior of the method that seems to be convergent if we exclude the triangular meshes.

4.4 Final considerations

We have presented a numerical investigation on a Virtual Element Method with reduced stress and displacement spaces for an augmented Lagrangian formulation. The results have shown that the proposed method does not converge when we deal with a triangular mesh or, more generally, a mesh with a cluster of triangles. We presume that a possible reason for this trouble is not related to a singular element but is connected to some global properties: i.e., the relationship between the $H(\mathbf{div})$-conformity and the symmetry of the stress. Therefore, considering the results of the proposed tests and these considerations, our future steps could be as follows: design a new and more sophisticated interpolation operator; study and implement, if it is possible, the inf-sup test [21], in order to obtain (numerically) an indication on the discrete inf-sup condition; relax the symmetry condition or the $H(\mathbf{div})$-conformity, considering for instance a non-conforming scheme for our augmented Lagrangian formulation.

Conclusions

We have proposed some Virtual Element Methods for the mixed stress-displacement formulation of linear elasticity problems. In particular, we have considered schemes with a-priori symmetric stresses. First of all, we have presented a conforming low-order VEM scheme for 3D problems, where we have exploited the flexibility of VEM to construct a stable and accurate scheme. The convergence and stability analysis has been confirmed by some numerical results. Afterward, exploiting the definition of the degrees of freedom of the stress field, we have applied the hybridization procedure to low-order VEM schemes for both bi-dimensional and three-dimensional problems. The numerical results have shown advantages from a computational and theoretical point of view. Indeed, we have seen a reduction in the solving time and a better reconstruction of the continuous solution through a simple post-processing procedure. Finally, we have presented a preliminary study of a Virtual Element Method for an augmented Lagrangian formulation. More precisely, we have numerically investigated the behavior of a method with reduced stress and displacement spaces. The results have shown that the proposed method does not converge when we deal with triangular meshes, but they also have suggested to us the future way to go.

Acknowledgments

First and foremost, I would like to express my sincere gratitude to my supervisor, Prof. Carlo Lovadina, for his guidance over the past three and a half years. Thanks for the continuous support and encouragement, for the invaluable advice, and the fruitful discussions.

Additionally, I wish to thank Prof. Lourenço Beirão da Veiga for accepting to be my tutor, for his interest in my work, and his extraordinary helpfulness whenever I needed it.

A huge thank goes to Dr. Franco Dassi, who patiently guided me in the world of Vem++. Thank you for always finding the time to discuss my doubts, answer my questions, and help me.

I would also like to thank Prof. Ilaria Perugia and Dr. Lorenzo Mascotto that have supervised my work during my stay at the University of Vienna (February 2020-June 2020). The opportunity to work in their research group has been fundamental for my growth as a mathematician.

I am obliged to Prof. David Mora and Prof. Marco Verani for their reports on this thesis and for their interest in my work.

Then, I wish to thank all the Ph.D. students and researchers I had the opportunity to meet during my doctoral studies. Thanks for all time we spent during the workshops, lessons, lunch breaks, trips, and spare time.

Finally, I would like to express my gratitude to my family and my friends for their constant encouragement and support during these years.
Thank you so much!

Michele

Bibliography

[1] B. Ahmad, A. Alsaedi, F. Brezzi, L. D. Marini, and A. Russo. Equivalent projectors for virtual element methods. *Comput. Math. Appl.*, 66(3):376–391, 2013.

[2] O. Andersen, H. Nilsen, and X. Raynaud. Virtual element method for geomechanical simulations of reservoir models. *Comput. Geosci.*, 21(5):877–893, Dec 2017.

[3] P. F. Antonietti, L. Beirão da Veiga, D. Mora, and M. Verani. A stream virtual element formulation of the Stokes problem on polygonal meshes. *SIAM J. Numer. Anal.*, 52(1):386–404, 2014.

[4] P. F. Antonietti, L. Beirão da Veiga, S. Scacchi, and M. Verani. A C^1 virtual element method for the Cahn–Hilliard equation with polygonal meshes. *SIAM J. Numer. Anal.*, 54(1):34–56, 2016.

[5] P. F. Antonietti, A. Cangiani, J. Collis, Z. Dong, E. H. Georgoulis, S. Giani, and P. Houston. Review of discontinuous galerkin finite element methods for partial differential equations on complicated domains. In *Building Bridges: Connections and Challenges in Modern Approaches to Numerical Partial Differential Equations*, pages 279–308. Springer, Berlin, 2016.

[6] D. N. Arnold, G. Awanou, and R. Winther. Finite elements for symmetric tensors in three dimensions. *Math. Comp.*, 77:1229–1251, 2008.

[7] D. N. Arnold and F. Brezzi. Mixed and nonconforming finite element methods: implementation, postprocessing and error estimates. *ESAIM Math. Model. Numer. Anal.*, 19:7–32, 1985.

[8] D. N. Arnold, F. Brezzi, and J. Douglas. PEERS: A new mixed finite element for plane elasticity. *Japan J. Appl. Math.*, 2:347–367, 1984.

[9] D. N. Arnold and R. Falk. A new mixed formulation for elasticity. *Numer. Math.*, 53:13–30, 1988.

[10] D. N. Arnold and R. Winther. Mixed finite elements for elasticity. *Numer. Math.*, 92:401–419, 2002.

[11] E. Artioli, L. Beirão da Veiga, and F. Dassi. Curvilinear virtual elements for 2D solid mechanics applications. *Comp. Methods Appl. Mech. Engrg.*, 359:112667, 2020.

[12] E. Artioli, L. Beirão da Veiga, C. Lovadina, and E. Sacco. Arbitrary order 2D virtual elements for polygonal meshes: Part I, elastic problem. *Comput. Mech.*, 60(3):355–377, Sep 2017.

[13] E. Artioli, L. Beirão da Veiga, C. Lovadina, and E. Sacco. Arbitrary order 2D virtual elements for polygonal meshes: Part II, inelastic problems. *Comput. Mech.*, 60(4):643–657, Oct 2017.

[14] E. Artioli, L. Beirão da Veiga, and M. Verani. An adaptive curved virtual element method for the statistical homogenization of random fibre-reinforced composites. *Finite Elem. Anal. Des.*, 177:103418, 2020.

[15] E. Artioli, S. de Miranda, C. Lovadina, and L. Patruno. A stress/displacement virtual element method for plane elasticity problems. *Comp. Methods Appl. Mech. Engrg.*, 325:155–174, 2017.

[16] E. Artioli, S. de Miranda, C. Lovadina, and L. Patruno. A family of virtual element methods for plane elasticity problems based on the hellinger-reissner principle. *Comp. Methods Appl. Mech. Engrg.*, 340:978–999, 2018.

[17] E. Artioli, S. de Miranda, C. Lovadina, and L. Patruno. An equilibrium-based stress recovery procedure for the VEM. *Int. J. Numer. Methods Eng.*, 117:885–900, 2019.

[18] B. Ayuso, K. Lipnikov, and G. Manzini. The nonconforming virtual element method. *ESAIM: Math. Model. Numer. Anal.*, 50(3):879–904, 2016.

[19] S. Balay, S. Abhyankar, M. F. Adams, J. Brown, P. Brune, K. Buschelmanm, L. Dalcin, A. Dener, V. Eijkhout, W. D. Gropp, D. Karpeyev, D. Kaushik, M. G. Knepley, D. A. May, L. C. McInnes, R. T. Mills, T. Munson, K. Rupp, P. Sanan, B. F. Smith, S. Zampini, H. Zhang, and H. Zhang. PETSc Web page. https://www.mcs.anl.gov/petsc, 2019.

[20] S. Balay, S. Abhyankar, M. F. Adams, J. Brown, P. Brune, K. Buschelmanm, L. Dalcin, A. Dener, V. Eijkhout, W. D. Gropp, D. Karpeyev, D. Kaushik, M. G. Knepley, D. A. May, L. C. McInnes, R. T. Mills, T. Munson, K. Rupp, P. Sanan, B. F. Smith, S. Zampini, H. Zhang, and H. Zhang. PETSc users manual. Technical Report ANL-95/11 - Revision 3.14, Argonne National Laboratory, 2020.

[21] K. J. Bathe, A. Iosilevich, and D. Chapelle. An inf-sup test for shell finite elements. *Comput. Struct.*, 75(5):439–456, 2000.

[22] L. Beirão da Veiga, F. Brezzi, A. Cangiani, G. Manzini, L. D. Marini, and A. Russo. Basic principles of Virtual Element Methods. *Math. Models Methods Appl. Sci.*, 23:119–214, 2013.

[23] L. Beirão da Veiga, F. Dassi, and A. Russo. A C^1 virtual element method on polyhedral meshes. *Comput. Math. Appl.*, 79(7):1936–1955, 2020.

[24] L. Beirão da Veiga, F. Dassi, and G. Vacca. The stokes complex for virtual elements in three dimensions. *Math. Models Methods Appl. Sci.*, 30(3):477–512, 2020.

[25] L. Beirão da Veiga, D. Mora, and G. Vacca. The Stokes complex for virtual elements with application to Navier-Stokes flows. *J. Sci. Comput.*, 81(2):990–1018, 2019.

[26] L. Beirão da Veiga, F. Brezzi, F. Dassi, L. D. Marini, and A. Russo. A family of three-dimensional virtual elements with applications to magnetostatics. *SIAM J. Numer. Anal.*, 56(5):2940–2962, 2018.

[27] L. Beirão da Veiga, F. Brezzi, F. Dassi, L. D. Marini, and A. Russo. Lowest order virtual element approximation of magnetostatic problems. *Comput. Methods Appl. Mech. Engrg.*, 332:343–362, 2018.

[28] L. Beirão da Veiga, F. Brezzi, L. D. Marini, and A. Russo. The hitchhiker's guide to the virtual element method. *Math. Models Methods Appl. Sci.*, 24(8):1541–1573, 2014.

[29] L. Beirão da Veiga, K. Lipnikov, and G. Manzini. *The mimetic finite difference method for elliptic problems*, volume 11 of *Modeling, Simulation and Applications*. Springer, 2014.

[30] L. Beirão da Veiga, C. Lovadina, and D. Mora. A virtual element method for elastic and inelastic problems on polytope meshes. *Comput. Methods Appl. Mech. Engrg.*, 295:327–346, 2015.

[31] L. Beirão da Veiga, C. Lovadina, and A. Russo. Stability analysis for the virtual element method. *Math. Models Methods Appl. Sci.*, 27(13):2557–2594, 2017.

[32] L. Beirão da Veiga, C. Lovadina, and G. Vacca. Divergence free virtual elements for the Stokes problem on polygonal meshes. *ESAIM Math. Model. Numer. Anal.*, 51(2):509–535, 2017.

[33] L. Beirão da Veiga and G. Manzini. A higher-order formulation of the mimetic finite difference method. *SIAM J. Sci. Comput.*, 31(1):732–760, 2008.

[34] L. Beirão da Veiga, A. Russo, and G. Vacca. The virtual element method with curved edges. *ESAIM Math. Model. Numer. Anal.*, 53(2):375–404, 2019.

[35] M. F. Benedetto, S. Berrone, A. Borio, S. Pieraccini, and S. Scialò. A hybrid mortar virtual element method for discrete fracture network simulations. *J. Comput. Phys.*, 306:148–166, 2016.

[36] M. F. Benedetto, S. Berrone, S. Pieraccini, and S. Scialò. The virtual element method for discrete fracture network simulations. *Comput. Methods Appl. Mech. Engrg.*, 280:135–156, 2014.

[37] M. F. Benedetto, A. Borio, and S. Scialò. Mixed virtual elements for discrete fracture network simulations. *Finite Elem. Anal. Des.*, 134:55–67, 2017.

[38] S. Biabanaki, A. Khoei, and P. Wriggers. Polygonal finite element methods for contact-impact problems on non-conformal meshes. *Comp. Methods Appl. Mech. Engrg.*, 269:198–221, 2014.

[39] D. Boffi, F. Brezzi, and M. Fortin. *Mixed finite element methods and applications*, volume 44 of *Springer Series in Computational Mathematics*. Springer, Heidelberg, 2013.

[40] D. Boffi and C. Lovadina. Analysis of new augmented lagrangian formulations for mixed finite element schemes. *Numer. Math.*, 75(4):405–419, 1997.

[41] D. Braess. *Finite elements. Theory, fast solvers, and applications in elasticity theory.* Cambridge University Press, third edition, 2007.

[42] S. C. Brenner and L. R. Scott. *The mathematical theory of finite element methods*, volume 15 of *Texts in Applied Mathematics*. Springer, New York, third edition, 2008.

[43] S. C. Brenner and L. Sung. Virtual element methods on meshes with small edges or faces. *Math. Models Methods Appl. Sci.*, 28(7):1291–1336, 2018.

[44] F. Brezzi, A. Buffa, and K. Lipnikov. Mimetic finite differences for elliptic problems. *ESAIM Math. Model. Numer. Anal.*, 43(2):277–295, 2009.

[45] F. Brezzi, R. S. Falk, and L. D. Marini. Basic principles of mixed virtual element methods. *ESAIM Math. Model. Numer. Anal.*, 48(4):1227–1240, 2014.

[46] F. Brezzi and M. Fortin. *Mixed and Hybrid Finite Element Methods*. Springer-Verlag, New York, 1991.

[47] F. Brezzi, M. Fortin, and L. D. Marini. Mixed finite element methods with continuous stresses. *Math. Models Methods Appl. Sci.*, 3(2):275–287, 1993.

[48] A. Cangiani, V. Gyrya, and G. Manzini. The nonconforming virtual element method for the Stokes equations. *SIAM J. Sci. Comput.*, 54(6):3411–3435, 2016.

[49] H. Chi, C. Talischi, O. Lopez-Pamies, and G. H. Paulino. Polygonal finite elements for finite elasticity. *Int. J. Numer. Methods Eng.*, 101(4):305–328, 2015.

[50] P. G. Ciarlet. *The Finite Element Method for Elliptic Problems*. North-Holland, Amsterdam, 1978.

[51] B. Cockburn, J. Gopalakrishnan, and R. Lazarov. Unified hybridization of discontinuous galerkin, mixed, and continuous galerkin methods for second order elliptic problems. *SIAM J. Numer. Anal.*, 47(2):1319–1365, 2009.

[52] M. Crouzeix and P.-A. Raviart. Conforming and nonconforming finite element methods for solving the stationary stokes equations I. *ESAIM Math. Model. Numer. Anal.*, 7(R3):33–75, 1973.

[53] F. Dassi, A. Fumagalli, D. Losapio, D. Scialò, A. Scotti, and G. Vacca. The mixed virtual element method for grids with curved interfaces. Preprint arXiv:2011.09332., 2020.

[54] F. Dassi, C. Lovadina, and M. Visinoni. A three-dimensional hellinger-reissner virtual element method for linear elasticity problems. *Comput. Methods Appl. Mech. Engrg.*, 364:112910, 2020.

[55] F. Dassi, C. Lovadina, and M. Visinoni. Hybridization of the virtual element method for linear elasticity problems. Preprint arXiv:2103.01164., 2021.

[56] F. Dassi and L. Mascotto. Exploring high-order three dimensional virtual elements: bases and stabilizations. *Comput. Math. Appl.*, 75(9):3379–3401, 2018.

[57] B. F. De Veubeke and O. C. Zienkiewicz. Displacement and equilibrium models in the finite element method. *Int. J. Numer. Methods Eng.*, 52(3):287–342, 2001.

[58] D. A. Di Pietro and A. Ern. A hybrid high-order locking-free method for linear elasticity on general meshes. *Comput. Methods Appl. Mech. Engrg.*, 283:1–21, 2015.

[59] D. A. Di Pietro and A. Ern. Hybrid high-order methods for variable-diffusion problems on general meshes. *C. R. Acad. Sci. Paris, Ser. I*, 353:31–34, 2015.

[60] Q. Du, V. Faber, and M. Gunzburger. Centroidal Voronoi tessellations: applications and algorithms. *SIAM Rev.*, 41(4):637–676, 1999.

[61] M. Fortin and R. Glowinski. *Augmented Lagrangian Methods: Applications to the Numerical Solution of Boundary-Value Problems.* North Holland, 1983.

[62] T.-P. Fries and T. Belytschko. The extended/generalized finite element method: An overview of the method and its applications. *Int. J. Numer. Methods Eng.*, 84(3):253–304, 2010.

[63] A. L. Gain and G. H. Paulino. Phase-field based topology optimization with polygonal elements: a finite volume approach for the evolution equation. *Struct. Multidiscip. Optim.*, 46(3):327–342, 2012.

[64] F. Gardini, G. Manzini, and G. Vacca. The nonconforming virtual element method for eigenvalue problems. *ESAIM Math. Model. Numer. Anal.*, 53(3):749–774, 2019.

[65] J.-L. Lions and E. Magenes. *Problèmes aux limites non homogènes et applications. Vol. 1.* Travaux et Recherches Mathématiques, No. 17. Dunod, Paris, 1968.

[66] L. Mascotto, I. Perugia, and A. Pichler. Non-conforming harmonic virtual element method: h- and p-versions. *J. Sci. Comput.*, 77(3):1874–1908, 2018.

[67] L. Mascotto, I. Perugia, and A. Pichler. A nonconforming Trefftz virtual element method for the Helmholtz problem. *Math. Models Methods Appl. Sci.*, 29:1619–1656, 2019.

[68] L. Mascotto, I. Perugia, and A. Pichler. A nonconforming Trefftz virtual element method for the Helmholtz problem: numerical aspects. *Comput. Methods Appl. Mech. Engrg.*, 347:445–476, 2019.

[69] D. Mora and I. Velásquez. A virtual element method for the transmission eigenvalue problem. *Math. Models Methods Appl. Sci.*, 28(14):2803–2831, 2018.

[70] S. E. Mousavi and N. Sukumar. Numerical integration of polynomials and discontinuous functions on irregular convex polygons and polyhedrons. *Comput. Mech.*, 47(5):535–554, 2011.

[71] S. E. Mousavi, H. Xiao, and N. Sukumar. Generalized gaussian quadrature rules on arbitrary polygons. *Int. J. Numer. Methods Eng.*, 82(1):99–113, 2010.

[72] A. I. Nazarov and S. I. Repin. Exact constants in Poincaré type inequalities for functions with zero mean boundary traces. *Math. Methods Appl. Sci.*, 38:3195–3207, 2014.

[73] A. Pechstein and J. Schöberl. Tangential-displacement and normal-normal-stress continuous mixed finite elements for elasticity. *Math. Models Methods Appl. Sci.*, 21:1761–1782, 2011.

[74] A. Pechstein and J. Schöberl. An analysis of the TDNNS method using natural norms. *Numer. Math.*, 139:93–120, 2018.

[75] I. Perugia, P. Pietra, and A. Russo. A plane wave virtual element method for the Helmholtz problem. *ESAIM Math. Model. Numer. Anal.*, 50(3):783–808, 2016.

[76] W. Prager and J. Synge. Approximations in elasticity based on the concept of function space. *Quart. Appl. Math.*, 5:241–269, 1947.

[77] C. H. Rycroft. Voro++: A three-dimensional voronoi cell library in c++. *Chaos: An Interdisciplinary Journal of Nonlinear Science*, 19(4):041111, 2009.

[78] J. R. Shewchuk. Triangle: Engineering a 2D Quality Mesh Generator and Delaunay Triangulator. In M. C. Lin and D. Manocha, editors, *Applied Computational Geometry: Towards Geometric Engineering*, volume 1148 of *Lecture Notes in Computer Science*, pages 203–222. Springer-Verlag, May 1996. First ACM Workshop on Applied Computational Geometry.

[79] H. Si. Tetgen, a delaunay-based quality tetrahedral mesh generator. *ACM Trans. Math. Softw.*, 41(2):1–36, Feb. 2015.

[80] A. Sommariva and M. Vianello. Product Gauss cubature over polygons based on green's integration formula. *BIT Numerical Mathematics*, 47(2):441–453, 2007.

[81] E. Stein and R. Rolfes. Mechanical conditions for stability and optimal convergence of mixed finite elements for linear plane elasticity. *Comput. Methods Appl. Mech. Engrg.*, 84(1):77–95, 1990.

[82] R. Stenberg. On the construction of optimal mixed finite element methods for the linear elasticity problem. *Numer. Math.*, 48:447–462, 1986.

[83] C. Talischi, G. H. Paulino, A. Pereira, and I. F. M. . Menezes. Polymesher: a general-purpose mesh generator for polygonal elements written in matlab. *Struct. Multidisc Optimiz.*, 45(3):309–328, 2012.

[84] J. Wang and X. Ye. A weak galerkin finite element method for second-order elliptic problems. *J. Comput. Appl. Math.*, 241:103–115, 2013.

[85] P. Wriggers, B. D. Reddy, W. Rust, and B. Hudobivnik. Efficient virtual element formulations for compressible and incompressible finite deformations. *Comput. Mech.*, page 253–268, 04 2017.

[86] P. Wriggers, W. Rust, and B. D. Reddy. A virtual element method for contact. *Comput. Mech-*, 58:1039–1050, 2016.

[87] B. Zhang and M. Feng. Virtual element method for two-dimensional linear elasticity problem in mixed weakly symmetric formulation. *Appl. Math. Comput.*, 328:1–25, 2018.